Doctoral Dissertations 2014-current              Dissertations and Theses

2-2014

# Discrete Parity-Time Symmetric Nonlinear Schrodinger Lattices

Kai Li

*University of Massachusetts - Amherst*, lk0123@hotmail.com

Follow this and additional works at: http://scholarworks.umass.edu/dissertations_2

# DISCRETE PARITY-TIME SYMMETRIC NONLINEAR SCHRÖDINGER LATTICES

A Dissertation Presented

by

KAI LI

Submitted to the Graduate School of the
University of Massachusetts Amherst in partial fulfillment
of the requirements for the degree of

DOCTOR OF PHILOSOPHY

February 2014

Department of Mathematics and Statistics

# DISCRETE PARITY-TIME SYMMETRIC NONLINEAR SCHRÖDINGER LATTICES

A Dissertation Presented

by

KAI LI

Approved as to style and content by:

_____

Panayotis Kevrekidis, Chair

_____

Nathaniel Whitaker, Member

_____

Hans Johnston, Member

_____

Triantafillos Mountziaris, Member

_____

Michael Lavine, Department Head
Department of Mathematics and Statistics

To my family.

# ACKNOWLEDGMENTS

# ABSTRACT

# DISCRETE PARITY-TIME SYMMETRIC NONLINEAR SCHRÖDINGER LATTICES

## FEBRUARY 2014

KAI LI

B.S., UNIVERSITY OF SCIENCE AND TECHNOLOGY OF CHINA

M.S., UNIVERSITY OF MASSACHUSETTS AMHERST

Ph.D., UNIVERSITY OF MASSACHUSETTS AMHERST

Directed by: Professor Panayotis Kevrekidis

In this thesis we summarize the classical cases of one-dimensional oligomers and two-dimensional plaquettes, respecting the parity-time ($\mathcal{PT}$) symmetry. We examine different types of solutions of such configurations with linear and nonlinear gain or loss profiles. For each configuration, we develop a dynamical model and examine its $\mathcal{PT}$ symmetry. The corresponding nonlinear modes are analyzed starting from the Hamiltonian limit, with zero value of the gain-loss coefficient, $\gamma$. Once the relevant waveforms have been identified (analytically or numerically), their stability as well as those of the ghost states in certain regimes is examined by means of linearization in the vicinity of stationary points. This reveals diverse and, occasionally, fairly complex bifurcations. The evolution of unstable modes is explored by means of direct simulations.

# TABLE OF CONTENTS

# LIST OF FIGURES

xiii

xiv

# CHAPTER 1

# INTRODUCTION

In quantum mechanics, energy of a quantum system is described by an operator called Hamiltonian, which acts on the Hilbert space (or a space of wave functions) of the system and corresponds to the total energy of the system, usually denoted by $H$, $\hat{H}$ or $\mathcal{H}$. The Hamiltonian is the sum of the kinetic energies of all the particles, plus the potential energy of the particles associated with the system. The spectrum of Hamiltonian is the set of possible outcomes when one measures the total energy of a system. Because of its close relation to the time-evolution of a system, it is of fundamental importance in most formulations of quantum theory. In the Universe in which we live, measurements of physical observables yield real quantities. In quantum mechanics these observables correspond to the eigenvalues of operators, and the reality requirement of observables demands that the eigenvalues of all operators be real quantities. In the case of the Hamiltonian operator $\mathcal{H}$, the real eigenvalues correspond to a real energy spectrum. In order to provide a real spectrum, one often imposes the Hermiticity condition $\mathcal{H}^\dagger = \mathcal{H}$ on the Hamiltonian, where $\mathcal{H}^\dagger$ represents the mathematical operation of complex conjugation and matrix transposition. And indeed, a Hermitian Hamiltonian not only ensures that the energy spectrum is real but it also takes care of the unitary temporal evolution.

In a remarkable recent development Bender and coworkers [1] have shown that it is possible to formulate quantum mechanics consistently even if the Hamiltonian and other observables are not Hermitian. In particular they explored the spectra of non-Hermitian Hamiltonians and found that in fact many non-Hermitian Hamiltonians can produce entirely real spectra provided they possess something known as $\mathcal{PT}$ (parity-time) symmetry.

Their formulation, dubbed $\mathcal{PT}$ quantum mechanics, replaces hermiticity by another set of requirements, notably that the Hamiltonian should be invariant under the discrete symmetry $\mathcal{PT}$. The actions of the parity, $\mathcal{P}$, and time reversal, $\mathcal{T}$, operators are defined as follows:

$$P : p \rightarrow -p,\ x \rightarrow -x;\ T : p \rightarrow -p,\ x \rightarrow -x,\ i \rightarrow -i. \qquad (1.1)$$

where $p$ and $x$ are the momentum and position operators, respectively. A Hamiltonian is defined as $\mathcal{PT}$-symmetric if it shares the same eigenfunctions as the $\mathcal{PT}$ operator and satisfies $\mathcal{PTH} = \mathcal{HPT}$. If $\mathcal{PTH} = \mathcal{HPT}$ is satisfied but the Hamiltonian does not share its eigenfunctions with the $\mathcal{PT}$ operator then the Hamiltonian is considered to possess broken $\mathcal{PT}$ symmetry.

The work of Bender [1] demonstrated that in many cases a threshold exists in the Hamiltonians, above which the spectrum is no longer completely real and instead becomes complex. This threshold marks the boundary between the $\mathcal{PT}$-symmetric and broken-symmetry phases and the transition is thus referred to as spontaneous $\mathcal{PT}$-symmetry-breaking. A necessary (but not sufficient) condition for a Hamiltonian to be $\mathcal{PT}$ symmetric is that its potential $V(x)$ satisfies the condition $V(x) = V^*(-x)$.

$\mathcal{PT}$-symmetric systems are interesting because they are intermediate between open systems (systems in contact with an external environment) and closed (isolated) systems. An open system typically suffers loss to or gain from its environment and thus cannot be in equilibrium. A $\mathcal{PT}$-symmetric system is special because, while it is in contact with the environment, the loss and gain are precisely balanced. The loss and gain may be widely separated, but, if the parameters of the system are adjusted to support a sufficiently rapid internal circulation, the system can be in equilibrium and thus mimic a closed system. A $\mathcal{PT}$-symmetric system in equilibrium (that is, one for which the system has an unbroken $\mathcal{PT}$ symmetry) typically exhibits oscillations between its modes. However, if the parameters of the system are varied to weaken sufficiently the internal circulation, the

oscillations cease. This is the signal that the system has undergone a transition to a broken $\mathcal{PT}$-symmetric phase and is no longer in equilibrium.

In the past few years, a significant vein of potential applications of such Hamiltonians has been initiated, predominantly so in the field of nonlinear optics. There, the work of Christodoulides and co-workers [2] gave rise to the realization that the synthetic systems that can be engineered therein enable a potential balance of gain (through suitable amplifiers) and the abundantly present losses in order to produce experimental realizations of $\mathcal{PT}$-symmetric systems. An additional feature present in such settings which made both their theoretical and experimental investigation even more interesting was the presence of nonlinearity which, in turn, rendered worthwhile the exploration of the dynamics of nonlinear waves (such as bright or gap solitons [2] and more recently of dark solitons and vortices [3]). The above optical settings were in fact the ones that enabled the first experimental realizations of $\mathcal{PT}$-symmetry. This was done in the context of waveguide couplers (i.e., either two waveguides with and without loss [4] – the so-called passive $\mathcal{PT}$– or in the more "standard" case of one waveguide with gain and one with loss [5]). More recently, electrical analogs of such systems have been engineered in the work of [6]. In parallel to these pioneering steps in the realm of experiments, numerous theoretical investigations have arisen both in the context of linear $\mathcal{PT}$-symmetric potentials [7, 8, 9, 10, 11, 12, 13, 14, 15, 16, 17, 18, 19, 20, 21, 22] and even in the case of the so-called nonlinear $\mathcal{PT}$-symmetric potentials (whereby a $\mathcal{PT}$-symmetric type of gain/loss pattern appears in the nonlinear term) [23, 24, 25].

Our aim in this thesis is to give a broad picture of the $\mathcal{PT}$-symmetric discrete linear and nonlinear, one-dimensional and two-dimensional states in so-called oligomers of two and more sites lattices, as well as in lattices with different types of potentials. A complete characterization of the existence and stability properties of its stationary solutions and properties of a new class of, so-called, "ghost" solutions of one-dimensional linear lattices are also introduced. Our presentation is structured as follows: In chapter 2, we consider one-

dimensional linear oligomers, namely the two-site dimer, three-site trimer and the four-site quadrimer. Both analytical and numerical solutions are provided and the "ghost solutions" are investigated in these cases. As a special case, $\mathcal{PT}$-symmetric coupler with $\chi^2$ nonlinearity is discussed at the end of this chapter. Chapter 3 shows the cases where gain/loss terms exist in the nonlinearity. Existence of both symmetric and asymmetric (in their amplitude) stationary solutions, and interesting bifurcation phenomena (such as spontaneous symmetry breakings) are found to arise in this case. Two-dimensional $\mathcal{PT}$-symmetric plaquettes are shown in Chapter 4. Three four-site squares and one five-site cross modes are presented here. We address the existence and stability of all families of stationary solutions, as well as their bifurcation diagrams. Dynamical evolution is also performed by means of direct simulation. In Chapter 5, we consider a $\mathcal{PT}$-symmetric coupler whose arms are birefringent waveguides. In this case, We obtain the relevant symmetry-breaking bifurcations between symmetric (circularly polarized) and asymmetric (elliptically polarized) states and examine the corresponding nonlinear solutions that persist up to the symmetry breaking point, as well as the ghost states that bifurcate from them.

# CHAPTER 2

# ONE DIMENSIONAL LINEAR $\mathcal{PT}$-SYMMETRIC OLIGOMERS

In this chapter, we consider the existence, stability, and dynamics of $\mathcal{PT}$-symmetric oligomers, i.e., configurations with one dimensional two sites (dimer), three sites (trimer) and four sites (quadrimer). Fig. 2.1 illustrates the gain or loss profiles among these fundamental one-dimensional $\mathcal{PT}$-symmetric oligomers. At the end of this chapter, we also introduce a special type of one-dimensional linear coupler, which has a $\chi^2$ nonlinearity.



| (a) dimer | (b) trimer | (c) quadrimer |
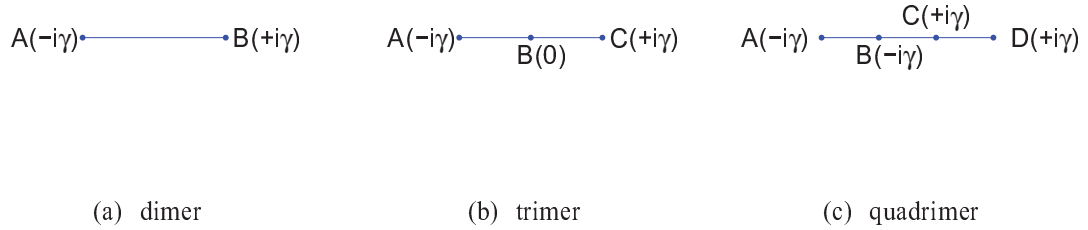
**Figure 2.1.** (Color online) The different fundamental one-dimensional $\mathcal{PT}$-symmetric oligomers including the linear balanced gain and loss. The nodes are labeled so as to connect the gain-loss profiles to the evolution of individual nodes in dynamical simulations. The sets are coded by chains of symbols, with $+, -$ and $0$ corresponding, respectively, to the linear gain, loss, or absence of either effect at particular sites.

## I $\mathcal{PT}$-symmetric dimer

We start our considerations from the so-called $\mathcal{PT}$-symmetric coupler or dimer. In this case, the dynamical equations that we examine are of the form:

$$\begin{aligned} i\dot{u}_1 &= -ku_2 - |u_1|^2 u_1 - i\gamma u_1 \\ i\dot{u}_2 &= -ku_1 - |u_2|^2 u_2 + i\gamma u_2. \end{aligned} \tag{2.1}$$

The model of Eq. (2.1) considers the linear $\mathcal{PT}$-symmetric dimer experimentally examined in [5], as augmented by the Kerr nonlinearity relevant e.g. to optical waveguides; see also [7, 8]. The overdot denotes the derivative with respect to the evolution variable which in optical applications is the propagation distance. In what follows, we will denote this variable by $t$ (to indicate its evolutionary nature). We seek stationary solutions of the form $u_1 = \exp(iEt)a$ and $u_2 = \exp(iEt)b$. Then the stationary equations arise:

$$\begin{aligned} Ea &= kb + |a|^2 a + i\gamma a \\ Eb &= ka + |b|^2 b - i\gamma b. \end{aligned} \tag{2.2}$$

Using a generic polar representation of the two "sites" $a = Ae^{i\phi_a}$ and $b = Be^{i\phi_b}$, we are led to the following algebraic conditions for the two existing branches of solutions (notice the $\pm$ sign distinguishing between them):

$$A^2 = B^2 = E \pm \sqrt{k^2 - \gamma^2} \tag{2.3}$$

$$\sin(\phi_b - \phi_a) = -\frac{\gamma}{k} \tag{2.4}$$

The fundamental difference of such solutions from their standard Hamiltonian ($\gamma = 0$) counterpart is that the latter were lacking the "flux condition" of Eq. (2.4). This dictated a selection of the phases so that no phase current would arise between the sites. On the contrary, in $\mathcal{PT}$-symmetric settings, the phase flux is nontrivial and must, in fact, be consonant with the gain-loss pattern of the coupler.

Fig. 2.2 shows the profile of the two branches. The branch in dashed line corresponding to the $(-)$ sign in Eq. (2.3) is stable when $\gamma^2 \leq k^2 - E^2/4$, whereas the branch in solid line
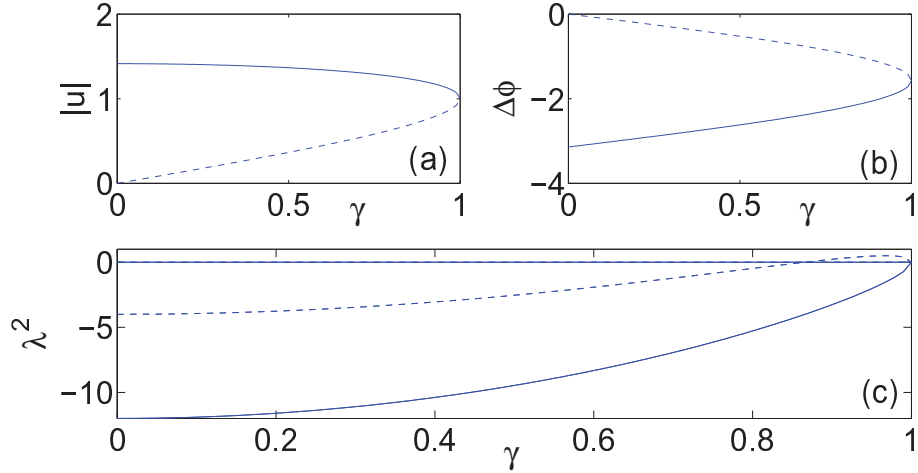
**Figure 2.2.** (Color online) The two branches of solutions for the dimer problem are shown for parameter values $k = E = 1$. (a) The amplitude of the sites,(b) their relative phase, and (c) the (nontrivial) squared eigenvalue of the two branches. The solid line branch is always stable branch, while the dashed line branch acquires a real eigenvalue pair above a certain $\gamma = \sqrt{k^2 - E^2/4}$.

is always stable. It is relevant to note here that the two branches "die" in a saddle-center bifurcation at $\gamma = k$, as shown in the figure. Importantly, this coincides with the linear limit $\gamma_{PT} = k$ of the PT-symmetry breaking since the eigenvalues of the linear problem are $\lambda = \pm\sqrt{k^2 - \gamma^2}$. Hence, the nonlinear solutions terminate where the linear problem eigenfunctions yield an imaginary pair, predisposing us for an asymmetric evolution past this critical point (for all initial data). The dynamical evolution of the dimer is shown first for a case of $\gamma < k$ (in which the dashed line branch is unstable, while the solid line branch is stable) in Fig. 2.3. The evolution of the instability of the dashed line branch leads to an asymmetric distribution of the power in the coupler, despite the fact that parametrically we are below the linear critical point (for the $\mathcal{PT}$-symmetry breaking). Notice that in all the cases, also below, where a stationary solution exists for the parameter values for which it is initialized, dynamical instabilities arise only through the amplification of roundoff errors i.e., a numerically exact solution up to $10^{-8}$ is typically used as an initial condition in

the system. Naturally, beyond $\gamma = k$, as shown in Fig. 2.4, all initial data yield such an asymmetric evolution.
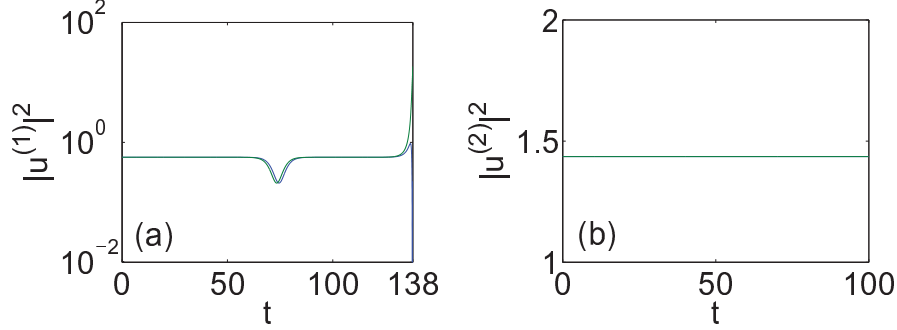


**Figure 2.3.** (Color online) Dynamical evolution of initial data belonging to the two branches of stationary solutions of a dimer in the case of $\gamma = 0.9$, $E = k = 1$, which is past the critical point for the instability of the (a) first branch, while the (b) second branch is still dynamically stable. Notice that (a) is plotted in semilog.
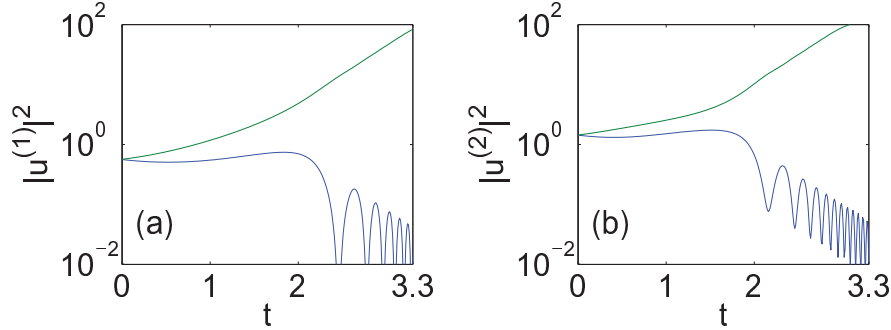


**Figure 2.4.** (Color online) Similar initialization as Fig. 2.3 of the dimer based on the two branches of stationary solutions (for $\gamma = 0.9$), but now for the case of $\gamma = 1.1$ ($E = k = 1$). The asymmetric evolution of the coupler past the linear $\mathcal{PT}$-symmetric threshold can be clearly discerned. Both are plotted in semilog.

The linearization around these branches can be performed explicitly yielding the nonzero eigenvalue pairs

$$\pm 2i\sqrt{2(k^2 - \gamma^2) - E\sqrt{k^2 - \gamma^2}}$$

for the first and

$$\pm 2i\sqrt{2(k^2 - \gamma^2) + E\sqrt{k^2 - \gamma^2}}$$

for the second (notice that the latter can never become real). For the case $\gamma = 0$, these eigenvalues describe the critical value of $E$, where the two branches become unstable, and the pitchfork bifurcation leading to the asymmetric states emerges. Specifically, if $k > 0$ (focusing nonlinearity), the first branch corresponding to the symmetric solutions becomes unstable at $E = 2k$ ; if $k < 0$ (defocusing nonlinearity), the destabilization arises when $E = -2k$ , and this happens for the second branch corresponding to the antisymmetric branch $\theta = \pi$ .

Similar stability conclusions occur for $\gamma \neq 0$ , where only the "–" branch becomes unstable, but now also for $\gamma^2 \geq k^2 - E^2/4$ . This suggests that there are two possibilities. If the propagation constant $E$ (and the coupling strength $k$) are such that $E^2 < 4k^2$, then the instability is induced by the increase of the $\mathcal{PT}$ symmetry parameter $\gamma$ at the critical point. However, if $E^2 > 4k^2$ , the instability has "already" taken place due to the presence of nonlinearity, and the "–" branch is unstable even in the $\gamma = 0$ limit. In the latter case the presence of the gain-loss aspect only enhances the instability.

What has become of the pitchfork bifurcation picture explored earlier? We can see that the same instability is present here at least if $E^2 > 4k^2$. However, analogs of the symmetry-broken states past the critical point, i.e., stationary asymmetric states (emerging after the instability of the symmetric states), cannot be identified. Inevitably, the question of their fate arises. This type of question was initially raised in Ref. [26] (where a leaky quantum dimer, with loss only, was considered) and, past a critical point, states with a complex (instead of real) "eigenvalue" $E$ were identified. In the $\mathcal{PT}$-symmetric context, a similar idea was put forth in Ref. [27] for a double well consisting of two delta functions. In this thesis we unify the approaches of Ref. [26] and [27] by computing the "ghost states" (as we characterize them) that emerge from the symmetry-breaking bifurcation. Before presenting the computation of the ghost states, we comment that these states with complex (nonlinear) eigenvalue $E$ are no longer true solutions of the original system Eq. 2.1. This is because of the $U(1)$ invariance of the system, which only allows stationary solutions

with real $E$ [so that $|\exp(iEt)|^2 = 1$]. When this symmetry is violated, the solutions may satisfy the stationary equations Eq. 2.2, but are only ghost states of the original dynamical system because they do not satisfy Eq. 2.1. Thus, at best one expects that the dynamics may stay close to the dynamics of these ghost states, especially during the evolution of the symmetry-breaking instability. We return to this topic later. To identify these stationary solutions, we introduce polar coordinates $E \to E \exp(i\phi_e)$ and get

$$
\begin{aligned}
AE \cos \phi_e &= kB \cos \theta + A^3 \\
BE \cos \phi_e &= kA \cos \theta + B^3 \\
AE \sin \phi_e &= kB \sin \theta + \gamma A \\
BE \sin \phi_e &= -kA \sin \theta - \gamma B,
\end{aligned}
\tag{2.5}
$$

where $\theta = \phi_b - \phi_a$. To derive the asymmetric $(A \neq B)$ solutions, we rewrite these equations as

$$
\cos \theta = \frac{AB}{k} \tag{2.6}
$$

$$
\sin \theta = -\frac{2\gamma AB}{k(A^2 + B^2)} \tag{2.7}
$$

$$
\cos \phi_e = \frac{A^2 + B^2}{E} \tag{2.8}
$$

$$
\sin \phi_e = \frac{\gamma(A^2 - B^2)}{E(A^2 + B^2)} \tag{2.9}
$$

Applying the identity $\sin^2 x + \cos^2 x = 1$ to Eq. 2.6-2.7, we obtain a condition for the solution amplitudes, and the same identity applied to Eq. 2.8-2.9 yields the parameter $E$. These solutions exist only for $\gamma^2 > k^2 - E^2/4$ . If $E^2 > 4k^2$, they exist for all values of $\gamma$ (i.e., they have bifurcated already due to the nonlinearity). Also, these solutions terminate as $\theta \to -\pi/2$, $\phi_e \to \pi/2$. In turn, this implies that in this limit both $B$ and $A$ vanish, with the ratio between them having the limit $B/A \to (\gamma \pm \sqrt{\gamma^2 - k^2})/k$. Thus, we have identified the disappearance point $\gamma^2 = E^2 + k^2$ of these symmetry-broken solutions.

10

Finally, we discuss the disappearance of the two symmetric states at the critical point $\gamma = k$
, which is the phase-transition point of the linear (and nonlinear) problem. We have shown
that at this point the symmetry-broken states still exist, but that now they are only ghost
states of the steady-state problem. From the point of view of nonlinear theory, one may be
content to find a saddle-center bifurcation at this point, which leads to the disappearance of
these solutions as stationary states of the nonlinear problem. Yet, once again, when these
solutions disappear (even in the normal form of such a bifurcation) this means that they
appear somewhere else within the complex plane of solutions. In order to compare this
result with the linear $\mathcal{PT}$-symmetric case, where the eigenvalues collide, become complex,
and continue to exist in the complex plane, we follow Ref. [27] and consider the analytic
continuation of our solutions. In the $\mathcal{PT}$-symmetric regime up to the critical point, the
solutions are chosen so that $u^*(x) = u(-x)$. (This is a broader statement for a spatially
distributed system; in our simpler dimer setting, we need only replace $x$ by the subscript 1
and $-x$ by the subscript 2, or vice-versa.) Thus, to perform the analytic continuation, we
use $u_j^* = u_{3-j}$ in Eq. 2.1, which leads to Eq. 2.5, but in the first pair of equations $A^3$ and
$B^3$ are replaced by $A^2B$ and $B^2A$ . The result is

$$\frac{B}{A} = \frac{\gamma \pm \sqrt{\gamma^2 - k^2}}{k} \tag{2.10}$$

$$\cos\phi_e = \frac{AB}{E} \tag{2.11}$$

$$\sin\phi_e = \frac{\gamma(A^2 - B^2)}{E(A^2 + B^2)} \tag{2.12}$$

$$\theta = -\frac{\pi}{2} \tag{2.13}$$

Note that the pitchfork symmetry-breaking branches also tend to this solution, as shown
above in the expression for $B/A$ in the limit of termination of the branch when $\gamma =
\sqrt{k^2 + E^2}$. We have made an additional subtle assumption here, namely, that $\theta_a + \theta_b = 0$.
We can obtain more general solutions without this assumption, but these do not appear to
introduce new features to the problem. The solutions stemming from the analytic contin-

11

uation provide a complete description of the states of the system. We move from symmetric/antisymmetric states to asymmetric ones (which may be ghost states) through a pitchfork bifurcation, destabilizing the symmetric (antisymmetric) branch for a focusing (defocusing) nonlinearity. We terminate at the point of the linear $\mathcal{PT}$ phase transition, where the nonlinear eigenvalues of the symmetric branches collide and become complex, giving rise to an analytic continuation of our solutions in the complex plane. All solutions terminate at $\gamma = \sqrt{k^2 + E^2}$. See Fig. 2.5 for a relevant bifurcation diagram.

Fig. 2.6 shows the evolutionary plots of the ghost solutions (blue solid line) for $\gamma = 0.9$, $E = k = 1$. With $E = E_r + iE_i$ being complex, the ghost state solutions under the form $u_1 = \exp(iEt)a$ and $u_2 = \exp(iEt)b$ should evolve exponentially, as indicated by red dashed lines in both panels. In particular, the black squares branch with negative $E_i$ is expected to lead to growth (for both nodes of the dimer), while the green stars branch with positive $E_i$ is anticipated to decay (again for both nodes). The slopes of these growth/decay features are given by $-2E_i = -2E \sin \phi_e$. However, in line with their anticipated linear "instability", neither of these follows exactly the dynamics anticipated above. Both of them evolve for a short period according to the expected growth or decay, and then the gain sites start to grow and the loss sites start to decay, regardless of the trend predicted by the form of the ghost state (as discussed above).

## II  $\mathcal{PT}$-symmetric trimer

We now turn to the case of the trimer where the dynamical equations are

$$
\begin{aligned}
i\dot{u}_1 &= -ku_2 - |u_1|^2 u_1 - i\gamma u_1 \\
i\dot{u}_2 &= -k(u_1 + u_3) - |u_2|^2 u_2 \\
i\dot{u}_3 &= -ku_2 - |u_3|^2 u_3 + i\gamma u_3
\end{aligned}
\tag{2.14}
$$

Seeking once again stationary solutions leads to the algebraic equations
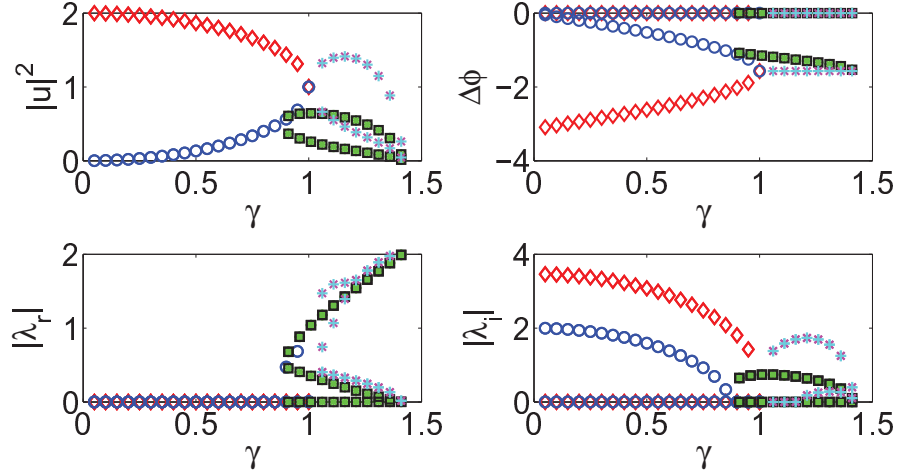
**Figure 2.5.** (Color online) Ghost states (denoted by cyan pluses and black squares) bifurcate from the two stationary solutions (denoted by blue circles and red diamonds) of a dimer. Under parameter values $k = 1$ and $E = 1$, the black squares branches emerge from a pitchfork bifurcation of the blue circles branch at $\gamma = 0.87$ and terminate at $\gamma = 1.41$.



(a) black squares branch          (b) green stars branch
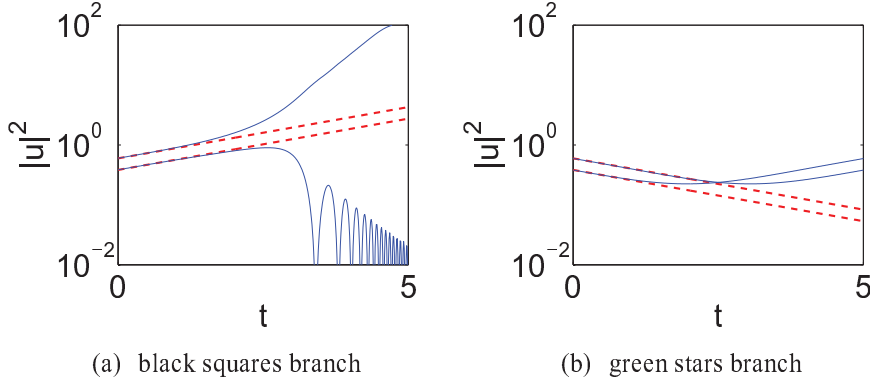
**Figure 2.6.** (Color online) The evolutionary plots of the two ghost solutions of dimer for $\gamma = 0.9$, $E = k = 1$. The dashed lines are the predicted dynamics of the ghost states on the basis of their growth rates (for black squares) or decay rates (for green stars).

$$Ea = kb + |a|^2 a + i\gamma a$$

$$Eb = k(a + c) + |b|^2 b$$

$$Ec = kb + |c|^2 c - i\gamma c \qquad (2.15)$$

13

In this case too, it is helpful to use the polar representation for the three-sites in the form $a = Ae^{i\phi_a}, b = Be^{i\phi_b}, c = Ce^{i\phi_c}$, which, in turn, leads to the algebraic equations of the form:

$$A = C \tag{2.16}$$

$$B^4 - EB^2 + 2EA^2 - 2A^4 = 0 \tag{2.17}$$

$$\sin(\phi_b - \phi_a) = -\sin(\phi_b - \phi_c) = -\frac{\gamma A}{kB} \tag{2.18}$$

$$\cos(\phi_a - \phi_b) = \cos(\phi_b - \phi_c) = \frac{EA - A^3}{kB} \tag{2.19}$$

In turn, the algebraic polynomial equation for the squared amplitude of $A^2 \equiv x$ is given by

$$x[\gamma^2 + (E - x)^2]^2 - k^2 E[\gamma^2 + (E - x)^2] - 2k^4 x + 2k^4 E = 0 \tag{2.20}$$

Notice how the presence of the gain-loss spatial profile along the three sites induces a spatial phase distribution and enforces the condition of a symmetric amplitude profile with the first and third site sharing the same amplitude. This phase distribution would be trivial (relative phases of $0$ or $\pi$) in the $\gamma = 0$ case.

As mentioned above, in addition to the regular stationary solutions for which $E$ is real, one can seek additional solutions with $E$ being complex, i.e., $E = \hat{E} \exp(i\phi_e)$ The resulting waveforms are quite special in that they are solutions of the stationary equations of motion (2.15), yet they are *not* solutions of the original dynamical evolution equations (2.14), because of the imaginary part of $E$. Such "ghost state" solutions have recently been identified in the case of the $\mathcal{PT}$-symmetric dimer [27, 28, 22] and have even been argued to play a significant role in its corresponding dynamics therein. In the case of the trimer, they are presented here. Such ghost trimer states will satisfy the following algebraic conditions:

$$\sin\phi_a = \frac{A\left(B^2 + 2C^2\right)\gamma}{B\left(A^2 + B^2 + C^2\right)k} \tag{2.21}$$

$$\cos\phi_a = \frac{A(B - C)(B + C)\left(-A^2 + B^2 + C^2\right)}{B\left(-A^2 + B^2 - C^2\right)k} \tag{2.22}$$

$$\sin\phi_c = -\frac{\left(2A^2 + B^2\right)C\gamma}{B\left(A^2 + B^2 + C^2\right)k} \tag{2.23}$$

$$\cos\phi_c = \frac{\left(-A^2 + B^2\right)C\left(A^2 + B^2 - C^2\right)}{B\left(-A^2 + B^2 - C^2\right)k} \tag{2.24}$$

$$\sin\phi_e = \frac{(A - C)(A + C)\gamma}{\left(A^2 + B^2 + C^2\right)\hat{E}} \tag{2.25}$$

$$\cos\phi_e = \frac{A^4 - B^4 + C^4}{\left(A^2 - B^2 + C^2\right)\hat{E}}, \tag{2.26}$$

From these equations, the amplitudes $A$, $B$, $C$ can be algebraically identified by applying the identity $\sin^2\phi + \cos^2\phi = 1$ for each of the above angles. The relevant six algebraic equations lead to the identification of the six unknowns, namely the three amplitudes, as well as the phases $\phi_a$, $\phi_c$ and $\phi_e$ (for simplicity we have set $\phi_b = 0$ hereafter, without loss of generality). It should be noted here that should such ghost state solutions be present with $\phi_e \neq 0$, these will spontaneously break the $\mathcal{PT}$ symmetry, given that they will have $A \neq C$.

Notice that for each branch of solutions that we identify in what follows, we will also examine its linear stability. This will be done through a linearization ansatz of the form $u_i = e^{iEt}[v_i + \epsilon(p_i e^{\lambda t} + \bar{q}_i e^{\bar{\lambda}t})]$. Here the $v_i$'s for $i = 1, 2, 3$ will denote the values of the field at the standing wave equilibria, while $\lambda$ are the corresponding eigenvalues and $(p_i, q_i)$ for $i = 1, 2, 3$ denote the elements of the corresponding eigenvector which satisfies the linearization problem at $\mathrm{O}(\epsilon)$; the overbar will be used to denote complex conjugation. When the eigenvalues $\lambda$ of the resulting $6 \times 6$ linearized equations have a positive real part, the solutions will be designated as unstable (whereas otherwise they will be expected to be dynamically stable). We now turn to the detailed numerical analysis of the corresponding stationary, as well as ghost branches of solutions. Since Eq. (2.20) is a polynomial of degree 5, we expect at most 5 distinct real roots (and at least 1 such). Indeed for suitable choices

15

of the free parameters $(E, k)$, we identify five branches of stationary solutions. Figure 2.7 illustrates a situation with five branches under $E = 0.5$ and $k = 0.1$. Two of them, denoted by blue circles and red diamonds, collide and terminate at $\gamma = 0.1$. The blue circles are essentially stable while the red diamonds are unstable. Another pair of branches, namely the magenta squares and green pluses collide and terminate at $\gamma = 0.02$, with the magenta squares being stable and the green pluses being unstable (i.e., both of the above collisions are examples of saddle-center bifurcations). The black crosses branch, which is essentially unstable, persists beyond $\gamma = 0.1$. Notice that the amplitudes of the different nodes for this branch shown in the top left panel of the figure are not constant: the upper line (standing for $B$) is slightly increasing and the lower line (standing for $A = C$) is slightly decreasing.
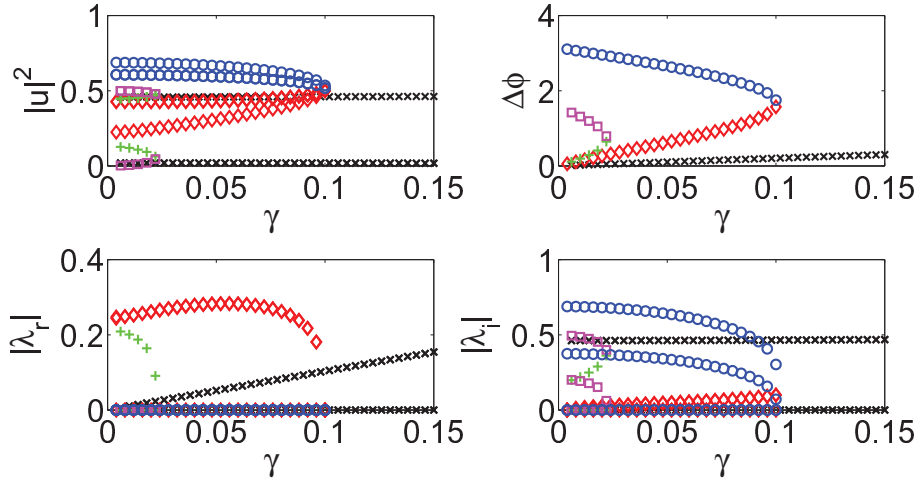


**Figure 2.7.** (Color online) The solution profile of Eq. (2.14) with $E = 0.5$, $k = 0.1$ and $\phi_b = 0$. The four panels denote the solution amplitude (top left), phase differences between adjacent nodes (top right), real and imaginary parts (second row) of eigenvalues.

In the following, we focus on a typical example of the branches (both stationary and ghost ones) for a selection of the free parameters of order unity, more specifically for $E = k = 1$; cf. Fig. 2.8. We identify three distinct examples of stationary states denoted by the blue circle, red diamond and black cross branches. The blue circle and red diamond branches stem from the corresponding "+0–" and "–+–" branches, respectively, namely

the second and third excited state of the Hamiltonian trimer problem of $\gamma = 0$; cf. with Ref. [29]. The blue circles branch is mostly unstable, except for a small interval of $\gamma \in [1, 1.035]$, while the red diamonds branch is chiefly stable, except for the narrow interval of values of $\gamma \in [1.035, 1.043]$. In this narrow interval, the eigenvalues of both of these branches are very close to each other. For the blue circles branch, we also note that two eigenvalue pairs stemming from a complex quartet collide on the imaginary axis at $\gamma = 1$ and split as imaginary thereafter. One of these pairs exits as real for $\gamma > 1.035$, and the two branches (blue circles and red diamonds) collide shortly thereafter, i.e., at $\gamma = 1.043$.
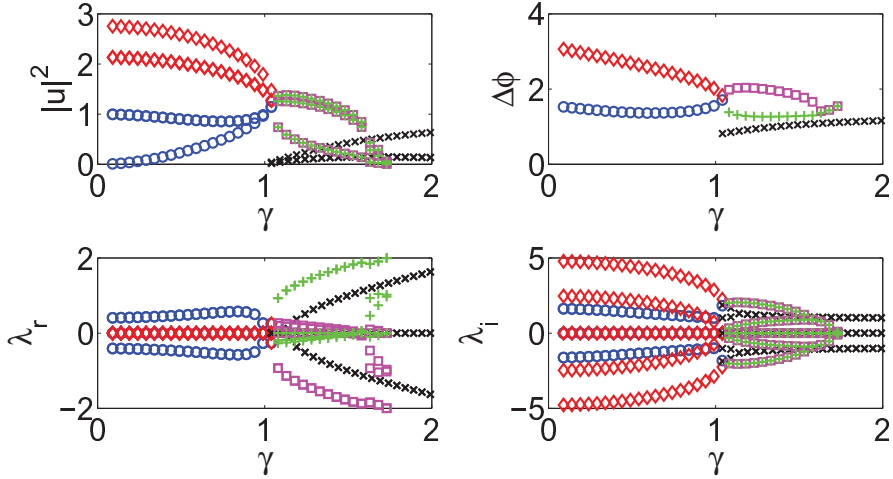


**Figure 2.8.** (Color online) In a way similar to that of the previous figure (i.e., with top left denoting amplitudes, top right relative phases, bottom left real and bottom right imaginary part of the linearization eigenvalues), the 4 panels show the existence and stability of solutions for a trimer with parameters $E = k = 1$. There are three regular standing wave branches: the blue, the red and the black; the blue and red are the ones disappearing hand-in-hand at $\gamma = 1.043$. Two ghost solutions are colored in magenta and green and bifurcate at the destabilization of the blue branch for $\gamma = 1.035$, while they terminate for $\gamma = 1.732$.

Interestingly, however, these are not the only branches that arise in the trimer case. In particular, as can be seen in Fig. 2.8, there is a branch of solutions bifurcating from zero (amplitude) for $\gamma > \sqrt{2k^2 - E^2}$, denoted by the black crosses in Fig. 2.8. In our case $E = k = 1$, this branch is only stable for $\gamma < 1.13$, at which point two pairs of imaginary eigenvalues collide and lead to a complex quartet, which renders the branch

17

unstable thereafter. Yet, this branch of solutions has a remarkable trait. In the case of the trimer, the underlying linear problem possesses the following eigenvalues: $0, \pm\sqrt{2k^2 - \gamma^2}$. Hence, the critical point for the existence of real eigenvalues of the linear problem in the case of the $\mathcal{PT}$-symmetric trimer is $\gamma_{PT} = \sqrt{2}k$ (cf. with the $\gamma_{PT} = k$ limit of the dimer). Nevertheless, and contrary to the case for the dimer, the third branch of solutions considered above persists beyond this critical point (although it is unstable in that regime).

In Fig. 2.8, in addition to the standard stationary solutions, the ghost state solutions are also shown. These are designated by the magenta squares and green pluses in the figure. These ghost solutions are also obtained for $\hat{E} = k = 1$, and importantly (and contrary to what is the case for the stationary states), they bear distinct amplitudes in all three sites. The two (magenta and the green) branches shown in the figure are mirror images of each other, i.e., $A, B, C$ in the magenta branch are the same as $C, B, A$ in the green branch, respectively, and their phase difference and eigenvalues are opposite to each other. Notice that as indicated above the difference in the magnitudes of $A$ and $C$ supports the fact that these branches defy the expectations of the $\mathcal{PT}$ symmetry. Indeed, both of the branches arise through a symmetry-breaking bifurcation from the blue branch when it becomes unstable at $\gamma = 1.035$. Furthermore, it should be noted that the branches terminate at vanishing amplitude for $\gamma = 1.732$. It is interesting to point out that when performing linear stability analysis of these states, we find *both* of them to be unstable. Case examples of the linearization results for both the regular states and the ghost ones are shown for three different values of $\gamma$ in Fig. 2.9. For $\gamma = 0.5$, the red diamond branch is (marginally) stable, while the blue circle branch bears the instability that we discussed above for $\gamma < 1$. For $\gamma = 1.5$, only the black branch is present among the stationary ones and the magenta and green ghost state branches manifest their respective asymmetries with spectra that are *asymmetric* around the imaginary axis. This is a characteristic feature of the ghost states; see also [22, 30]. Although among the two branches, the magenta is more stable and the green highly unstable, even the magenta branch is predicted to be weakly unstable with

a small real positive eigenvalue. We will examine the dynamical implications of these instabilities in what follows. The last panel similarly shows the case of $\gamma = 1.7$ shortly before the disappearance of the ghost state branches.
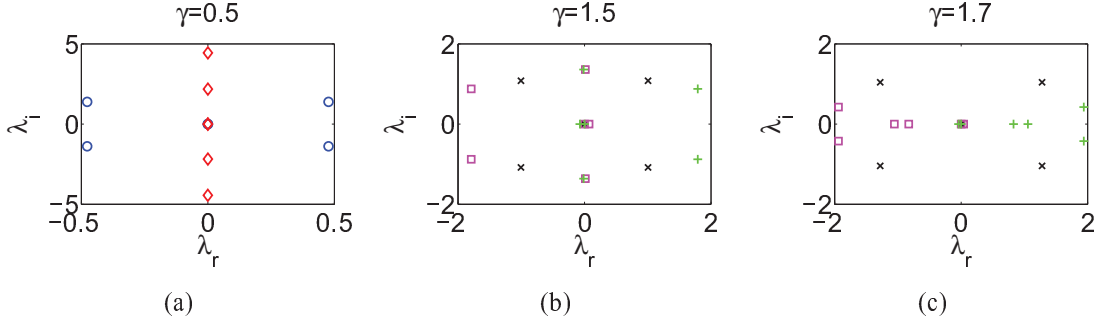


**Figure 2.9.** (Color online) The spectral planes $(\lambda_r, \lambda_i)$ of the eigenvalues $\lambda = \lambda_r + i\lambda_i$ of the solutions shown in Fig. 2.8. The first panel shows the case of $\gamma = 0.5$ where only the standing wave branches exist (blue circles – unstable and red diamonds – stable). The second panel for $\gamma = 1.5$ has only one standing wave (black crosses – unstable), and two asymmetric ghost states which are mirror images of each other (and so are their spectra), namely magenta squares and green pluses. The third panel shows the same branches as in top right but for $\gamma = 1.7$ close to the termination of the ghost state branches.

Finally, we examine the dynamics of the different branches in Fig. 2.10. The top row panels of the figure show the evolution of the three stationary branches. Panels (a) and (b) show the blue circle branch for $\gamma = 0.5$ and $\gamma = 1.1$, while panel (c) depicts the red diamond standing wave branch for $\gamma = 1.1$. It can be seen that in accordance with the predictions of our linear stability analysis, the first two branches are stable or unstable in their corresponding regimes, while past the point of existence of these branches ($\gamma = 1.043$), their evolution gives rise to asymmetric dynamics favoring the growth of the power in a single site [or, in some cases, even in two sites; see, e.g., Figs. 2.10(b) and 2.10(c)]. On the other hand, for the branch emerging at $\gamma = 1$ and persisting past the linear instability limit, we indeed find it to be stable for $\gamma < 1.13$ and unstable thereafter, again leading to an asymmetric distribution of the power. Notice that the cases of (b) and (c), the corresponding branches cease to exist at $\gamma = 1.043$. Thus in these runs, we have used the terminal point profile of the branches (at $\gamma = 1.043$) as initial data for the evolution with $\gamma = 1.1$.

Importantly, we note that in the unstable evolution of cases (b) and (c), two of the sites end up growing indefinitely while the lossy site ends up decaying. On the contrary, in the case (a), only the site with gain is led to growth, while the other two are led to eventual decay. In panel (d), we show the black crosses branch, the third among the standing wave solutions identified herein for $\gamma = 1.5$. Notice that panel (d) shows a different dynamical evolution from panels (b) and (c) and more in line with panel (a), showcasing that there are indeed two general growth scenaria: one in which the gain site "grabs" along the neutral central site and leads it to indefinite growth and one in which the central site is ultimately led to decay together with the lossy site.



(a) blue circles  (b) blue circles  (c) red diamonds  (d) black crosses

(e) magenta squares  (f) magenta squares  (g) green pluses  (h) green pluses
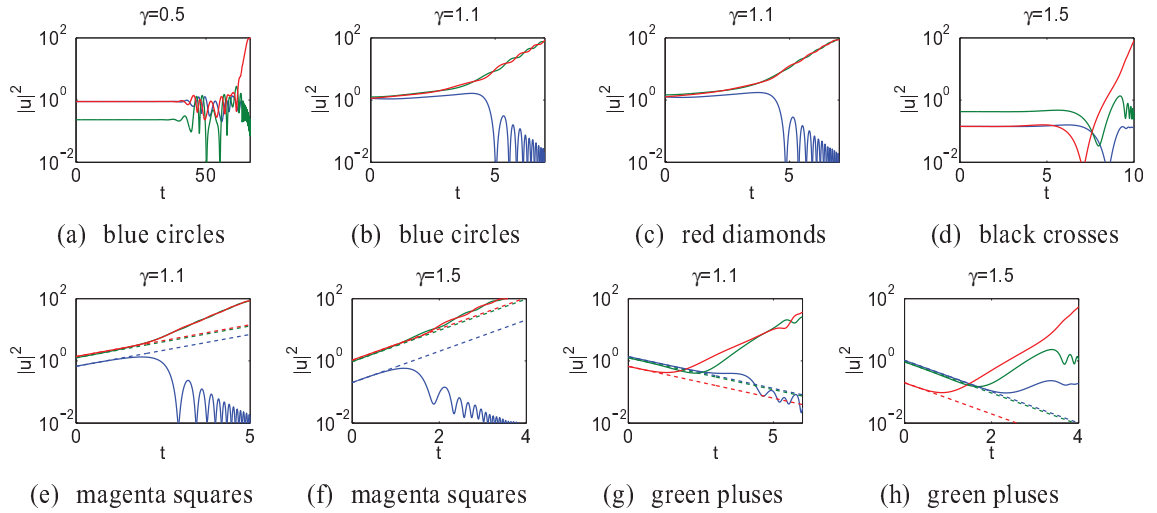
**Figure 2.10.** (Color online) The dynamical evolution of the amplitudes of the three sites for the solutions shown in Fig. 2.8. Notice that all solutions are plotted in semilog. The first row shows the evolution of the three stationary branches. In (b) and (c), since these branches are absent for $\gamma = 1.1$, their profile for $\gamma = 1.043$ is initialized. The second row shows dynamics of the two ghost state solution branches. The dashed lines are the predicted dynamics of the ghost states on the basis of their growth (for magenta squares) or decay (for green pluses) rates.

The four panels in the lower row show the dynamical evolution of the two ghost states (green pluses and magenta squares) for the cases of $\gamma = 1.1$ and $\gamma = 1.5$. Similarly as in the dimer case, the magenta squares branch with negative $E_i$ is expected to lead to exponential growth (for all three nodes of the trimer), while the green plus branch with

positive $E_i$ is anticipated to decay exponentially (again for all nodes). Once again, neither of these follows exactly the dynamics anticipated above. Both of them evolve for a short period according to the expected growth or decay, and then the gain sites start to grow and the loss sites start to decay, regardless of the trend predicted by the form of the ghost state. Moreover, it is relevant to note as regards the corresponding dynamics that the cases of the blue circle and red diamond branches of $\gamma = 1.1$ exhibit similar (asymptotic) dynamics to those of the magenta squares and of the green pluses for the same parameter value; i.e., the central site is also led to growth along with the gain one. On the other hand, it is also evident that the black crosses branch for $\gamma = 1.5$ instead follow an evolution resembling to the asymptotic evolution of the green pluses branch (which is different from that of the magenta squares for the latter value), i.e., here only the gain site is ultimately led to growth.

## III $\mathcal{PT}$-symmetric quadrimer

In this section, we briefly turn to the case of the quadrimer. Here the equations are

$$
\begin{aligned}
i\dot{u}_1 &= -ku_2 - |u_1|^2 u_1 - i\gamma u_1 \\
i\dot{u}_2 &= -k(u_1 + u_3) - |u_2|^2 u_2 - i\gamma u_2 \\
i\dot{u}_3 &= -k(u_2 + u_4) - |u_3|^2 u_3 + i\gamma u_3 \\
i\dot{u}_4 &= -ku_3 - |u_4|^2 u_4 + i\gamma u_4
\end{aligned} \tag{2.27}
$$

Notice here that we only consider the case where the first two sites have the same loss and the latter two the same gain. This is by no means necessary, and the gain-loss profile can be generalized to involve two parameters (e.g., $\pm\gamma_1$ and $\pm\gamma_2$ distinct between the different corresponding sites, i.e., the first and fourth ones, as well as the second and third ones)[31]. We do not consider this latter case here, due to its more complicated algebraic structure that does not permit the direct analytical results given below. More specifically, in our considered special case, the stationary equations read

$$
\begin{aligned}
Ea &= kb + |a|^2 a + i\gamma a \\
Eb &= k(a+c) + |b|^2 b + i\gamma b \\
Ec &= k(b+d) + |c|^2 c - i\gamma c \\
Ed &= kc + |d|^2 d - i\gamma d
\end{aligned}
\tag{2.28}
$$

The polar representation of the form $a = Ae^{i\phi_a}, b = Be^{i\phi_b}, c = Ce^{i\phi_c}, d = De^{i\phi_d}$ now allows the following reduced algebraic equations:

$$
A^2 + B^2 = C^2 + D^2 = E \tag{2.29}
$$

$$
A^2 B^4 + \gamma^2 A^2 - k^2 B^2 = 0 \tag{2.30}
$$

$$
D^2 C^4 + \gamma^2 D^2 - k^2 C^2 = 0 \tag{2.31}
$$

$$
\sin(\phi_b - \phi_a) = -\frac{\gamma A}{kB} \tag{2.32}
$$

$$
\sin(\phi_c - \phi_b) = -\frac{\gamma E}{kBC} = -1 \tag{2.33}
$$

$$
\sin(\phi_d - \phi_c) = -\frac{\gamma D}{kC}. \tag{2.34}
$$

Notice that in this case not only do we have the customary phase profile, but in fact one of the phase differences becomes locked to $\pi/2$ due to the presence of the gain-loss pattern.

Upon reducing the algebraic equations, we obtain

$$
(E - B^2)B^4 + \gamma^2(E - B^2) - k^2 B^2 = 0, \tag{2.35}
$$

$$
(E - C^2)C^4 + \gamma^2(E - C^2) - k^2 C^2 = 0, \tag{2.36}
$$

$$
\gamma E = kBC. \tag{2.37}
$$

This leads to the important conclusion that for this gain-loss profile in the case of the quadrimer, in contrast to the cases of the dimer and trimer, one of the parameters $E$, $k$, or $\gamma$ is determined by the other two; i.e., not all three of these parameters can be picked independently in order to give rise to a solution of the quadrimer.

We hereby set $E = 1$, and increase $\gamma$ from $0$ as before: then $k$ can be obtained self-consistently from the above equations. Therefore, once $E$ and $\gamma$ are fixed, the solutions of the quadrimer problem are fully determined. We now present three branches of solutions that arise in this setting as we increase $\gamma$. These are shown in the panels of Fig. 2.11. There are two classes of solutions here. The solid curve the blue circles branch corresponds to a fully asymmetric, always unstable branch with $A$, $B$, $C$, $D$ distinct, i.e., something that is unique (among the settings considered herein) to the quadrimer. On the other hand, the dashed curve of the branch the red diamonds branch and the dash-dotted curve of the branch the black crosses branch correspond to symmetric branches with amplitudes $A = D$ and $B = C$. Among the two symmetric branches the red diamonds branch and the black crosses branch that collide and disappear together in a saddle-center bifurcation at $\gamma = 0.362$, we can observe that the former has a real and two imaginary pairs of eigenvalues being always unstable, while the latter starts out stable, but the collision of two of its imaginary pairs will render it unstable past the critical point of $\gamma = 0.023$. Interestingly the asymmetric branch the blue circles branch and the symmetric branch the black crosses branch appear to collide in a subcritical pitchfork bifurcation that imparts the instability of the asymmetric branch to the symmetric one for $\gamma > 0.193$.

As an aside, we should also note here that in its linear dynamics the $\mathcal{PT}$-symmetric quadrimer has an interesting difference from the dimer and trimer. In particular, the four linear eigenvalues of the system are

$$\lambda_{1,2} = \pm\sqrt{-\gamma^2 + \frac{k}{2}\left(3k - \sqrt{-16\gamma^2 + 5k^2}\right)} \tag{2.38}$$

$$\lambda_{3,4} = \pm\sqrt{-\gamma^2 + \frac{k}{2}\left(3k + \sqrt{-16\gamma^2 + 5k^2}\right)}. \tag{2.39}$$

The fundamental difference of this case from the dimer and regular trimer considered above is that these eigenvalues do not become imaginary by crossing through zero. Instead, they become *genuinely complex* through their collision that occurs for $\gamma_{PT} = \sqrt{5}k/4$, a critical

point which is lower than that of the trimer. This could be an experimentally observable signature of the difference of the near linear dynamics of the quadrimer.
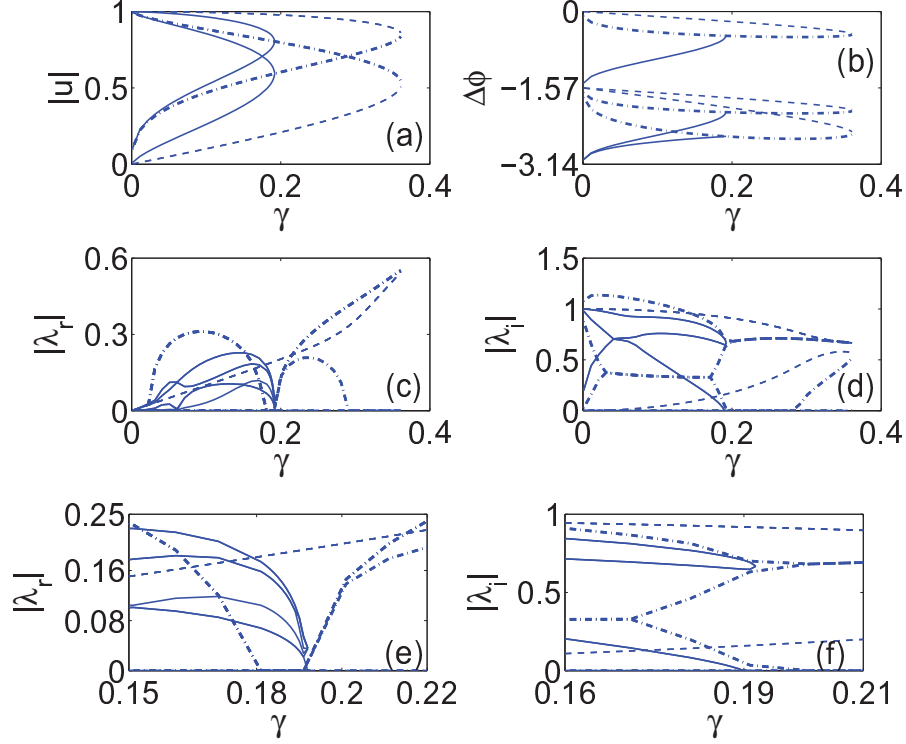


**Figure 2.11.** (Color online) Three branches of solutions for the quadrimer problem with parameters $E = 1$ and $\phi_a$ normalized to $0$: the solid lines denote the asymmetric branch the blue circles branch, while the dashed and dash-dotted lines denote the symmetric branches the red diamonds branch and the black crosses branch, respectively. For each branch, four curves in (a) stand for $A, B, C, D$ (only two curves for the red diamonds branch and the black crosses branch since $A = D, B = C$ in these cases), and three curves in (b) stand for $\phi_b, \phi_c, \phi_d$. Panel (e) and (f) are zooms of (c) and (d) respectively.

The dynamics of these different branches was also considered in Fig. 2.12. In this case, it can be clearly observed that all three branches tend toward an asymmetric distribution of the power. This favors the two sites (third and fourth) with the gain, although some case examples can be found [see, e.g., Fig. 2.12(a) for the asymmetric branch] where only one of the two gain sites is favored by the mass evolution.
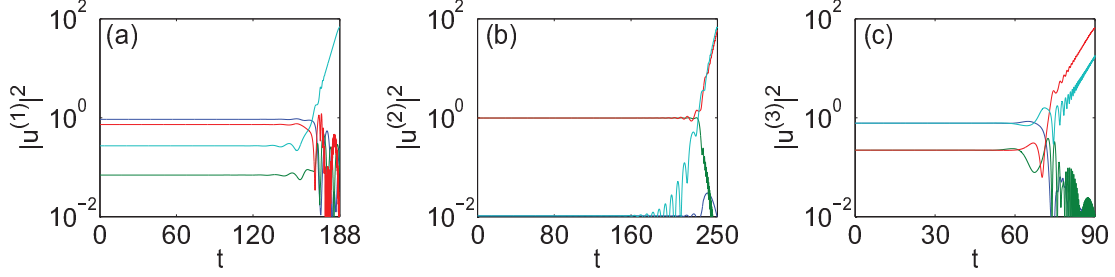
**Figure 2.12.** (Color online) The profile of the dynamical evolution of the three different branches: (a) the blue circles branch, (b) the red diamonds branch, and (c) the black crosses branch of a quadrimer in the case of $E = 1$ and $\gamma = 0.1$.

# IV  $\mathcal{PT}$-symmetric coupler with $\chi^2$ nonlinearity

Recently the studies of solitons in quadratically nonlinear media were extended to $\mathcal{PT}$-symmetric systems. More specifically, the existence and stability of solitons for localized potentials in quadratic media was explored in [32]. In the work of [33], the effect of periodic $\mathcal{PT}$-symmetric potentials on $\chi^{(2)}$ solitons was described.

It is on that direction of exploring the interplay of quadratic nonlinearity and $\mathcal{PT}$-symmetric potentials that the present work is focused. It is appreciated that even in the case of two waveguides, this combination offers a significant level of complexity, as well as a number of features that are absent in the cubic Kerr nonlinearity case.

The prototypical setup of equations describing the $\mathcal{PT}$ symmetric coupler with quadratic nonlinearity reads as follows:

$$i\dot{u}_1 = k_1 u_2 - 2u_1^* v_1 + i\gamma_1 u_1, \qquad (2.40a)$$

$$i\dot{v}_1 = k_2 v_2 - u_1^2 - q v_1 + i\gamma_2 v_1, \qquad (2.40b)$$

$$i\dot{u}_2 = k_1 u_1 - 2u_2^* v_2 - i\gamma_1 u_2, \qquad (2.40c)$$

$$i\dot{v}_2 = k_2 v_1 - u_2^2 - q v_2 - i\gamma_2 v_2. \qquad (2.40d)$$

Each waveguide contains two harmonics: the fundamental field (first harmonic) $u_j$ and the second harmonic $v_j$, $j = 1, 2$, which are nonlinearly coupled. The linear coupling between

the first harmonics is characterized by the parameter $k_1$, while that of the second harmonics by $k_2$. Both $k_1$ and $k_2$ will be considered positive. The gain (loss) strength in the two arms of the dimer is given by the parameters $\gamma_j > 0$ ($\gamma_j < 0$), for the first ($j = 1$) and second ($j = 2$) harmonics, respectively. In what follows, we will explore different parameter values of $(\gamma_1, \gamma_2)$ to get a systematic sense of the model phenomenology. The overdot in (2.40) denotes the derivative with respect to the evolution variable which, here, we will denote as $t$ (although in the optical realm it represents the propagation distance $z$).

In particular, we focus on nonlinear solutions preserving the symmetry pertinent to the linear part, i.e. to the $\mathcal{PT}$-invariant modes obeying $\mathcal{PT}\mathbf{w} = \mathbf{w}$. Using for such modes the amplitude-phase decomposition we rewrite the stationary solution $\mathbf{w}$ in the form

$$\mathbf{w} = \begin{pmatrix} Ae^{i\phi_1} \\ Be^{i\phi_2} \\ Ae^{-i\phi_1} \\ Be^{-i\phi_2} \end{pmatrix}, \tag{2.41}$$

where $A$ and $B$ are real stationary amplitudes and $\phi_{1,2}$ are stationary phases. This ansatz reduces (2.40) to the system of stationary equations as follows

$$E = k_1 e^{-2i\phi_1} - 2Be^{i(\phi_2 - 2\phi_1)} + i\gamma_1, \tag{2.42a}$$

$$2E = k_2 e^{2i\phi_2} - (A^2/B)e^{i(\phi_2 - 2\phi_1)} - q - i\gamma_2 \tag{2.42b}$$

(where it is assumed that $B \neq 0$). Further splitting to real and imaginary parts yields four equations:

$$E = k_1 \cos(2\phi_1) - 2B \cos(\phi_2 - 2\phi_1), \tag{2.43a}$$

$$0 = -k_1 \sin(2\phi_1) - 2B \sin(\phi_2 - 2\phi_1) + \gamma_1, \tag{2.43b}$$

$$2E = k_2 \cos(2\phi_2) - (A^2/B) \cos(\phi_2 - 2\phi_1) - q, \tag{2.43c}$$

$$0 = k_2 \sin(2\phi_2) - (A^2/B) \sin(\phi_2 - 2\phi_1) - \gamma_2. \tag{2.43d}$$

26
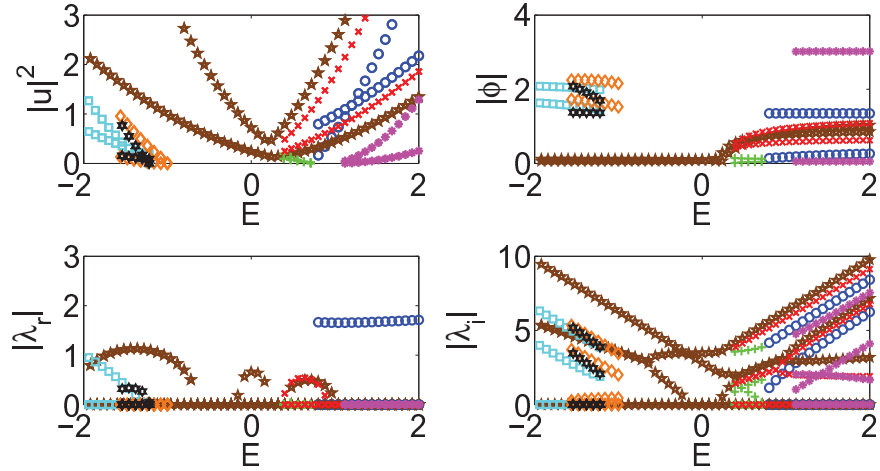
**Figure 2.13.** (Color online) Existence and stability properties of nonlinear modes with $k_1 = 1$, $k_2 = 2$, $q = 0.5$, $\gamma_1 = 0.1$, $\gamma_2 = 0.5$. The four panels denote the solution amplitude (top left), phase differences between adjacent nodes (top right), real and imaginary parts (second row) of eigenvalues. For a detailed explanation of the different families, see the text.

If we take $A$, $B$, $\phi_{1,2}$ as four unknowns in the system (2.43), then one can expect that there exists one or several solutions for any given $E$. Therefore, we can speak about *continuous families* of nonlinear modes.

We now turn to a more systematic analysis of the existence and stability properties of the different families of solutions identified previously, for reasons of completeness. Fig. 2.13 illustrates the situation where $k_1 = 1$, $k_2 = 2$, $q = 0.5$, $\gamma_1 = 0.1$, $\gamma_2 = 0.5$. There are eight families of solutions in this case, denoted by different symbols. Their eigenvalues for the respective parameters of existence are shown in the case of three different choices of $E$ in Fig. 2.14.

- The family denoted by blue circles arises from $E = \tilde{E}_3 \approx 0.72$ and continues monotonically increasing its sum of squared amplitudes upon increase of $E$ to infinity. It always has two pairs of purely imaginary and one pair of real eigenvalues, which give rise to its instability.
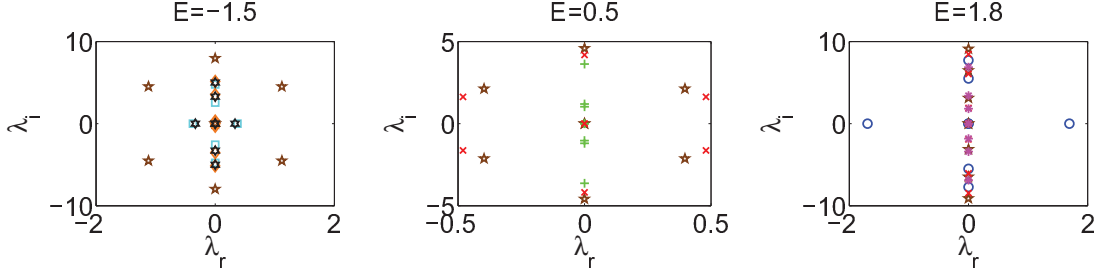
**Figure 2.14.** (Color online) Eigenvalues of the linearization problem of nonlinear modes with $k_1 = 1$, $k_2 = 2$, $q = 0.5$, $\gamma_1 = 0.1$, $\gamma_2 = 0.5$. The same notation has been used as in Fig. 2.13.

- The brown pentagram family exists for all the considered values of $E$. The amplitudes of both harmonics reach their minimum (within the parabolic shape of the family reported previously) in the interval $E \in [0.2, 0.3]$, but at different points. This family has three pairs of purely imaginary eigenvalues, two of which collide at $E \approx -2.13$ and turn into a complex quartet. At $E \approx -0.65$, the complex quartet collides on the imaginary axis and splits anew into two pairs of imaginary eigenvalues, restabilizing the waveform. The larger of the two imaginary pairs subsequently meets the largest imaginary eigenvalues and the collision yields a complex quartet within the short parametric interval of $E \in [-0.20, -0.19]$ (hereafter boundaries of the intervals are given approximately). The remaining (lowest frequency) pair collides with the spectral plane origin and turns into a real pair at $E \approx -0.2$. This pair of eigenvalues becomes imaginary again shortly at $E \approx 0.2$ and collides with its former partner at $E \approx 0.41$ to form a complex quartet. This complex quartet once again splits into two purely imaginary pairs at $E \approx 1$. As a result, the brown pentagrams family is stable for all $E$ except on $[-2.13, -0.65], [-0.2, 0.2], [0.41, 1]$. From the above, the substantial complexity of the family stability properties should be rather evident.

- The green pluses and the red crosses arise together from a saddle-node bifurcation at $E \approx 0.3$. The green pluses family is essentially stable except when $E$ is within

a small interval of $[0.47, 0.48]$, where two out of three pairs of purely imaginary eigenvalues collide yielding a Hamiltonian-Hopf bifurcation and a complex quartet and the reverse path renders the eigenvalues purely imaginary again. This family terminates at $E = \tilde{E}_3 \approx 0.72$ with the first harmonic amplitude vanishing.

- The red crosses family bifurcates from the same point as the green pluses, however it does not terminate. It is unstable only on an interval of $E \in [0.39, 0.89]$ due to a complex quartet.

- The magenta stars family arises from the linear limit at $E = \tilde{E}_1 \approx 0.99$ and exists always thereafter. It has three pairs of purely imaginary eigenvalues, too. Two of them turn into a complex quartet within the small interval $[1.38, 1.43]$ and make the family unstable in this interval.

- The cyan squares family comes from $-\infty$ having a real pair and two purely imaginary pairs of eigenvalues. This branch is stable only after $E \approx -1.3$ where the real pair turns purely imaginary; subsequently the branch terminates at $E = \tilde{E}_4 \approx -1.22$ (with the first harmonic amplitude vanishing).

- The orange diamonds and the black hexagrams emerge from a saddle-node bifurcation at $E \approx -1.63$. The orange diamonds constitute the only family that is always stable, having three pairs of purely imaginary eigenvalues. This family terminates at the linear limit of $E = \tilde{E}_2 \approx -0.99$.

- The black hexagrams start at the same point as the orange diamonds but terminate at $E = \tilde{E}_4 \approx -1.22$. It always has two pairs of purely imaginary and one pair of real eigenvalues. Hence it is generically unstable.

As general comments we can infer that, arguably, the most robust families and ones that will generically exist are the ones emerging from the eigenvalues $\tilde{E}_{1,2}$ of the linear limit. The other families may have intervals of stability but also often suffer oscillatory or real
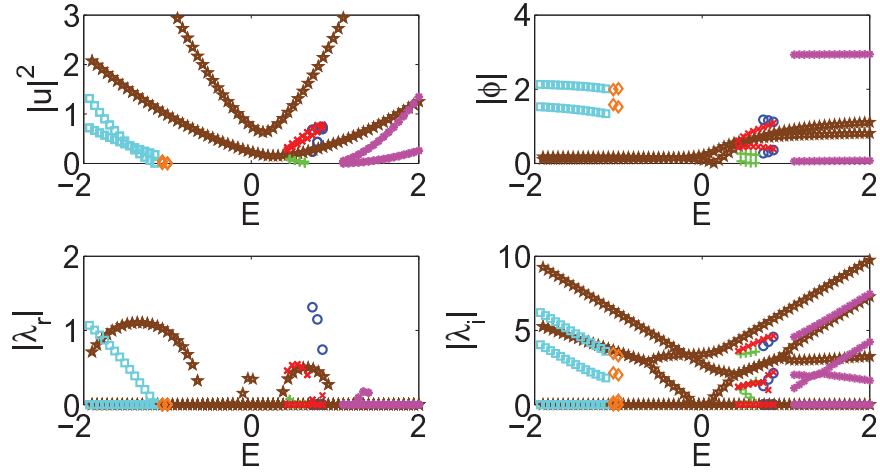
**Figure 2.15.** (Color online) Existence and stability properties of nonlinear modes with similar settings as in Fig. 2.13 but for $k_1 = 1$, $k_2 = 2$, $q = 0.5$, $\gamma_1 = 0.1$, $\gamma_2 = 0.9$.
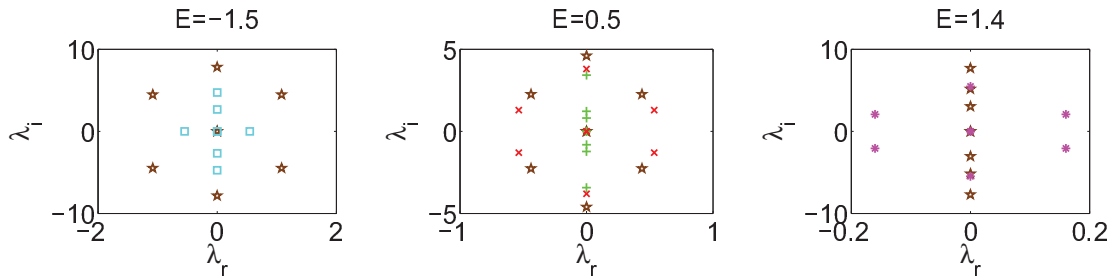


**Figure 2.16.** (Color online) Eigenvalues of the linearization problem of nonlinear modes with $k_1 = 1$, $k_2 = 2$, $q = 0.5$, $\gamma_1 = 0.1$, $\gamma_2 = 0.9$.

instabilities and are subject to saddle-center bifurcations (although e.g., the family starting from $\tilde{E}_1 \approx 0.99$ also has a small interval of instability, and the generically stable family starting from $\tilde{E}_2 \approx -0.99$ is subject to a saddle-node bifurcation).

Fig. 2.15 and Fig. 2.16 show us the solution profiles and their eigenvalues under the parameter $k_1 = 1$, $k_2 = 2$, $q = 0.5$, $\gamma_1 = 0.1$, $\gamma_2 = 0.9$. In this case there are seven families. The black hexagrams family of Fig. 2.13 does not exist any more. We briefly summarize the difference in each family in the following compared with the previous ones.

- The red crosses family now arises from a saddle-node bifurcation with the green pluses at $E \approx 0.36$ and terminates into another saddle-node bifurcation with the blue

30

circles families at $E \approx 0.85$. It now has a pair of purely imaginary and a complex quartet eigenvalues. The latter one reshapes into two pairs of purely imaginary eigenvalues at $E \approx 0.74$, and one of them becomes real at $E \approx 0.84$. Hence, it is unstable except on the interval $[0.74, 0.84]$.

- The blue circle branch is still unstable but now exists from $E = \tilde{E}_3 \approx 0.64$ to $E \approx 0.85$.

- The green pluses branch now exists from $E \approx 0.36$ to $\tilde{E}_3 \approx 0.64$. It is essentially stable except when $E$ is between $[0.4, 0.46]$.

- The brown pentagrams still exist for all $E$ and bear similar eigenvalues as in Fig. 2.13. In this case, the branch is stable except on $[-2.06, -0.61], [-0.22, -0.17],$ $[-0.1, 0.07], [0.37, 0.97]$.

- The magenta stars family is similar as in Fig. 2.13, again bifurcating from the linear limit and now being stable in the exception of the interval $E \in [1.27, 1.45]$.

- The unstable cyan squares family still comes from $-\infty$, but now it is always unstable and terminates at $\tilde{E}_4 = -1.14$.

- The orange diamonds family exists from $\tilde{E}_4 \approx -1.14$ to $\tilde{E}_2 \approx -0.99$. It is unstable until $E \approx -1.1$ and becomes stable thereafter.

For comparison purposes, we also consider the Hamiltonian case $k_1 = 1$, $k_2 = 2$, $q = 0.5$, $\gamma_1 = 0$, $\gamma_2 = 0$. Fig. 2.17 and Fig. 2.18 show the six families of nonlinear modes in this case.

- The blue circle family is similar to the one in Fig. 2.13, i.e. arises from $E = \tilde{E}_3 = 0.75$ and is always unstable. It possesses a pair of real and two pairs of purely imaginary eigenvalues for all $E$ where it exists.
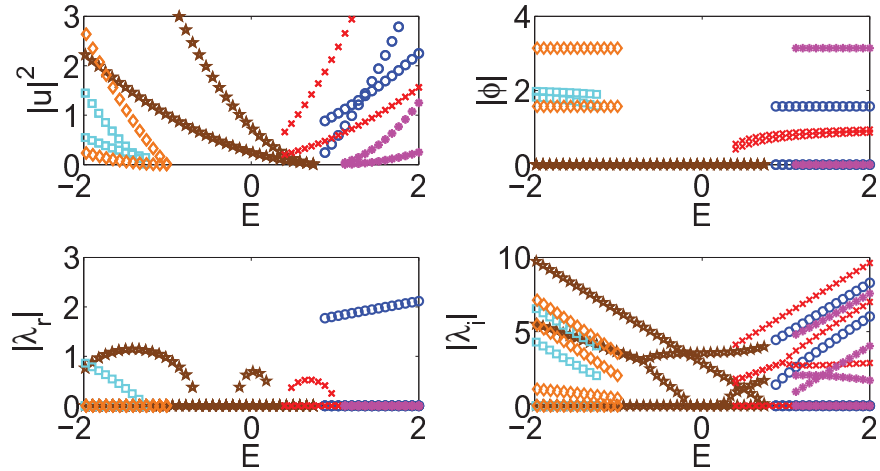
**Figure 2.17.** (Color online) Existence and stability properties of nonlinear modes with similar settings as Fig. 2.13 but for $k_1 = 1$, $k_2 = 2$, $q = 0.5$, $\gamma_1 = 0$, $\gamma_2 = 0$.
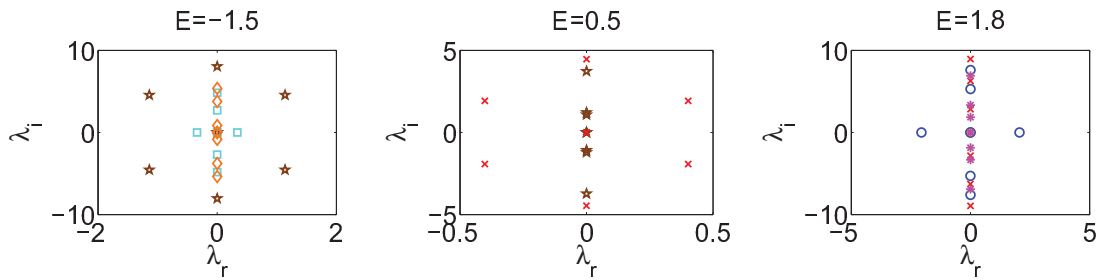


**Figure 2.18.** (Color online) Eigenvalues of the linearization problem of nonlinear modes with $k_1 = 1$, $k_2 = 2$, $q = 0.5$, $\gamma_1 = 0$, $\gamma_2 = 0$.

- The brown pentagrams now exist only up to $\tilde{E}_3 = 0.75$. This branch is stable except on $[-2.17, -0.66], [-0.17, 0.24]$, where it has a complex quartet of eigenvalues.

- The red crosses now bifurcate from the brown pentagrams at $E \approx 0.25$ and persist beyond the point. It is this bifurcation that apparently splits into two fold points in the two cases considered previously. The red crosses are unstable only on the interval $[0.41, 1]$, where a complex quartet of eigenvalues comes from two pairs of purely imaginary ones colliding at $E \approx 0.41$ and returning to the imaginary axis at $E \approx 1$.

- The magenta stars family still arises from the linear limit at $\tilde{E}_1 = 1$. However, it now always has three pairs of purely imaginary eigenvalues and hence is stable wherever it exists.

- The cyan squares family is similar to the one in Fig. 2.13, too. It is unstable, comes from $-\infty$, and terminates at $\tilde{E}_4 = -1.25$.

- The orange diamonds branch now also exists from $-\infty$ and terminates at $\tilde{E}_2 = -1$. It is always stable in this case, too, again verifying the robustness of the families that emerge from the linear limit.

Finally, from the point of view of numerical results, we have also performed direct numerical simulations of the propagation dynamics of the quadratically nonlinear $\mathcal{PT}$-symmetric dimer. These simulations allow us to obtain a feeling about the dynamical implications of the instabilities presented above.

In Fig. 2.19, we show the dynamics of the nonlinear modes with $k_1 = 1$, $k_2 = 2$, $q = 0.5$, $\gamma_1 = 0.1$, $\gamma_2 = 0.5$, which corresponds to Fig. 2.13. We choose different values of $E$ for the different families, usually in order to simulate their typical unstable behavior under a small perturbation by numerical errors up to $10^{-7}$ [however, as an exception for the orange diamonds e.g. of panel (g), we only confirm their generic stability]. In panel (a),(b) and (d), we pick $E = 1.5$ for the blue circles family, $E = 0.5$ for the brown
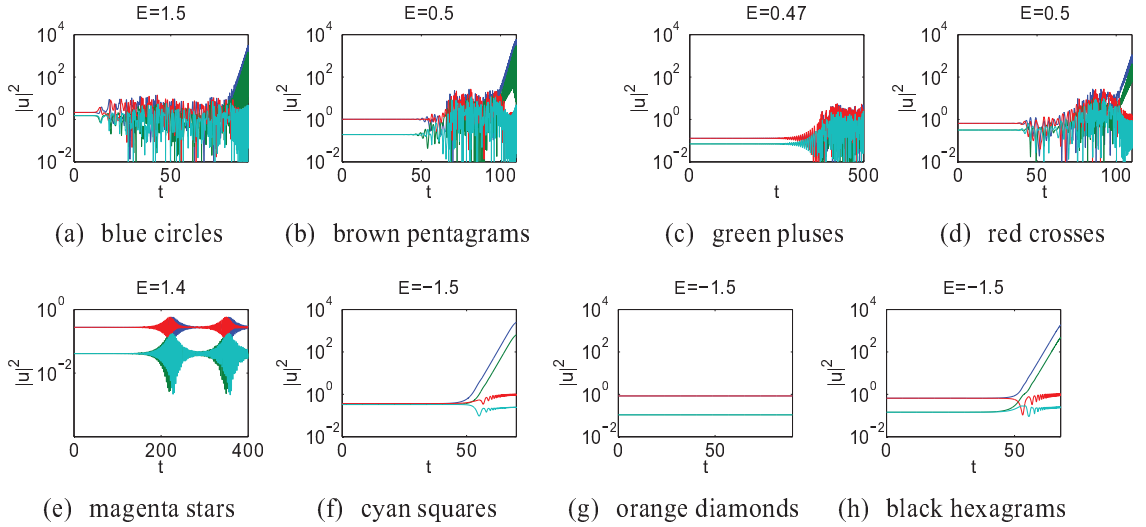
**Figure 2.19.** (Color online) Dynamical plots in a semilogarithmic scale for the $y$-variable (denoting the amplitudes of the fundamental and the second harmonic) for different non-linear modes with $k_1 = 1$, $k_2 = 2$, $q = 0.5$, $\gamma_1 = 0.1$, $\gamma_2 = 0.5$. The family considered and the value of the propagation constant are depicted explicitly in each panel.

pentagrams family and the red crosses family, where all of them are unstable. In all three cases here, the amplitudes of the first waveguide (which features gain) grow exponentially fast after some oscillation. The amplitudes of the second waveguide (which sustains loss) keep oscillating but also appear to increase in comparison to their initial values. In panel (c), all the amplitudes of the green pluses family are relatively constant for a long evolution interval and oscillating around their initial values, due to its complex quartet of eigenvalues at $E = 0.47$. Panel (e) shows the amplitudes of the two waveguides of the magenta star family which are oscillating quasi-periodically in a similar way at $E = 1.4$. Panel (f) and (h) illustrate the instability of cyan squares and black hexagrams where the amplitudes of both harmonics of the first waveguide grow exponentially at about $t = 50$ while the amplitudes of the second waveguide do not appear to grow indefinitely (but contrary to the cubic case, they are also not observed to systematically decay [34]). The stable dynamics of the orange diamonds family at $E = -1.5$ is also plotted in panel (g). Generally, for the

|  |  |  |  |
|---|---|---|---|
| (a) blue circles | (b) brown pentagrams | (c) green pluses | (d) red crosses |



|  |  |  |
|---|---|---|
| (e) magenta stars | (f) cyan squares | (g) orange diamonds |
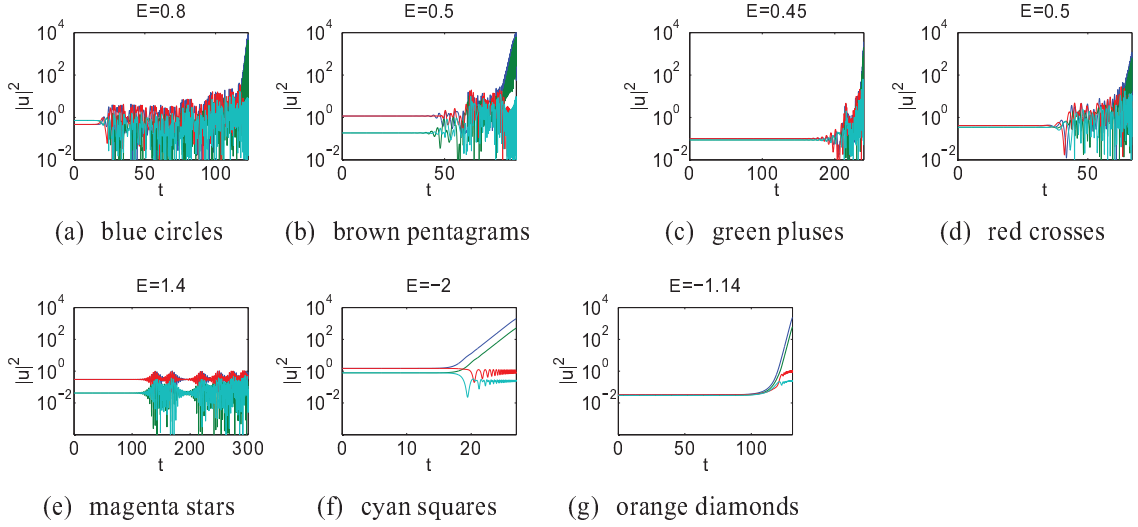
**Figure 2.20.** (Color online) Dynamical plots in a semi-logarithmic scale for the $y$-variable (denoting the amplitudes of the fundamental and the second harmonic) for different non-linear modes with $k_1 = 1$, $k_2 = 2$, $q = 0.5$, $\gamma_1 = 0.1$, $\gamma_2 = 0.9$.

unstable families, we infer either a growth in the first waveguide coupled with a bounded oscillation in the second waveguide, or a bounded evolution in both waveguides.

Fig. 2.20 shows similar dynamic plots corresponding to the families plotted in Fig. 2.15. Here all of the blue circles, brown pentagrams, green pluses, and red crosses in panel (a)–(d) are unstable and present similar features as before, with unbounded growth in the one waveguide (but no decay of amplitude on the second). The amplitudes of the magenta stars still oscillate quasi-periodically around their initial values. In panels (f) and (g), both amplitudes of the first waveguide grow exponentially. The amplitudes of the second waveguide in cyan squares decay a little and then feature a weak oscillation around their initial values, whereas for the orange diamonds family they grow a little and then feature a similar weak oscillation.

Fig. 2.21 shows the dynamics of the Hamiltonian case under the parameters $k_1 = 1$, $k_2 = 2$, $q = 0.5$, $\gamma_1 = 0$, $\gamma_2 = 0$ that corresponds to Fig. 2.17. Since $\gamma_1 = 0$, $\gamma_2 = 0$, neither of the two waveguides has a gain or loss profile. Shown in panels (a)–(c), are all the amplitudes of the harmonics of the the blue circle, brown pentagram, and red cross
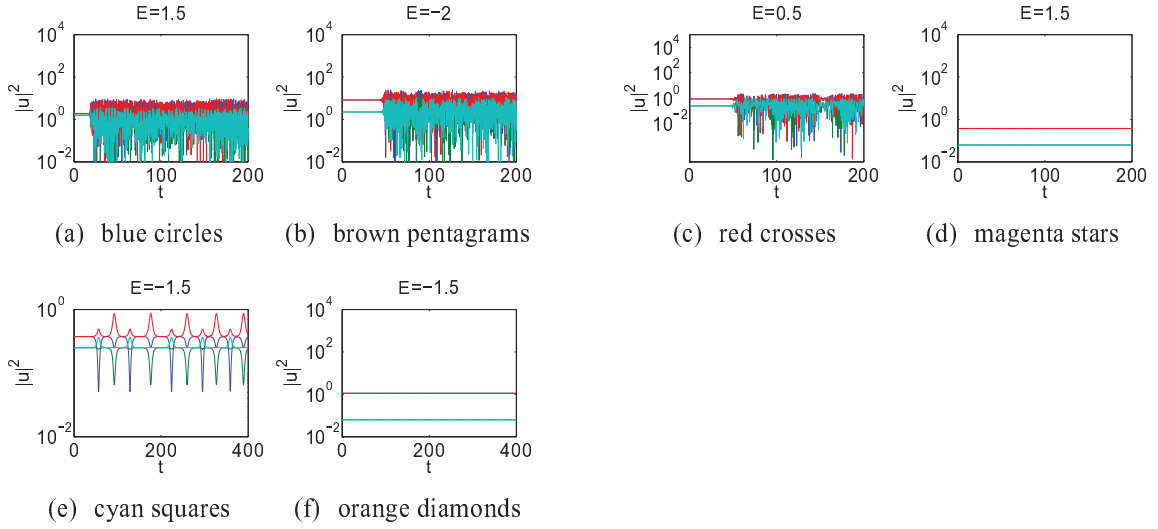
**Figure 2.21.** (Color online) Dynamical semi-logarithmic plots of nonlinear modes with $k_1 = 1$, $k_2 = 2$, $q = 0.5$, $\gamma_1 = 0$, $\gamma_2 = 0$.

families which are oscillating around their initial values, with no trend of indefinite growth or decay, just as expected by the absence of $\mathcal{PT}$-symmetric terms. In panel (e), the cyan squares family amplitudes now weakly oscillate periodically. Panels (d) and (f) show the stable dynamics of the magenta stars and the orange diamonds families in this case, i.e., confirming the dynamical robustness of the families stemming from the linear limit.

# CHAPTER 3

# ONE DIMENSIONAL NONLINEAR $\mathcal{PT}$-SYMMETRIC OLIGOMERS

In what follows below, we study the case of nonlinear-$\mathcal{PT}$-symmetric dimers [23] and trimers, in which a gain/loss pattern appears *both* in the linear and nonlinear terms. One of the fundamental side-effects of the fact that the nonlinearity does *not* commute with the $\mathcal{PT}$ operator is the existence of nonlinear solutions that persist past the linear $\mathcal{PT}$-phase-transition threshold. Furthermore, one of the principal consequences of the presence of gain/loss terms in the nonlinearity is the existence of both symmetric and asymmetric (in their amplitude) stationary solutions, with the latter possessing a non-symmetric linearization spectrum. Interesting bifurcation phenomena (such as spontaneous symmetry breakings) are, additionally, found to arise in this case.

# I  Analysis of Stationary Solutions for the Nonlinear-$\mathcal{PT}$-Symmetric Dimer Case

The dynamical equations of a nonlinear $\mathcal{PT}$-symmetric dimer have the form:

$$iu_t = -\epsilon v + (\rho_r - i\rho_{im})|u|^2 u + i\gamma u \qquad (3.1)$$

$$iv_t = -\epsilon u + (\rho_r + i\rho_{im})|v|^2 v - i\gamma v. \qquad (3.2)$$

The model contains the Kerr nonlinearity which is relevant to optical waveguides and is effectively a generalization of the experimental framework of [5], in that nonlinear (i.e., amplitude-dependent) gain and loss processes are taken into account. Similarly as the

linear cases, considering the prototypical stationary solutions of the system, we let $u(t)$ and $v(t)$ have the forms:

$$u(t) = ae^{iEt}, \qquad v(t) = be^{iEt} \tag{3.3}$$

where $E$ is the propagation constant while the complex numbers $a$ and $b$ denote the amplitudes of the dimer sites. Plugging this ansatz into Eq. (3.1), one finds the complex nonlinear algebraic equations:

$$Ea = \epsilon b - (\rho_r - i\rho_{im})|a|^2 a - i\gamma a \tag{3.4}$$

$$Eb = \epsilon a - (\rho_r + i\rho_{im})|b|^2 b + i\gamma b. \tag{3.5}$$

We now use a polar decomposition of $a$ and $b$ of the form:

$$a = Ae^{i\phi_a}, \qquad b = Be^{i\phi_b} \tag{3.6}$$

for real-valued $A$, $B$, $\phi_a$ and $\phi_b$. Plugging Eq. (3.6) into Eq. (3.4) and writing these equations in terms of their real and imaginary parts, we find:

$$EA = \epsilon B \cos(\phi_b - \phi_a) - \rho_r A^3 \tag{3.7}$$

$$EB = \epsilon A \cos(\phi_b - \phi_a) - \rho_r B^3 \tag{3.8}$$

$$-\epsilon A \sin(\phi_b - \phi_a) - \rho_{im} B^3 + \gamma B = 0 \tag{3.9}$$

$$\epsilon B \sin(\phi_b - \phi_a) + \rho_{im} A^3 - \gamma A = 0. $$

The last two equations yield

$$(A^2 - B^2) \left[ \rho_{im}(A^2 + B^2) - \gamma \right] = 0. \tag{3.10}$$

38

We note that Eq. (3.10) yields a simple algebraic condition which connects the amplitude of the two dimer sites. This allows us to distinguish several subcases of interest. We look for nontrivial solutions $A$ and $B$ in each of the subcases presented in the following subsection.

## I.1 Existence of localized modes for the dimer case

Eq. (3.10) identifies the different scenarios for the values of $A$ and $B$. We now examine the three cases that arise from this equation for our dimer dynamical system.

- Case I : $A^2 = B^2$ and $A^2 + B^2 \neq \gamma/\rho_{im}$:

Recall the equations given in (3.7):

$$EA = \epsilon B \cos(\phi_b - \phi_a) - \rho_r A^3; \tag{3.11}$$

$$EB = \epsilon A \cos(\phi_b - \phi_a) - \rho_r B^3 \tag{3.12}$$

and

$$\epsilon B \sin(\phi_b - \phi_a) + \rho_{im} A^3 - \gamma A = 0; \tag{3.13}$$

$$-\epsilon A \sin(\phi_b - \phi_a) - \rho_{im} B^3 + \gamma B = 0. \tag{3.14}$$

Since $A = B$ (i.e., these are symmetric solutions) in this case, the two equations in each set are equivalent. Thus, we have:

$$\sin(\phi_b - \phi_a) = \frac{-(\rho_{im} A^2 - \gamma)}{\epsilon}, \tag{3.15}$$

$$\cos(\phi_b - \phi_a) = \frac{\rho_r A^2 + E}{\epsilon}. \tag{3.16}$$

We use the relation $\sin^2(\phi_b - \phi_a) + \cos^2(\phi_b - \phi_a) = 1$ to determine the following quadratic equation for $A^2$:

$$(\rho_r^2 + \rho_{im}^2)A^4 + 2(E\rho_r - \gamma\rho_{im})A^2 + \gamma^2 + E^2 - \epsilon^2 = 0. \tag{3.17}$$

The solution of the resulting bi-quadratic equation reads:

$$A^2 = B^2 = \frac{-(E\rho_r - \gamma\rho_{im}) \pm \sqrt{(E\rho_r - \gamma\rho_{im})^2 - (\rho_r^2 + \rho_{im}^2)(\gamma^2 + E^2 - \epsilon^2)}}{\rho_r^2 + \rho_{im}^2} \quad (3.18)$$

with the restriction that

$$(E\rho_r - \gamma\rho_{im})^2 \geq (\rho_r^2 + \rho_{im}^2)(\gamma^2 + E^2 - \epsilon^2). \quad (3.19)$$

- Case II :  $A^2 + B^2 = \gamma/\rho_{im}$  and  $A^2 \neq B^2$:

Under these conditions, one can get

$$A^2 = \frac{\gamma}{2\rho_{im}} \pm \sqrt{\frac{\gamma^2}{4\rho_{im}^2} - \frac{\epsilon^2}{\rho_r^2 + \rho_{im}^2}} \quad (3.20)$$

$$B^2 = \frac{\gamma}{2\rho_{im}} \mp \sqrt{\frac{\gamma^2}{4\rho_{im}^2} - \frac{\epsilon^2}{\rho_r^2 + \rho_{im}^2}} \quad (3.21)$$

$$E = -\frac{\gamma\rho_r}{\rho_{im}} \quad (3.22)$$

$$\cos(\phi_b - \phi_a) = -\frac{\epsilon\rho_r}{\sqrt{\rho_r^2 + \rho_{im}^2}}, \quad (3.23)$$

with the restriction that

$$\frac{\gamma^2}{4\rho_{im}^2} \geq \frac{\epsilon^2}{\rho_r^2 + \rho_{im}^2}. \quad (3.24)$$

A fundamental difference of this case from case I is that here $E$ is no longer a free parameter [23]. The solutions with the different amplitudes will be called asymmetric in what follows.

- Case III :  $A^2 + B^2 = \gamma/\rho_{im}$  and  $A^2 = B^2$:

As a final "mixed" possibility, between the above symmetric and asymmetric cases, from Eq. (3.7), it is straightforward to obtain

$$A \;\; = \;\; B = \sqrt{\frac{\gamma}{2\rho_{im}}}, \tag{3.25}$$

$$\cos(\phi_b - \phi_a) \;\; = \;\; \frac{2\rho_{im}E + \gamma\rho_r}{2\epsilon\rho_{im}} \tag{3.26}$$

$$\sin(\phi_b - \phi_a) \;\; = \;\; \frac{\gamma}{2\epsilon}, \tag{3.27}$$

with the restriction that

$$\left(\frac{2\rho_{im}E + \gamma\rho_r}{2\epsilon\rho_{im}}\right)^2 + \left(\frac{\gamma}{2\epsilon}\right)^2 = 1. \tag{3.28}$$

Once again this implies that once other parameters (such as $\gamma$, $\rho_{im}$, $\rho_r$ and $\epsilon$) are determined, $E$ is not a free parameter; rather is obtained from Eq. (3.28). These will be referred to as special symmetric solutions in the following.

It is particularly important to highlight that both solutions of Case II (asymmetric) and ones of Case III (special symmetric) are present due to competing effects of the linear and nonlinear gain loss profiles; notice the opposite signs thereof in Eq. (3.1) and the necessity of $\gamma\rho_{im} > 0$ for such solutions to exist. In the case, where the linear and nonlinear gain/loss cooperate (rather than compete) such solutions would obviously be absent and the system would be inherently less wealthy in its potential dynamics. This point was also discussed in [23].

41

## I.2 Linear stability analysis for the dimer case

We now go back to our original $\mathcal{PT}$-symmetric dimer with linear and nonlinear gain and loss in Eq. (3.1) and examine the linear stability of the solutions to this equation. We begin by setting

$$u(t) = e^{iEt}[a + pe^{\lambda t} + Pe^{\lambda^* t}],$$
(3.29)

$$v(t) = e^{iEt}[b + qe^{\lambda t} + Qe^{\lambda^* t}]$$
(3.30)

where $\lambda$ is a complex-valued eigenvalue parameter revealing the growth (instability) or oscillation (stability) of all the modes of linearization of the dimer system; $*$ denotes the complex conjugate and $p, P, q, Q$ are perturbations to the solutions of interest. Plugging Eq. (3.29) into Eq. (3.1) and taking only the linear terms in $p, P, q$ and $Q$, we find the following eigenvalue problem:

$$\mathbf{A}\mathbf{X} = i\lambda\mathbf{X}$$
(3.31)

where $\mathbf{X} = (p, \ -P^*, \ q, \ -Q^*)^T$ and $\mathbf{A}$ is written as:

$$
\mathbf{A} =
\begin{pmatrix}
a_{11} & -a^2(\rho_r - i\rho_{im}) & -\epsilon & 0 \\
(a^*)^2(\rho_r + i\rho_{im}) & a_{22} & 0 & \epsilon \\
-\epsilon & 0 & a_{33} & -b^2(\rho_r + i\rho_{im}) \\
0 & \epsilon & (b^*)^2(\rho_r - i\rho_{im}) & a_{44}
\end{pmatrix}
$$
(3.32)

where

$$a_{11} = E + 2|a|^2(\rho_r - i\rho_{im}) + i\gamma$$

$$a_{22} = -2|a|^2(\rho_r + i\rho_{im}) - E + i\gamma$$

$$a_{33} = E - i\gamma + 2|b|^2(\rho_r + i\rho_{im})$$

$$a_{44} = -E - i\gamma - 2|b|^2(\rho_r - i\rho_{im}). \tag{3.33}$$

The use of the symmetric, asymmetric or mixed solutions of the previous subsection into these matrix elements produces a $4 \times 4$ complex matrix whose eigenvalues will determine the spectral stability of the corresponding nonlinear solution. The existence of eigenvalues with positive real part $\lambda_r > 0$ amounts to a dynamical instability of the relevant solution, while in the case where all 4 eigenvalues have $\lambda_r \leq 0$, the solution is linearly stable.

### I.3 Numerical results for the dimer case

Fig. 3.1 shows the profile of the different branches for the dimer case and for parameters $\epsilon = 1$, $E = 1$, $\rho_r = -2$ and $\rho_{im} = 1$ (unless noted otherwise). The branches denoted by blue stars and red diamonds correspond to the case I of symmetric solutions; these two branches collide and disappear at the critical point $\gamma = 1.61$ (when Eq. (3.19) becomes an equality). The green circle and magenta cross branches correspond to case II; and the black squares branch corresponds to case III. For the latter two branches, when $\gamma$ is varied, $E$ is also varied too (rather than staying fixed at $E = 1$ as for case I) according to Eqs. (3.22) and (3.28), respectively. Similar notation is used in Fig. 3.2, which shows the linear stability eigenvalues $\lambda = \lambda_r + i\lambda_i$ of the linearization. While the branches of case I are stable, it is interesting to note that the branch of case III (black squares) is stable until a pitchfork (symmetry breaking) bifurcation arises at $\gamma = 0.895$ (when Eq. (3.24) becomes an equality) and acquires a real pair of eigenvalues thereafter signalling its dynamical instability. On the other hand, it is at that critical point that the two branches belonging to case II collide. While the special symmetric black squares' branch of case III persists up to the critical point of $\gamma = 2\epsilon = 2$ of Eq. (3.27), it should be pointed out that nonlinearity enables the

asymmetric branches of Case II to persist for large values of $\gamma$, in fact well past the point of the linear $\mathcal{PT}$ phase transition. This feature has been highlighted in a number of recent works [13, 31]; in the case of the dimer the linear critical $\mathcal{PT}$ phase transition point is identified as $\gamma = \epsilon$, while for the trimer setting considered below it is $\gamma = \sqrt{2}\epsilon$.

An additional point worthy to mention here is that in linear $\mathcal{PT}$-symmetric chains (just as is the case in typical Hamiltonian systems), if $\lambda$ is an eigenvalue to the linearization problem around a solution, so are $-\lambda$, $\bar{\lambda}$, and $-\bar{\lambda}$ (where the overbar denotes complex conjugation here). However, in our nonlinear $\mathcal{PT}$-symmetric dimer $-\lambda$ and $-\bar{\lambda}$ may not appear in the linearization around a particular branch, as is observed in Fig. 3.2. Eigenvalues of the green circles and magenta cross branches are not symmetric about the imaginary axis, but are symmetric with respect to each other. One can see from Fig. 3.3 that the green circles branch is always stable, while the magenta crosses branch is always unstable (due to an oscillatory instability associated with a complex eigenvalue pair). This is because the existence of asymmetry in these solutions of case II creates, in turn, asymmetries in the linearization matrix, due to the nonlinear gain/loss term, which breaks the $\mathcal{PT}$ symmetry of the linearization matrix and produces the corresponding observable asymmetry in eigenvalues.

The dynamical evolution of the different elements of the bifurcation diagram of nonlinear-PT-symmetric dimer is shown in Fig. 3.3 at a fixed $\gamma = 1.5$. In all the cases here and below, where a stationary solution exists for the parameter value for which it is initialized, a numerically exact solution up to $10^{-8}$ is typically used as an initial condition in the system. The system is sufficiently sensitive to dynamical instabilities that even the amplification of roundoff errors is enough to observe them. The stability of the case I branches is evident in the invariance of the relevant states during the course of the simulation (blue stars and red diamonds). On the other hand, the black squares branch is attracted towards the asymmetric (yet stable, as is evident in the corresponding simulation) green circles branch. Finally, the asymmetric magenta crosses branch leads to indefinite growth of the site with the larger

amplitude (nonlinear gain) and the decay of the site with the smaller amplitude (nonlinear loss).
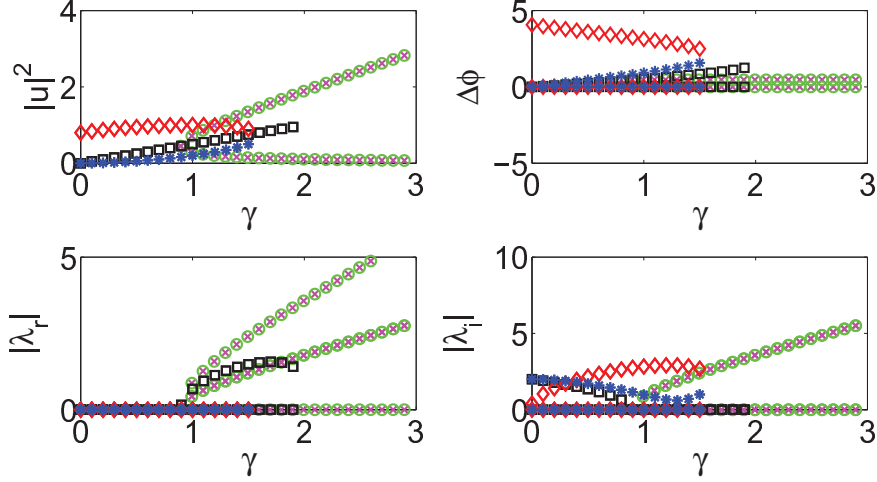


**Figure 3.1.** The solution profiles of the nonlinear $\mathcal{PT}$-symmetric dimer case with $\epsilon = 1$, $\rho_r = -2$ and $\rho_{im} = 1$. The four panels here present the continuation of each branch (the amplitudes in the top left, the phases in the top right, and the real -bottom left- and imaginary -bottom right- parts of the linear stability eigenvalues) starting from the conservative system at $\gamma = 0$. The five branches are denoted by curves of blue stars, red diamonds, black squares, green circles and magenta crosses. Blue stars: Case I with "-" in the amplitude; Red diamonds: Case I with "+" in the amplitude; Green circles: Case II with "+" in the amplitude (of $A$); Magenta crosses: Case II with "-" in the amplitude (of $A$); Black squares: Case III. Notice that the eigenvalues of green circles and magenta crosses are opposite to each other (see the relevant discussion in the text). We always set $E = 1$ in the case I branches, namely the blue stars and the red diamonds, which terminate at the same point when $\gamma = 1.61$. The black squares are subject to a destabilizing supercritical pitchfork bifurcation at $\gamma = 0.895$, $E = 1.789$ whereby the green circles and magenta crosses arise. The black squares branch terminates at $\gamma = 2$; the green circles and magenta crosses exist for arbitrary values of the (linear) gain/loss past the linear $\mathcal{PT}$-symmetry breaking point.

## II    Analysis of Stationary Solutions for the Nonlinear $\mathcal{PT}$-Symmetric Trimer Case

We now consider the generalization of the above considerations to the case of a nonlinear $\mathcal{PT}$-symmetric trimer. Here, the dynamical system associated with a potential application of a three-waveguide setting is of the form:
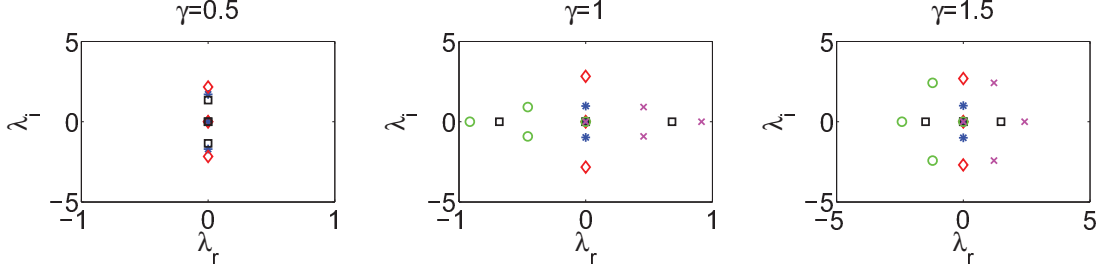
**Figure 3.2.** The eigenvalue plots illustrating the linear stability of the nonlinear-PT-symmetric dimer with $\epsilon = 1$, $\rho_r = -2$ and $\rho_{im} = 1$. For the blue stars and red diamonds branches, we use $E = 1$ here, while for the case II (green circles and magenta crosses) and case III (black squares), $E$ is determined from the remaining parameters based on Eqs. (3.22) and (3.28), respectively.



(a) blue stars branch      (b) red diamonds branch      (c) black squares branch

(d) green circles branch      (e) magenta crosses branch
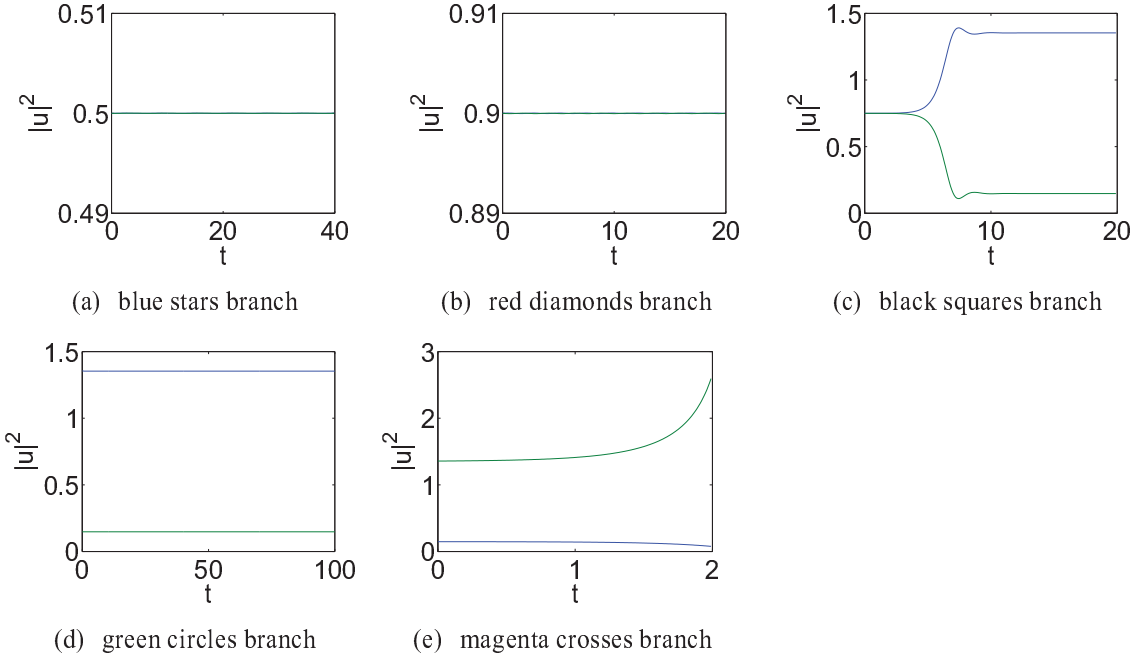
**Figure 3.3.** The dynamical evolution plots of the branches for the case of the nonlinear-PT-symmetric dimer with the same parameter settings as in Fig. 3.2 when $\gamma = 1.5$. The symmetric blue stars and red diamonds of Case I and the asymmetric green circles of Case II are stable, while the black squares of Case III (past the pitchfork point) and magenta crosses of Case II are unstable and deviate from their initial profile during the dynamics (see also the discussion in the text).

$$iu_t = -\epsilon v + (\rho_r - i\rho_{im})|u|^2 u + i\gamma u \tag{3.34}$$

$$iv_t = -\epsilon(u + w) - |v|^2 v \tag{3.35}$$

$$iw_t = -\epsilon v + (\rho_r + i\rho_{im})|w|^2 w - i\gamma w \tag{3.36}$$

46

Such configurations have been considered earlier in optical applications theoretically [35] and even experimentally [29] in the absence of gain/loss. We examine this case with both linear and nonlinear gain/loss profiles. Once again, as in the case of the dimer, we present the richer phenomenology setting of direct competition between linear and nonlinear gain/loss. The middle site is assumed as devoid of gain and loss. The Kerr nonlinearity is also assumed to be present in all three sites. Here, we use $u(t)$, $v(t)$ and $w(t)$ as the complex-valued components for the trimer. For the stationary solutions, we again assume:

$$u(t) = ae^{iEt}, \quad v(t) = be^{iEt} \quad \text{and} \quad w(t) = ce^{iEt}. \tag{3.37}$$

Plugging Eqs. (3.37) into Eq. (3.34), we find:

$$Ea = \epsilon b - (\rho_r - i\rho_{im})|a|^2 a - i\gamma a, \tag{3.38}$$

$$Eb = \epsilon(a + c) + |b|^2 b \tag{3.39}$$

$$Ec = \epsilon b - (\rho_r + i\rho_{im})|c|^2 c + i\gamma c. \tag{3.40}$$

Since $a, b$ and $c$ are complex-valued functions, we use the polar decomposition:

$$a = Ae^{i\phi_a}, \quad b = Be^{i\phi_b} \quad \text{and} \quad c = Ce^{i\phi_c} \tag{3.41}$$

where $A, B, C, \phi_a, \phi_b$ and $\phi_c$ are real-valued. Plugging Eq. (3.41) into Eq. (3.38) and separating the real and imaginary parts, we derive the following set of real-valued equations for $A, B$ and $C$:

$$EA = \epsilon B \cos(\phi_b - \phi_a) - \rho_r A^3, \tag{3.42}$$

$$0 = \epsilon B \sin(\phi_b - \phi_a) + \rho_{im} A^3 - \gamma A, \tag{3.43}$$

$$EB = \epsilon A \cos(\phi_b - \phi_a) + \epsilon C \cos(\phi_b - \phi_c) + B^3, \tag{3.44}$$

$$0 = -\epsilon A \sin(\phi_b - \phi_a) - \epsilon C \sin(\phi_b - \phi_c), \tag{3.45}$$

$$EC = \epsilon B \cos(\phi_b - \phi_c) - \rho_r C^3, \tag{3.46}$$

$$0 = \epsilon B \sin(\phi_b - \phi_c) - \rho_{im} C^3 + \gamma C. \tag{3.47}$$

We seek nontrivial solutions to Eqs. (3.42), i..e, $(A, B, C) \neq (0, 0, 0)$. We can reduce Eqs. (3.42) to the form:

$$\cos(\phi_b - \phi_a) = \frac{EA + \rho_r A^3}{\epsilon B}, \tag{3.48}$$

$$\cos(\phi_b - \phi_c) = \frac{EC + \rho_r C^3}{\epsilon B}, \tag{3.49}$$

$$\sin(\phi_b - \phi_a) = \frac{\gamma A - \rho_{im} A^3}{\epsilon B}, \tag{3.50}$$

$$\sin(\phi_b - \phi_c) = -\frac{(\gamma C - \rho_{im} C^3)}{\epsilon B} \tag{3.51}$$

$$A \cos(\phi_b - \phi_a) + C \cos(\phi_b - \phi_c) = \frac{EB - B^3}{\epsilon}, \tag{3.52}$$

$$A \sin(\phi_b - \phi_a) + C \sin(\phi_b - \phi_c) = 0. \tag{3.53}$$

We apply the first four equations of Eqs. (3.48) into the last two equations and obtain the following relations:

$$B^4 - EB^2 + E(A^2 + C^2) + \rho_r(A^4 + C^4) = 0, \tag{3.54}$$

$$(A^2 - C^2)[\gamma - \rho_{im}(A^2 + C^2)] = 0. \tag{3.55}$$

We now determine $A$, $B$ and $C$ for several subcases (symmetric, asymmetric and mixed) as was done for the dimer case in section II.

## II.1 Existence of localized modes for the trimer case

For the trimer case, the special cases that can be seen to emerge for the solutions of Eqs. (3.54) can be classified as follows:

- Case I : $A^2 = C^2$ and $A^2 + C^2 \neq \gamma/\rho_{im}$:

  In this case the algebraic equations assume the form:

$$\cos(\phi_b - \phi_a) = \frac{EA + \rho_r A^3}{\epsilon B} = \cos(\phi_b - \phi_c) \tag{3.56}$$

$$\sin(\phi_b - \phi_a) = \frac{\gamma A - \rho_{im} A^3}{\epsilon B} = -\sin(\phi_b - \phi_c). \tag{3.57}$$

We now use Eq. (3.54) and $\cos^2(\phi_b - \phi_a) + \sin^2(\phi_b - \phi_a) = 1$ to determine:

$$(\rho_r^2 + \rho_{im}^2)A^6 + 2(E\rho_r - \gamma\rho_{im})A^4 + (E^2 + \gamma^2)A^2 - \epsilon^2 B^2 = 0, \tag{3.58}$$

$$B^4 - EB^2 + 2EA^2 + 2\rho_r A^4 = 0. \tag{3.59}$$

One can solve eqns. (3.58) for $A^2$ and $B^2$ to complete the calculation of the relevant symmetric branch of solutions of Case I.

- Case II : $A^2 + C^2 = \gamma/\rho_{im}$ and $A^2 \neq C^2$:

  From Eq. (3.48), we obtain the four algebraic equations:

$$A^2(E + \rho_r A^2)^2 + A^2(\gamma - \rho_{im} A^2)^2 = \epsilon^2 B^2 \tag{3.60}$$

$$C^2(E + \rho_r C^2)^2 + C^2(\gamma - \rho_{im} C^2)^2 = \epsilon^2 B^2 \tag{3.61}$$

$$B^4 - EB^2 + E\left(A^2 + C^2\right) + \rho_r\left(A^4 + C^4\right) = 0 \tag{3.62}$$

$$A^2 + C^2 = \frac{\gamma}{\rho_{im}}. \tag{3.63}$$

We now have four equations but with only three unknowns ($A$, $B$ and $C$). Therefore, in contrast to the previous symmetric branch of case I, one of the parameters

49

$E$, $\epsilon$, $\rho_r$, $\rho_{im}$, $\gamma$ is determined by the other four; i.e., not all five of these parameters can be picked independently in order to give rise to a solution of the trimer. Once again, we should nevertheless, highlight here that these asymmetric solutions only exist because of the interplay of linear gain/loss and nonlinear loss/gain profiles.

- Case III : $A^2 + C^2 = \gamma/\rho_{im}$ and $A^2 = C^2$:

In this mixed case, we have

$$A^2 = C^2 = \frac{\gamma}{2\rho_{im}} \tag{3.64}$$

$$B^4 - EB^2 + 2EA^2 + 2\rho_r A^4 = 0, \tag{3.65}$$

with the restriction that

$$E^2 - \frac{4E\gamma}{\rho_{im}} - \frac{2\rho_r \gamma^2}{\rho_{im}^2} \geq 0. \tag{3.66}$$

One can solve the following equations for $B$ and $E$

$$B^4 - EB^2 + 2E\frac{\gamma}{2\rho_{im}} + 2\rho_r \frac{\gamma^2}{4\rho_{im}^2} = 0 \tag{3.67}$$

$$\left(\rho_r^2 + \rho_{im}^2\right)\frac{\gamma^3}{8\rho_{im}^3} + (2\rho_r E - 2\rho_{im}\gamma)\frac{\gamma^2}{4\rho_{im}^2} + \left(E^2 + \gamma^2\right)\frac{\gamma}{2\rho_{im}} = \epsilon^2 B^2. \tag{3.68}$$

These equations imply that one of the parameters (e.g., $E$) will be determined once the parameters, $\gamma$, $\epsilon$, $\rho_r$ and $\rho_{im}$ are chosen.

## II.2  Linear stability analysis for the trimer case

We again consider the nonlinear $\mathcal{PT}$-symmetric trimer model with linear and nonlinear gain/loss and examine the linear stability of its solutions given in Eq. (3.34) for the solutions given in the previous section. We begin by positing the linearization ansatz:

$$u(t) = e^{iEt}[a + pe^{\lambda t} + Pe^{\lambda^* t}], \tag{3.69}$$

$$v(t) = e^{iEt}[b + qe^{\lambda t} + Qe^{\lambda^* t}], \tag{3.70}$$

$$w(t) = e^{iEt}[c + re^{\lambda t} + Re^{\lambda^* t}], \tag{3.71}$$

where $p, P, q, Q, r, R$ are perturbations to the solutions of interest. Plugging Eq. (3.69) into Eq. (3.34) and truncating at the linear order in $p, P, q, Q, r$ and $R$, we derive the following eigenvalue problem:

$$\mathbf{A}\mathbf{Y} = i\lambda\mathbf{Y} \tag{3.72}$$

where $\mathbf{Y} = (p, -P^*, q, -Q^*, r, -R^*)^T$ and $\mathbf{A}$ is the $(6 \times 6)$ matrix:

$$\mathbf{A} = \begin{pmatrix} a_{11} & -a^2\Lambda_- & -\epsilon & 0 & 0 & 0 \\ (a^*)^2\Lambda_+ & a_{22} & 0 & \epsilon & 0 & 0 \\ -\epsilon & 0 & E - 2|b|^2 & b^2 & -\epsilon & 0 \\ 0 & \epsilon & -(b^*)^2 & -E + 2|b|^2 & 0 & \epsilon \\ 0 & 0 & -\epsilon & 0 & a_{55} & -c^2\Lambda_+ \\ 0 & 0 & 0 & \epsilon & (c^*)^2\Lambda_- & a_{66} \end{pmatrix} \tag{3.73}$$

where

$$a_{11} = E + i\gamma + 2|a|^2(\rho_r - i\rho_{im}) \tag{3.74}$$

$$a_{22} = -E + i\gamma - 2|a|^2(\rho_r + i\rho_{im}) \tag{3.75}$$

$$a_{55} = E - i\gamma + 2|c|^2(\rho_r + i\rho_{im}), \tag{3.76}$$

$$a_{66} = -E - i\gamma - 2|c|^2(\rho_r - i\rho_{im}), \tag{3.77}$$

$$\Lambda_+ = \rho_r + i\rho_{im}, \tag{3.78}$$

$$\Lambda_- = \rho_r - i\rho_{im}. \tag{3.79}$$

51

The solution of this $6 \times 6$ eigenvalue problem (and whether the corresponding eigenvalues $\lambda$ possess a positive real part) will determine the spectral stability properties of the solutions of the nonlinear-PT-symmetric trimer.

## II.3   Numerical results for the trimer case

- Trimer Case I:

The numerical results for the symmetric solutions of the nonlinear-PT-symmetric trimer (Case I) are shown in Fig. 3.4, Fig. 3.5 and Fig. 3.6, with similar notations as in the dimer case. Solutions are found by numerically solving Eq. (3.58). A typical example of the branches that may arise in case I of the trimer is shown for the parameters $\epsilon = 1$, $E = 1$, $\rho_r = -1$ and $\rho_{im} = 1$. In this case, we find three branches in the considered interval of parameter values. There are two branches which exist up to the point $\gamma = 2.59$ where they collide in a saddle-node bifurcation. One of these, the red diamonds branch, is mostly unstable except for $\gamma \in [1.26, 1.33] \cup [2, 2.11]$. For $\gamma < 1.26$, this branch has one real and one imaginary pair, which become both imaginary for $\gamma > 1.26$ until they collide for $\gamma = 1.33$ and yield a complex quartet, which subsequently splits into two imaginary pairs for $\gamma = 2$ and finally into one real and one imaginary pair for $\gamma > 2.11$. The other one, the black squares branch, is always unstable due to one real and one imaginary pair. When these two modes collide, a collision arises between both their real and their imaginary (respective) eigenvalue pairs.

Aside from the other two branches, the branch associated with the blue stars emerges from $\gamma = 1$ and persists beyond the above critical point (and for all values of $\gamma$ that we have monitored). In our case, this branch is only stable for $\gamma < 1.25$, at which two pairs of imaginary eigenvalues collide and lead to a complex quartet, which renders the branch unstable thereafter. This branch behaves very similarly as the one in the linear $\mathcal{PT}$ trimer case reported in [13]. Both of them bifurcate from zero amplitude

after a certain value of $\gamma$, persist beyond the linear $\mathcal{PT}$ critical point and have similar stability properties.
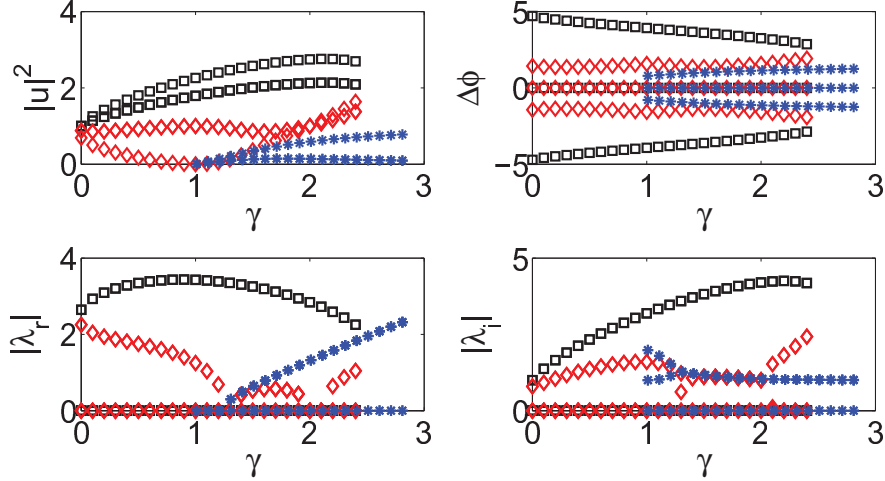


**Figure 3.4.** The symmetric solution profiles of Case I in the nonlinear-PT-symmetric trimer with $\epsilon = 1$, $E = 1$, $\rho_r = -1$ and $\rho_{im} = 1$. The three branches are denoted by blue stars, red diamonds and black squares and their amplitudes (top left), phases (top right), real part (bottom left) and imaginary part (bottom right) of the corresponding eigenvalues are shown. See also the relevant discussion in the text.
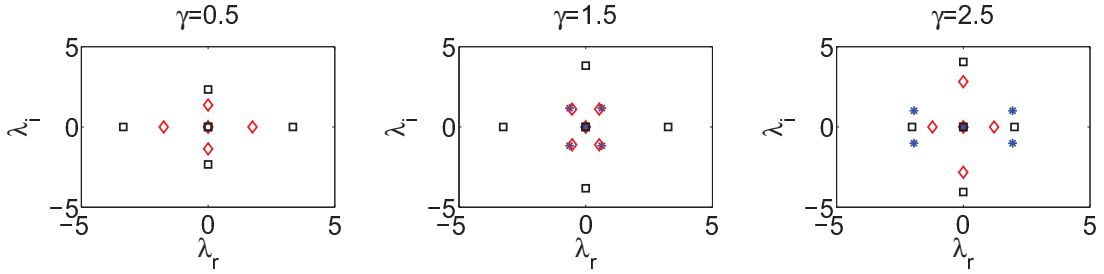


**Figure 3.5.** The spectral plane of the linear stability analysis for the symmetric solutions of Case I with $\epsilon = 1$, $E = 1$, $\rho_r = -1$ and $\rho_{im} = 1$, for three different values of $\gamma = 0.5$, $1.5$ and $2.5$. Each branch is associated with three eigenvalue pairs one of which is at $0$ due to symmetry.

To monitor the dynamical evolution of the different branches, we used direct numerical simulations illustrated in Fig. 3.6 for the case of $\gamma = 1.5$. Two of the branches, the blue stars of the left panel and the red diamonds of the middle one are oscillatorily

unstable for this value of $\gamma$, while the black squares branch is always unstable due to a real eigenvalue pair. The latter has been found to generically cause the unbounded gain of at least one node within the trimer. The oscillatory instability, on the other hand, in the case of the blue branch and for $\gamma = 1.5$ can be observed to lead to a long-lived periodic exchange of "power" between the three sites. On the other hand, for the red diamonds branch of the middle panel, while there is an intermediate stage of power oscillations between the three nodes, the ultimate fate of the configuration favors the unbounded growth of at least one node (in fact, two nodes in the example shown) of the trimer.



(a)  blue stars branch         (b)  red diamonds branch         (c)  black squares branch
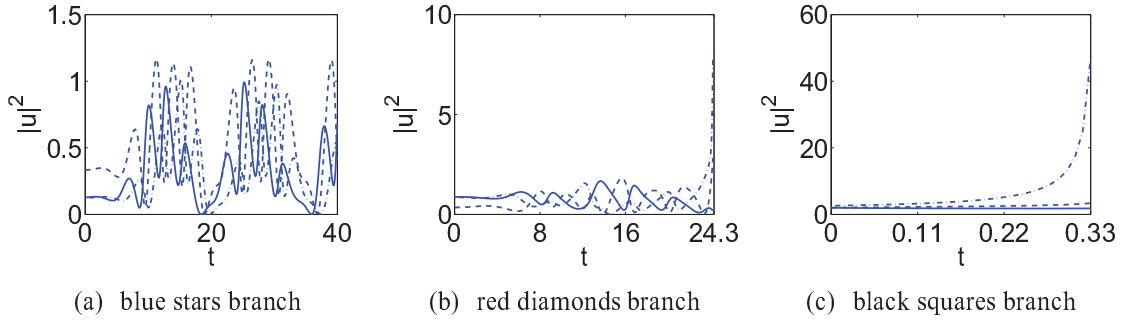
**Figure 3.6.** The time evolution plots of the trimer case I with $\epsilon = 1$, $E = 1$, $\rho_r = -1$ and $\rho_{im} = 1$ when $\gamma = 1.5$. For each branch, the solid line denotes the nonlinear loss/linear gain site, the dot-dashed line denotes the nonlinear gain/linear loss site, while the dashed line represents the inert site between the two. Notice the oscillatory evolution of the stars branch, while the diamonds and squares lead to ultimate unbounded increase of at least one site within the trimer.

- Trimer Case II:

    According to Eq. (3.60), one of the parameters should be determined by the others. We hereby set $\epsilon = 1$, $\rho_r = -1$ and $\rho_{im} = 1$, then $E$ is obtained self-consistenly for a given choice of $\gamma$. The solution profiles, which are obtained by solving Eq. (3.60) numerically, are plotted in Fig. 3.7. There are three pairs of branches, i.e., six branches of solutions in total found in this case. Only one out of each pair is shown in Fig. 3.7-3.9 (to avoid cluttering of the relevant figures), namely the blue stars, red diamonds
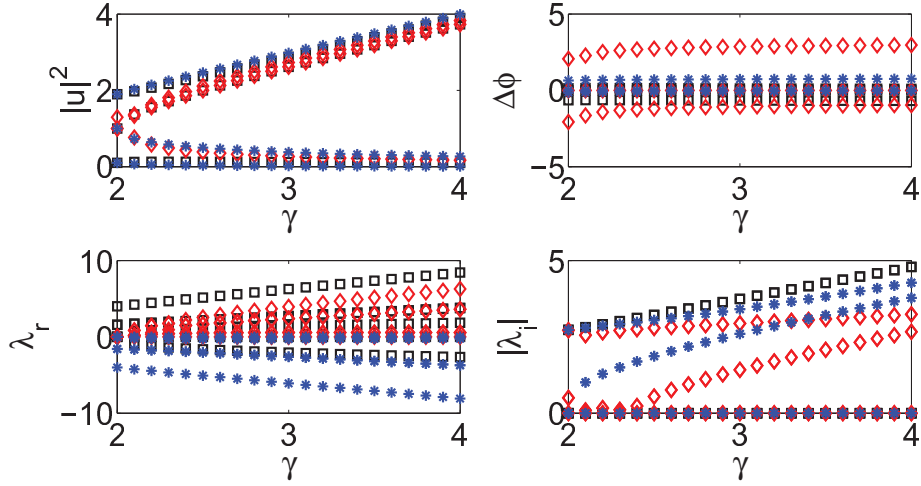
**Figure 3.7.** The solution profile of the trimer case II with $\epsilon = 1$, $\rho_r = -1$ and $\rho_{im} = 1$. The three branches are denoted by blue stars, red diamonds and black squares. These branches start at $\gamma = 2$ (except for the red diamonds branch that is initiated at $\gamma = 2.05$) and exist even when $\gamma$ is large.

and black squares. The other three branches are mirror symmetric to these branches, respectively. For example, the existence profile of the mirror symmetric branch of the blue stars would be identical to the blue stars shown in Fig. 3.7, while its stability plot would be mirror symmetric about the imaginary axis to the blue stars shown in Fig. 3.8. Among the three branches shown in Fig. 3.7, two of them emerge at $\gamma = 2$ and persist throughout the range of $\gamma$ values considered. It should be noticed that the amplitudes are different within each branch. The blue stars (dynamically stable) branch has a large $A$ and small $B$ and $C$, while the red diamonds and black squares branches have a fairly small $A$ and large values of $B$ and $C$. In fact, precisely at the critical point of the branches' emergence, the blue stars and the black squares are exact mirror images of each other (i.e., they have the same amplitude for $B$ and the one's $A$ is the other's $C$ -and vice versa-). This mirror symmetry is in fact directly reflected in the eigenvalues of the linearization around the two configurations, one set of which (for the blue stars) possesses negative real parts, while the other (black squares) has mirror symmetric positive ones. As can be perhaps intuitively anticipat-

ed, the more stable configuration is the one having large amplitude at the nonlinear loss/linear gain site. The third branch (red diamonds) is also highly unstable and emerges out of a bifurcation at $\gamma = 2.05$ (to which we will return when discussing case III).
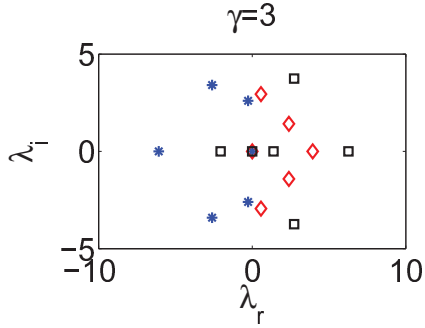


**Figure 3.8.** The spectral stability plots of the trimer case II with $\epsilon = 1$, $\rho_r = -1$ and $\rho_{im} = 1$, illustrating the stability of the blue stars branch and the instability of the other two.

Fig. 3.8 shows the eigenvalues of the three branches clearly illustrating the fact that they are not symmetric about the imaginary axis. This can once again be justified by the asymmetry of the configurations of case II which, in turn, break the $\mathcal{PT}$ symmetry of the linearization matrix and hence lead to asymmetric spectra. The blue stars branch is always stable, as indicated above, and the other two branches are always unstable as $\gamma$ increases. For instance, for the red diamond branch, there exists (in addition to a zero eigenvalue) an imaginary pair, a complex conjugate pair (with a positive real part) and a real eigenvalue. In the case of the black squares branch, there are (in addition to the zero eigenvalue) three real pairs (two positive and one negative) and a complex conjugate pair (with positive real part).

Fig. 3.9 shows the dynamical plots of the three distinct branches of solutions. The blue stars branch clearly preserves its configuration due to its dynamical stability, while for the two unstable branches, their evolution gives rise to asymmetric dynamics favoring the loss of the power in a single site (the nonlinear gain/linear loss one),

(a) blue stars branch  (b) red diamonds branch  (c) black squares branch
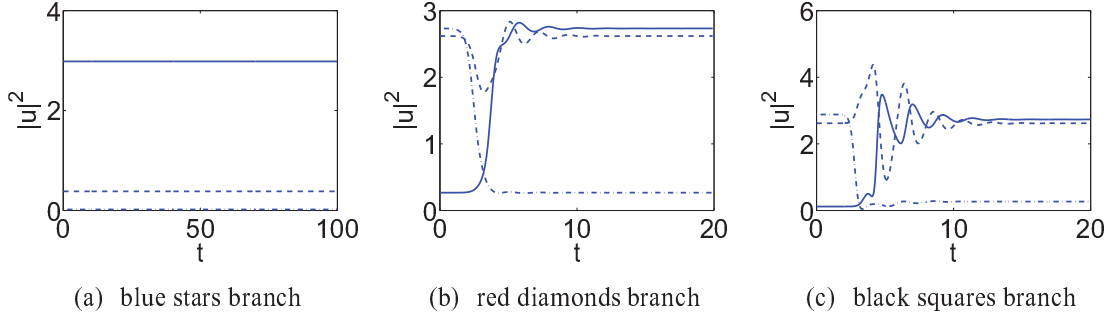
**Figure 3.9.** The time evolution plots of the trimer case II with $\epsilon = 1$, $\rho_r = -1$ and $\rho_{im} = 1$ when $\gamma = 3$. The two unstable branches (red diamonds and black squares) tend to a dynamically stable configuration which is a mirror image of the red diamonds branch.

and quickly absorbed by a stable state. The latter state appears to be the mirror symmetric of the red diamonds asymmetric branch in both cases. This is indeed also a stable dynamical state of the original stationary system of equations. Furthermore, this state is expected to exist based on the symmetry breaking bifurcation that we will discuss below as giving rise to the red diamonds branch. As remarked above, the stability properties of the mirror symmetric branches are mirror symmetric to the ones shown in Fig. 3.8. This implies that only the mirror symmetric branch of the red diamonds is stable, which is, in turn, consonant with our observation that it is a potential attractor for the dynamics for $\gamma = 3$ shown in Fig. 3.9.

- Trimer Case III:

Finally, we turn to a consideration, using the same parametric setting as in case II, of the numerical results by solving Eq. (3.67) for case III in Figs. 3.10-3.12. Four distinct branches of solutions are observed in this case. The branches denoted by red diamonds and black squares exist only for small values of the linear gain/loss parameter $\gamma$, are stable and terminate at $\gamma = 0.65$. The other two branches, namely the blue stars and the green circles collide and terminate at $\gamma = 2.1$. The green circles branch is unstable in this case, due to a complex quartet of eigenvalues (observed in Fig. 3.11). On the other hand, the blue stars' branch is stable up to $\gamma = 2.05$ a critical
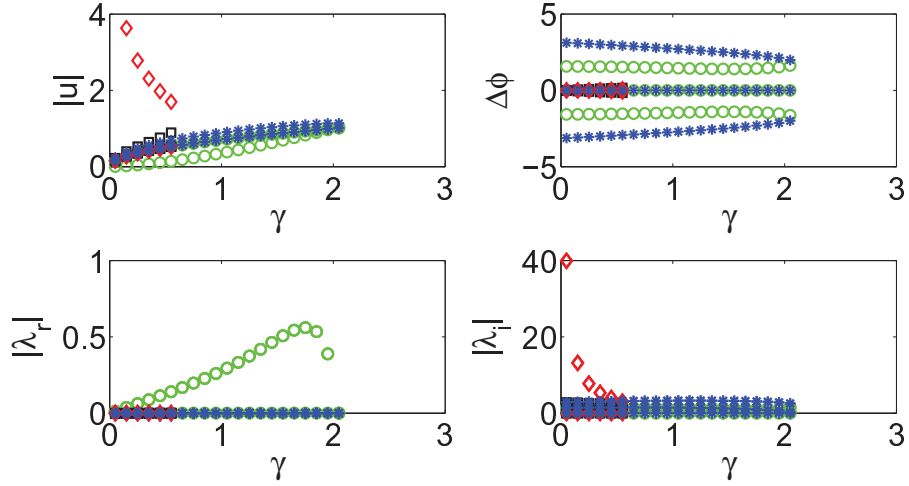
**Figure 3.10.** The solution profile (amplitude (a), phase (b)) and the stability (real (c) and imaginary (d) part of the eigenvalues) for the nonlinear $\mathcal{PT}$-symmetric trimer of Case III (special symmetric solutions) with $\epsilon = 1$, $\rho_r = -1$ and $\rho_{im} = 1$. The norms are not squared in the top left panel to improve the visibility of the branches (given the disparity of the relevant amplitudes). The four branches are denoted by blue stars, red diamonds, black squares and green circles. The blue stars, red diamonds and black squares branches always have two pairs of purely imaginary eigenvalues, while the green circles branch always has a complex quartet. The blue stars branch terminates with the green circles at $\gamma = 2.1$, while the red diamonds and black squares terminate together at $\gamma = 0.65$.

point at which branches of case II (the red diamonds branch referred to in case II as having a pitchfork bifurcation at the same value and its mirror symmetric image) emerge. Notice that this detail is not discernible in the eigenvalue plots of Fig. 3.10.
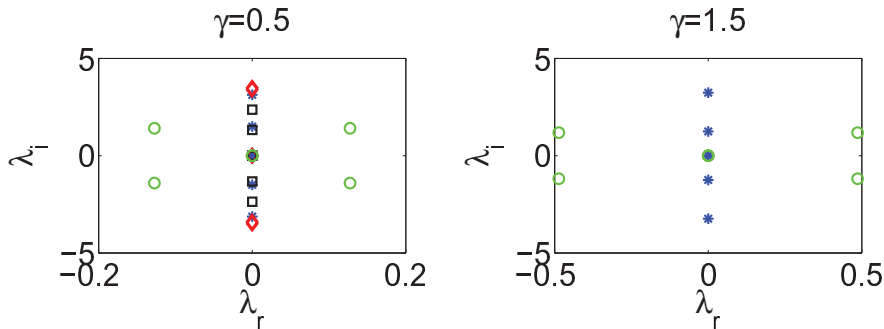


**Figure 3.11.** The plots of the spectral plane of the linear stability eigenvalues for the nonlinear-PT-symmetric trimer Case III (special symmetric solutions) with $\epsilon = 1$, $\rho_r = -1$ and $\rho_{im} = 1$.

The dynamics of the different configurations are shown in Fig. 3.12. The blue stars, red diamonds and black squares special symmetric branches of solutions are stable and thus preserve their shape. On the other hand, the green circles for $\gamma = 0.5$ are subject to the oscillatory instability predicted by the linear stability analysis. This, in turn, results into long-lived oscillatory dynamics of the system, as indicated in the bottom right of Fig. 3.12.



(a) blue stars branch

(b) red diamonds branch

(c) black squares branch

(d) green circles branch
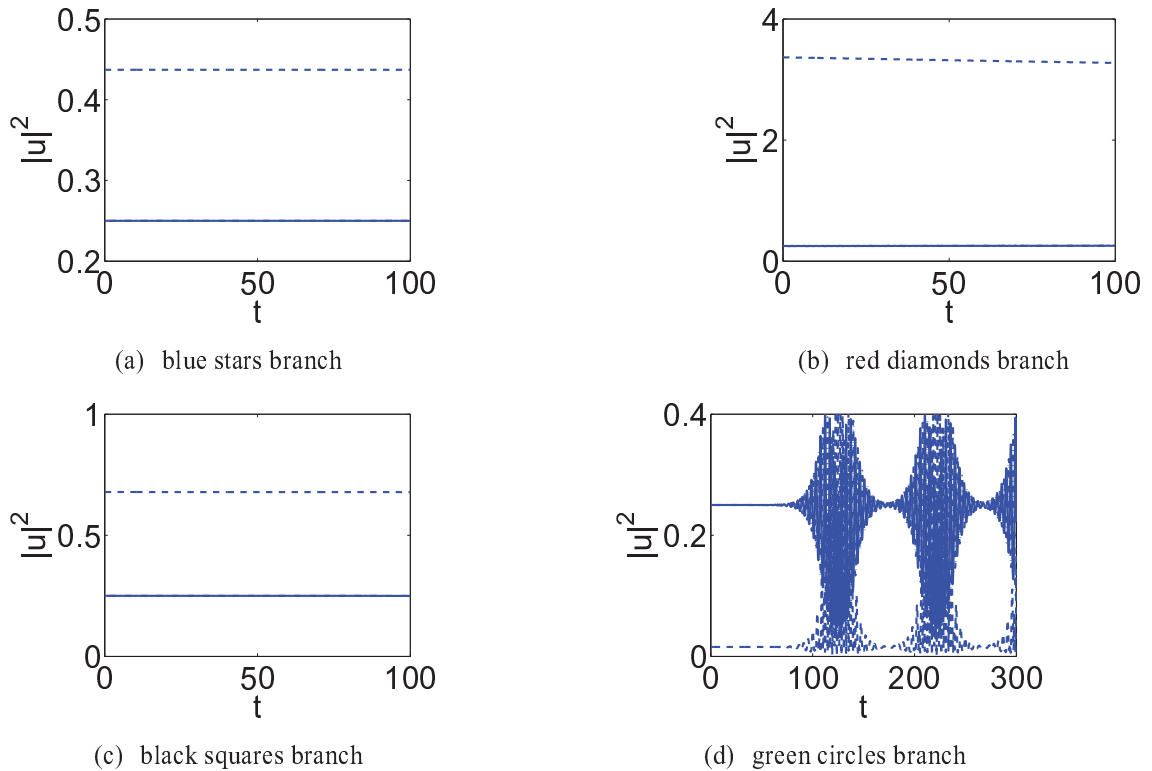
**Figure 3.12.** The time evolution plots of the nonlinear-PT-symmetric trimer in Case III of special symmetric solutions with $\epsilon = 1$, $\rho_r = -1$ and $\rho_{im} = 1$ when $\gamma = 0.5$. The only unstable configuration is the green circle one of the bottom right which leads to long-lived oscillatory dynamics.

# CHAPTER 4

# TWO DIMENSIONAL $\mathcal{PT}$-SYMMETRIC PLAQUETTES



(a) mode 0+0–    (b) mode +–+–    (c) mode ++– –    (d) mode +–0+–
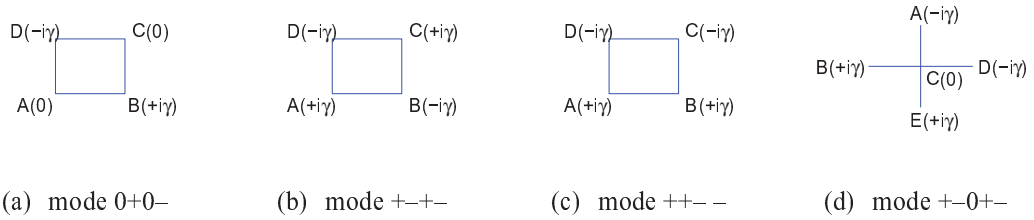
**Figure 4.1.** (Color online) The different fundamental plaquette configurations (i.e., two-dimensional *oligomers*) including the linear balanced gain and loss. Among these, (a), (c) and (d) are $\mathcal{PT}$-symmetric, while (b) is not in the strict sense, but it is interesting too, as an implementation of alternating gain and loss nodes in the plaquette pattern. The nodes are labeled so as to connect the gain-loss profiles to the evolution of individual nodes in dynamical simulations. The sets are coded by chains of symbols, with $+, -$ and $0$ corresponding, respectively, to the linear gain, loss, or absence of either effect at particular sites.

In Chapter 2 and Chapter 3, we have considered one-dimensional linear and nonlinear $\mathcal{PT}$-invariant systems. This chapter aims to make a basic step in this direction, by introducing fundamental two dimensional plaquettes consisting, typically, of four sites (in one case, it will be a five-site cross). These configurations, illustrated by Fig. 4.1, are inspired by earlier works on 2D Hamiltonian lattices described by discrete nonlinear Schrödinger equations [36], where diverse classes of modes, including discrete solitary vortices [37, 38], have been predicted and experimentally observed [39, 40]. The plaquettes proposed herein should be straightforwardly accessible with current experimental techniques in nonlinear optics, as a straightforward generalization of the coupler-based setting reported in Ref. [5].

# I   Existence, stability and dynamics of nonlinear states

In this section, we seek stationary solutions of the type

$$\mathbf{u}_0(t) = e^{-iEt}\mathbf{u}_0, \qquad E \in \mathbb{R}, \qquad \mathbf{u}_0 = (a, b, c, d)^T \in \mathbb{C}^4 \qquad (4.1)$$

constructed over constant vectors $\mathbf{u}_0$. We note that restricting the explicit analysis to stationary solutions of the type (4.1) we by construction exclude from this analysis $\mathcal{PT}-$violating solutions with $E \notin \mathbb{R}$ which are necessarily non-stationary, i.e., we do not consider ghost states).

## I.1   The plaquette of the 0+0– type

We start from the 2D plaquette of 0+0– type depicted as configuration (a) in Fig. 4.1. This plaquette has only two (diagonally opposite) nodes carrying the gain and loss, while the other two nodes bear no such effects. Using same notations as before, the corresponding dynamical equations for the amplitudes at the four sites of this oligomer are

$$
\begin{aligned}
i\dot{u}_A &= -k(u_B + u_D) - |u_A|^2 u_A, \\
i\dot{u}_B &= -k(u_A + u_C) - |u_B|^2 u_B + i\gamma u_B, \\
i\dot{u}_C &= -k(u_B + u_D) - |u_C|^2 u_C, \\
i\dot{u}_D &= -k(u_A + u_C) - |u_D|^2 u_D - i\gamma u_D, \qquad (4.2)
\end{aligned}
$$

where $\gamma \in \mathbb{R}$ is the above-mentioned gain-loss coefficient, and $k \in \mathbb{R}$ is a real coupling constant. The nonlinearity coefficients are scaled to be 1.

Substituting ansatz (4.1) for the stationary solutions in Eq. (4.2) we obtain the following algebraic equations:

$$
\begin{aligned}
Ea &= k(b+d) + |a|^2 a, \\
Eb &= k(a+c) + |b|^2 b - i\gamma b, \\
Ec &= k(b+d) + |c|^2 c, \\
Ed &= k(a+c) + |d|^2 d + i\gamma d, \quad (4.3)
\end{aligned}
$$

These equations can be analyzed via amplitude-phase decomposition

$$
a = Ae^{i\phi_a}, b = Be^{i\phi_b}, c = Ce^{i\phi_c}, d = De^{i\phi_d}. \quad (4.4)
$$

Without loss of generality, we may fix $\phi_a = 0$.

Using this condition in Eq. (4.3) and dividing each equation (4.3) by the phase factor on its left-hand side, one obtains the imaginary parts of the resulting equations:

$$
\begin{aligned}
0 &= kB\left[\sin(\phi_b - \phi_a) + \sin(\phi_d - \phi_a)\right] = 2kB\sin\left(\frac{\phi_b + \phi_d}{2} - \phi_a\right)\cos\left(\frac{\phi_b - \phi_d}{2}\right), \\
\gamma B &= kA\left[\sin(\phi_a - \phi_b) + \sin(\phi_c - \phi_b)\right] = 2kA\sin\left(\frac{\phi_a + \phi_c}{2} - \phi_b\right)\cos\left(\frac{\phi_a - \phi_c}{2}\right), \\
0 &= kB\left[\sin(\phi_b - \phi_c) + \sin(\phi_d - \phi_c)\right] = 2kB\sin\left(\frac{\phi_b + \phi_d}{2} - \phi_c\right)\cos\left(\frac{\phi_b - \phi_d}{2}\right), \\
-\gamma B &= kA\left[\sin(\phi_a - \phi_d) + \sin(\phi_c - \phi_d)\right] = 2kA\sin\left(\frac{\phi_a + \phi_c}{2} - \phi_d\right)\cos\left(\frac{\phi_a - \phi_c}{2}\right).
\end{aligned}
$$

$$(4.5)$$

For $\phi_a = 0$ the first of these equations implies $\sin(\phi_b) = -\sin(\phi_d)$, hence either $\phi_b = -\phi_d$ (case 1) or $\phi_d = \phi_b - \pi$ (case 2). In case 1, we conclude from the third equation that either $\phi_b \neq \pm\pi/2$ and $\phi_c = 0$ (case 1a), or $\phi_b = \pm\pi/2$ and $\phi_c$ is arbitrary (case 1b). In case 2 the third equation is satisfied automatically. In all three cases, the second and the fourth equation are compatible. They give

$$\text{case 1a:} \qquad \sin(\phi_b) = -\frac{\gamma B}{2kA}, \qquad \phi_c = 0, \qquad \phi_d = -\phi_b,$$

$$\text{case 1b:} \qquad \cos(\phi_c) = \mp\frac{\gamma B}{kA} - 1, \qquad \phi_d = -\phi_b = \mp\pi/2,$$

$$\text{case 2:} \qquad \sin(\phi_b) + \sin(\phi_b - \phi_c) = -\frac{\gamma B}{kA}, \qquad \phi_d = \phi_b - \pi. \quad (4.6)$$

Returning to the phase-factor divided equations (4.3) and considering their real parts, we find

$$
\begin{aligned}
EA &= kB\left[\cos(\phi_b - \phi_a) + \cos(\phi_d - \phi_a)\right] + A^3, \\
EB &= kA\left[\cos(\phi_a - \phi_b) + \cos(\phi_c - \phi_b)\right] + B^3, \\
EA &= kB\left[\cos(\phi_b - \phi_c) + \cos(\phi_d - \phi_c)\right] + A^3, \\
EB &= kA\left[\cos(\phi_a - \phi_d) + \cos(\phi_c - \phi_d)\right] + B^3. \quad (4.7)
\end{aligned}
$$

The pairwise compatibility of the first and third, as well as of the second and fourth equations requires

$$
\begin{aligned}
\cos(\phi_b - \phi_a) + \cos(\phi_d - \phi_a) &= \cos(\phi_b - \phi_c) + \cos(\phi_d - \phi_c), \\
\cos(\phi_a - \phi_b) + \cos(\phi_c - \phi_b) &= \cos(\phi_a - \phi_d) + \cos(\phi_c - \phi_d). \quad (4.8)
\end{aligned}
$$

For case 1a, these conditions are trivially satisfied, whereas for the remaining cases they lead to further restrictions:

$$\text{case 1b:} \qquad \phi_c = 0; \pi \qquad \Longrightarrow \qquad \gamma = \mp\frac{2kA}{B};$$

$$\gamma = 0;$$

$$\text{case 2:} \qquad\qquad \phi_c = 2\phi_b \pm \pi, \quad \sin(\phi_b) = -\frac{\gamma B}{2kA}. \quad (4.9)$$

In this way the phase angles are fixed for all the three cases and we can turn to the amplitudes. The corresponding equation sets reduce to

$$\text{case 1a:} \qquad EA = 2kB\cos(\phi_b) + A^3,$$

$$EB = 2kA\cos(\phi_b) + B^3,$$

$$\text{case 1b,2:} \qquad E = A^2 = B^2. \qquad (4.10)$$

In the latter two cases (1b and 2) the amplitudes and phases completely decouple and we have

$$A = B = C = D = \sqrt{|E|}. \qquad (4.11)$$

Case 1a allows for a richer behavior. Equating the terms $2k\cos(\phi_b)$ in the upper two equations (4.10) leads to the constraint

$$A^2(E - A^2) = B^2(E - B^2), \qquad (4.12)$$

which can be resolved by $A = B$ (case 1aa) as well as by $E = A^2 + B^2$ (case 1ab). The analysis of these two cases can be completed with the help of the relation $\cos(\phi_b) = \pm\sqrt{1 - \frac{\gamma^2 B^2}{4k^2 A^2}}$ from Eq. (4.6).

As result we obtain the following set of stationary solutions:

$$\text{case 1a:} \qquad \sin(\phi_b) = -\frac{\gamma B}{2kA}, \qquad \phi_c = 0, \qquad \phi_d = -\phi_b,$$

$$\text{case 1aa:} \qquad A = B = C = D = \sqrt{E + \sqrt{4k^2 - \gamma^2}}, \qquad (4.13)$$

$$\text{case 1ab:} \qquad A = B = C = D = \sqrt{E - \sqrt{4k^2 - \gamma^2}}, \qquad (4.14)$$

$$\text{case 1b:} \qquad \phi_d = -\phi_b = \mp\pi/2, \quad \phi_c = 0, \pi, \qquad \gamma = \pm 2k, \quad \gamma = 0,$$

$$A = C, \; B = D = \frac{2kA}{\sqrt{A^4 + \gamma^2}}, \quad E = A^2 + B^2, \qquad (4.15)$$

$$\text{case 2:} \qquad \sin(\phi_b) = -\frac{\gamma}{2k}, \qquad \phi_d = \phi_b - \pi, \qquad \phi_c = 2\phi_b \pm \pi,$$

$$A = B = C = D = \sqrt{E}. \qquad (4.16)$$

The linear stability analysis was performed numerically. Subsequently we present corresponding graphical results. The plaquettes (b) - (d) can be analyzed in a similar way.

64

For brevity's sake, in Fig. I.1 we present only the basic numerical results, by means of the following symbols:
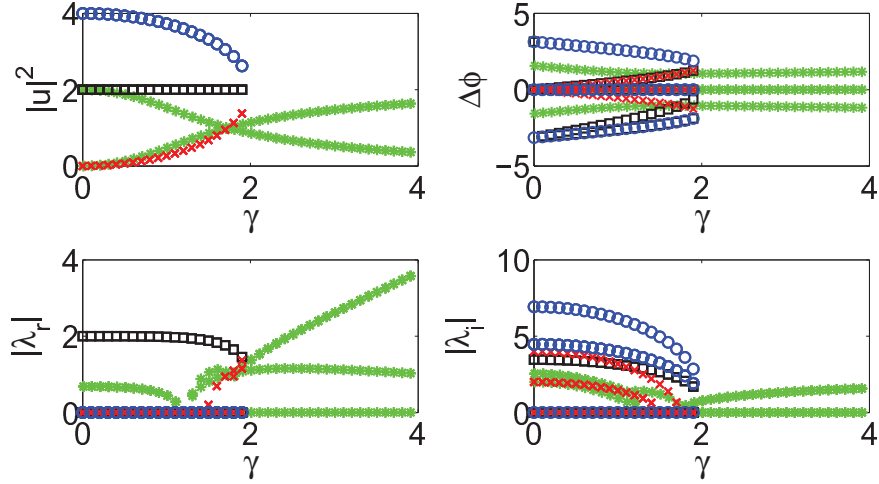


**Figure 4.2.** (Color online) Profiles of the solutions for plaquette (a) from Fig. 4.1, with $E = 2$ and $k = 1$. Four different branches of the solutions are denoted by blue circles, red crosses, black squares and green stars. The top left and right panel display, respectively, the squared absolute values of the amplitudes and phase differences between adjacent sites for the respective states. The bottom left and right panels show real (the instability growth rates) and imaginary (oscillation frequencies) parts of the eigenvalues produced by the linearization around the stationary states. The continuations are shown versus the gain-loss parameter $\gamma$.

- case 1aa with $A = B = C = D = \sqrt{E + \sqrt{4k^2 + \gamma^2}}$     — blue circles;

- case 1aa with $A = B = C = D = \sqrt{E - \sqrt{4k^2 - \gamma^2}}$     — red crosses;

- case 1ab — green stars;

- case 2 — black squares;

- Case 1b is not depicted explicitly because it corresponds to point configurations without gain-loss ($\gamma = 0$) and to exceptional point configurations $\gamma = \pm 2k$.

Figure I.1 presents the mode branches (their amplitudes, phases, and also their stability) over the gain-loss parameter $\gamma$, starting from the conservative system at $\gamma = 0$. The same

symbols are used in Fig. 4.3, which displays typical examples of the spectral plane $(\lambda_r, \lambda_i)$ for stability eigenvalues $\lambda = \lambda_r + i\lambda_i$ of the linearization; recall that the modes are unstable if they give rise to $\lambda_r \neq 0$. Explicitly we observe the following behavior.
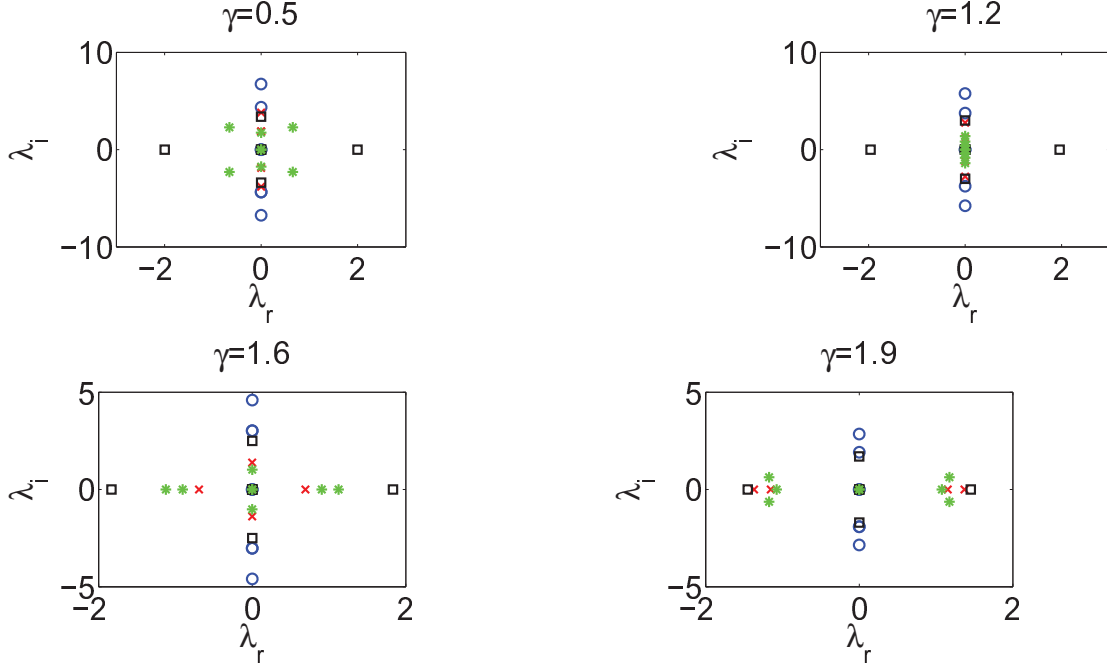


**Figure 4.3.** (Color online) The stability plots for plaquette (a) from Fig. 4.1 with $E = 2$ and $k = 1$, for different values of $\gamma$. The notation for different branches is the same as in the previous figure. All branches are shown for $\gamma = 0.5$, $\gamma = 1.2$, $\gamma = 1.6$, and $\gamma = 1.9$ (top left, top right, bottom left, and bottom right panels, respectively).

- case 1aa with $A = B = C = D = \sqrt{E + \sqrt{4k^2 + \gamma^2}}$ — blue circles

  According to Fig. 4.3, the present solution is stable. Notice that, although featuring a phase profile, it cannot be characterized as a vortex state (the same is true for some other configurations carrying phase structure). Interestingly, the relevant configuration is generically stable bearing two imaginary pairs of eigenvalues.

- case 1aa with $A = B = C = D = \sqrt{E - \sqrt{4k^2 - \gamma^2}}$ — red crosses.

  Obviously, this kind of solutions as well as the previous one exist up to the exceptional point $\gamma = \pm 2k$ of the $\mathcal{PT}$-symmetry breaking in the linear system, where the

two branches collide and disappear (leave the stationary regime and become nonstationary). As seen in Fig. 4.3, the present branch has two eigenvalue pairs which are purely imaginary for small $\gamma$, but become real (rendering the configuration unstable) at $\gamma = 1.49$ and then $\gamma = 1.73$, respectively. Ultimately, these pairs of unstable eigenvalues collide at the origin of the spectral plane with those of the previous branch (blue circles).

- case 1ab — green stars.

  This stationary solution has a number of interesting features. Firstly, it is the only one among the considered branches which has two unequal amplitudes. Secondly, it exists past the critical point $\gamma = \pm 2k$ of the linear system, due to the effect of the nonlinearity (the extension of the existence region for nonlinear modes was earlier found in 1D couplers [23] and oligomers [13, 31]). Furthermore, this branch has three non-zero pairs of stability eigenvalues, two of which form a quartet for small values of the gain-loss parameter, while the third is imaginary (i.e., the configuration is unstable due to the real parts of the eigenvalues within the quartet). At $\gamma = 1.17$, the eigenvalues of the complex quartet collapse into two imaginary pairs, rendering the configuration stable, in a narrow parametric interval. At $\gamma = 1.24$, the former imaginary pair becomes real, destabilizing the state again, while subsequent bifurcations of imaginary pairs into real ones occur at $\gamma = 1.28$ and $\gamma = 1.74$ (at the latter point, all three non-zero pairs are real). Shortly thereafter, two of these pairs collide at $\gamma = 1.76$ and rearrange into a complex quartet, which exists along with the real pair past that point.

- case 2 — black squares. In contrast to all other branches, this one is *always* unstable. One of the two nonzero eigenvalue pairs is always real (while the other is always imaginary), as seen in Fig. 4.3. This branch also terminates at the exceptional point $\gamma = \pm 2k$, as relation $\sin(\phi_b) = -\gamma/(2k)$ cannot hold at $|\gamma| > |2k|$. This branch

collides with the two previous ones via a very degenerate bifurcation (that could be dubbed a "double saddle-center" bifurcation), which involves 3 branches instead of two as in the case of the generic saddle-center bifurcation, and two distinct eigenvalue pairs colliding at the origin of the spectral plane.



(a)  blue circle branch

(b)  red cross branch

(c)  black square branch

(d)  green star branch
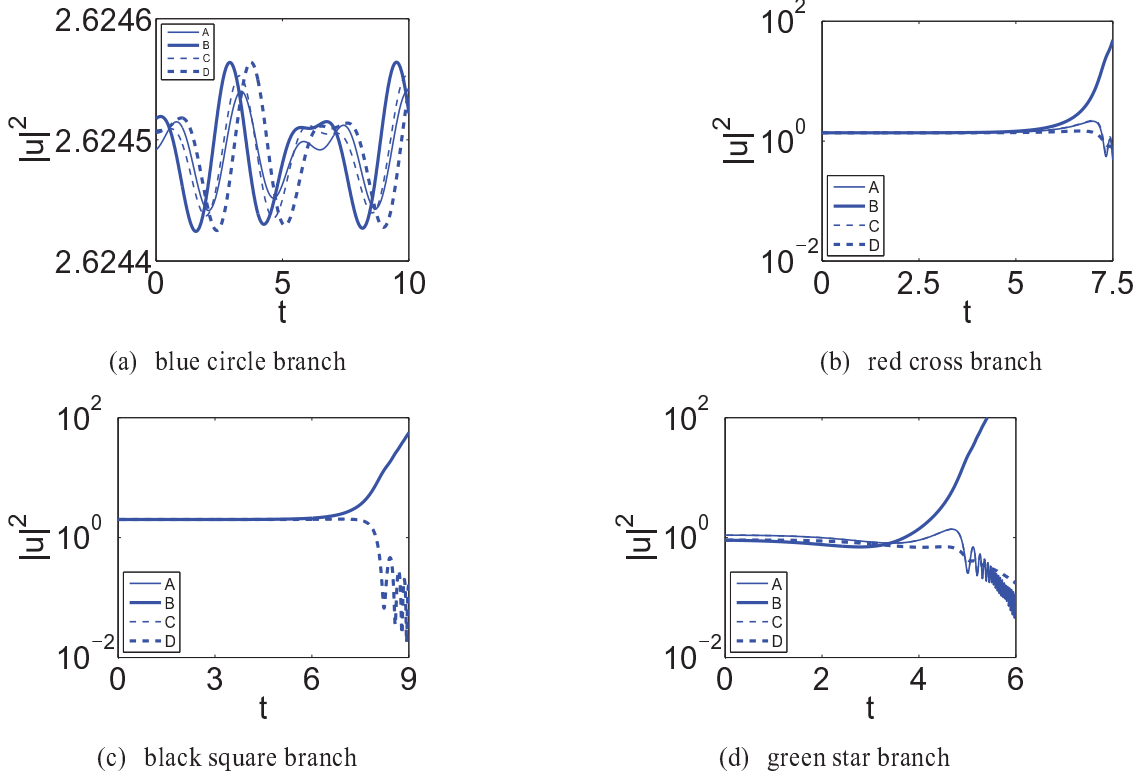
**Figure 4.4.** (Color online) The perturbed evolution of different branches from Figs. I.1 and 4.3 at $\gamma = 1.9$. Thin solid, thick solid, thin dashed, and thick dashed curves correspond to nodes A, B, C, D in Fig. 4.1(a), respectively. In panel (b), the plots pertaining to sites A and C [see Fig. 4.1(a)] overlap. Similarly, pairs of the plots for (A,B) and (C,D) overlap in (c), and for (A,C) they overlap in (d).

By means of direct simulations, we have also examined the dynamics of the modes belonging to different branches in Fig. 4.4. The stable blue-circle branch demonstrates only oscillations under perturbations. This implies that, despite the presence of the gain-loss profile, none of the perturbation eigenmodes grows in this case. Nevertheless, the three other branches ultimately manifest their dynamical instability, which is observed through the growth of the amplitude at the gain-carrying site [B, in Fig. 4.1(a)] at the expense of the

lossy site (D). That is, the amplitude of the solution at the site with the gain grows, while the amplitude of the solution at the dissipation site loses all of its initial power. Depending on the particular solution, passive sites (the ones without gain or loss, such as A and C) may be effectively driven by the gain (as in the case of the black-square-branch, where the site A is eventually amplified due to the growth of the amplitude at site B) or by the loss (red-cross and green-star branches, where, eventually, the amplitudes at both A and C sites lose all of their optical power).

### I.2 The plaquette of the +–+– type

We now turn to the generalized (not exactly $\mathcal{PT}$-symmetric) configuration featuring the alternation of the gain and loss along the plaquette in panel (b) of Fig. 4.1. Apart from the two $\mathcal{PT}-$symmetry violating solutions, there should exist at least two stationary solutions which we construct in analogy to [cf. Eqs. (4.3)] from

$$
\begin{aligned}
Ea &= k(b+d) + |a|^2a - i\gamma a, \\
Eb &= k(a+c) + |b|^2b + i\gamma b, \\
Ec &= k(b+d) + |c|^2c - i\gamma c, \\
Ed &= k(a+c) + |d|^2d + i\gamma d.
\end{aligned}
\tag{4.17}
$$

Substituting the Madelung representation (4.4) and setting $A = B = C = D$ (for illustration purposes, we focus here only on this simplest case), we obtain

$$
\sin(\phi_b - \phi_a) + \sin(\phi_d - \phi_a) = \sin(\phi_b - \phi_c) + \sin(\phi_d - \phi_c) = \frac{\gamma}{k}, \tag{4.18}
$$

$$
\cos(\phi_b - \phi_a) + \cos(\phi_d - \phi_a) = \cos(\phi_b - \phi_c) + \cos(\phi_d - \phi_c) = \frac{E - A^2}{k}. \tag{4.19}
$$

Further, fixing $\phi_a = \phi_c = 0$, Eqs. (4.18) and (4.19) yield

$$
\sin\phi_b = \sin\phi_d = \frac{\gamma}{2k}, \quad A^2 = E \pm \sqrt{4k^2 - \gamma^2}. \tag{4.20}
$$

Obviously, the solution terminates at point $\gamma = \pm 2k$. Similar to what was done above, the continuation of this branch and typical examples of its linear stability are shown in Figs. 4.5 and 4.6, respectively. From here it is seen that the blue-circle branch, which has a complex quartet of eigenvalues, is always unstable. In fact, the gain-loss alternating configuration is generally found to be more prone to the instability. The red-cross branch is also unstable via a similar complex quartet of eigenvalues. This quartet, however, breaks into two real pairs for $\gamma \geq 1.5$, and, eventually, the additional imaginary eigenvalue pair becomes real too at $\gamma > 1.74$, making the solution highly unstable with three real eigenvalue pairs. The manifestation of the instability is shown in Fig. 4.7, typically amounting to the growth of the amplitudes at one or more gain-carrying sites.
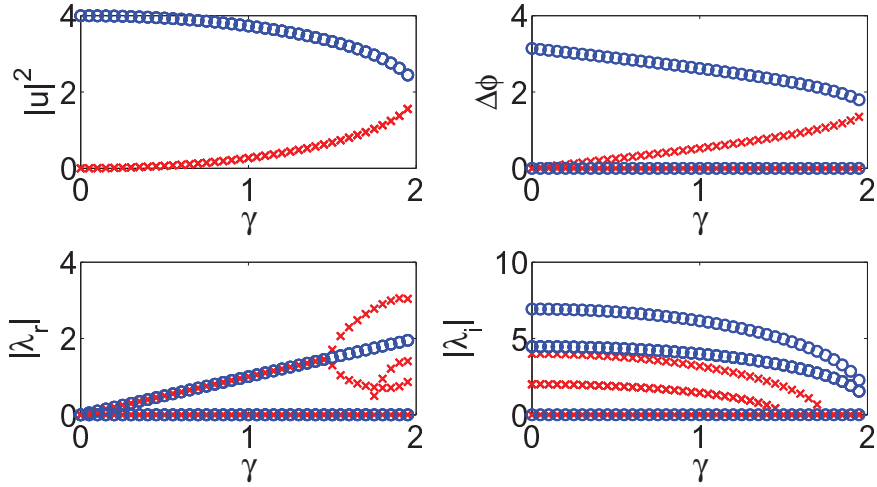


**Figure 4.5.** (Color online) The continuation of mode (4.20) and its stability, supported by plaquette (b) in Fig. 4.1, for $E = 2$ and $k = 1$.

## I.3 The plaquette of the $++--$ type

We now turn to the plaquette in Fig. 4.1(c), which involves parallel rows of gain and loss. In this case, the stationary equations are
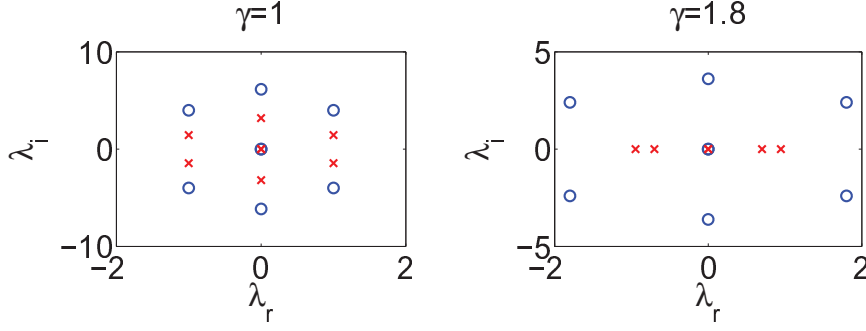
**Figure 4.6.** Two typical stability plots for branch (4.20), for $E = 2$, $k = 1$ and $\gamma = 1$ and 1.8, respectively.



(a)  blue circles branch          (b)  red crosses branch
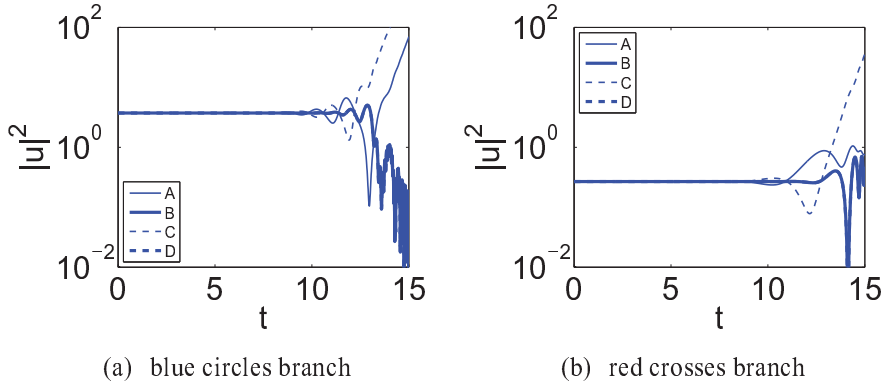
**Figure 4.7.** The perturbed evolution of the modes of type (4.20) at $\gamma = 1$ corresponding to the left panel of Fig. 4.6. The plots pertaining to sites B and D [see Fig. 4.1(b)] overlap in both panels.

$$
\begin{aligned}
Ea &= k(b+d) + |a|^2 a - i\gamma a, \\
Eb &= k(a+c) + |b|^2 b - i\gamma b, \\
Ec &= k(b+d) + |c|^2 c + i\gamma c, \\
Ed &= k(a+c) + |d|^2 d + i\gamma d.
\end{aligned}
\tag{4.21}
$$

In this case too, we focus on symmetric states of the form of $A = B = C = D$ [see Eq. (4.4)], which gives rise to two solutions displayed in Fig. 4.8, represented by the following analytical solutions:

71

$$A^2 = E - k \pm \sqrt{k^2 - \gamma^2}, \tag{4.22}$$

$$\phi_a = \phi_b = 0, \; \sin\phi_c = \sin\phi_d = \frac{\gamma}{k}; \tag{4.23}$$

$$A^2 = E + k \pm \sqrt{k^2 - \gamma^2}, \tag{4.24}$$

$$\phi_a = 0, \; \phi_b = \pi, \; \phi_c = \phi_d - \pi, \; \sin\phi_d = \frac{\gamma}{k}, \tag{4.25}$$

The analysis demonstrates that the branch with the upper sign in Eq. (4.22) is always unstable (through two real pairs of eigenvalues), as shown by blue circles in Fig. 4.8. On the other hand, the branch denoted by the red crosses, which corresponds to the lower sign in Eq. (4.22) is stable up to $\gamma = 0.86$, and then it gets unstable through a real eigenvalue pair. The black-squares branch with the upper sign in Eq. (4.24) is always stable, while the green-star branch with the lower sign in Eq. (4.24) is always unstable. At the linear-$\mathcal{PT}$-symmetry breaking point $\gamma = k$, we observe a strong degeneracy, since all the three pairs of eigenvalues for two of the branches (in the case of the blue circles, two real and one imaginary, and in the case of red crosses— one real and two imaginary) collapse at the origin of the spectral plane. On the other hand, the black-squares branch is always stable with three imaginary eigenvalue pairs, while the green-star branch has two imaginary and one real pair of eigenvalues. Between the latter two, there is again a collision of a pair at the origin at the critical condition, $\gamma = k$. Direct simulations, presented for $\gamma = 0.5$ in Fig. 4.9, demonstrate the stability of the lower-sign black-squares branch, while the instability of the waveform associated with the blue circles and the green stars leads to the growth and decay of the amplitudes at the sites carrying, respectively, the gain and loss. Notice that at the parameter values considered here, the red-cross branch is also dynamically stable as shown in the top right panel of Fig. 4.9.
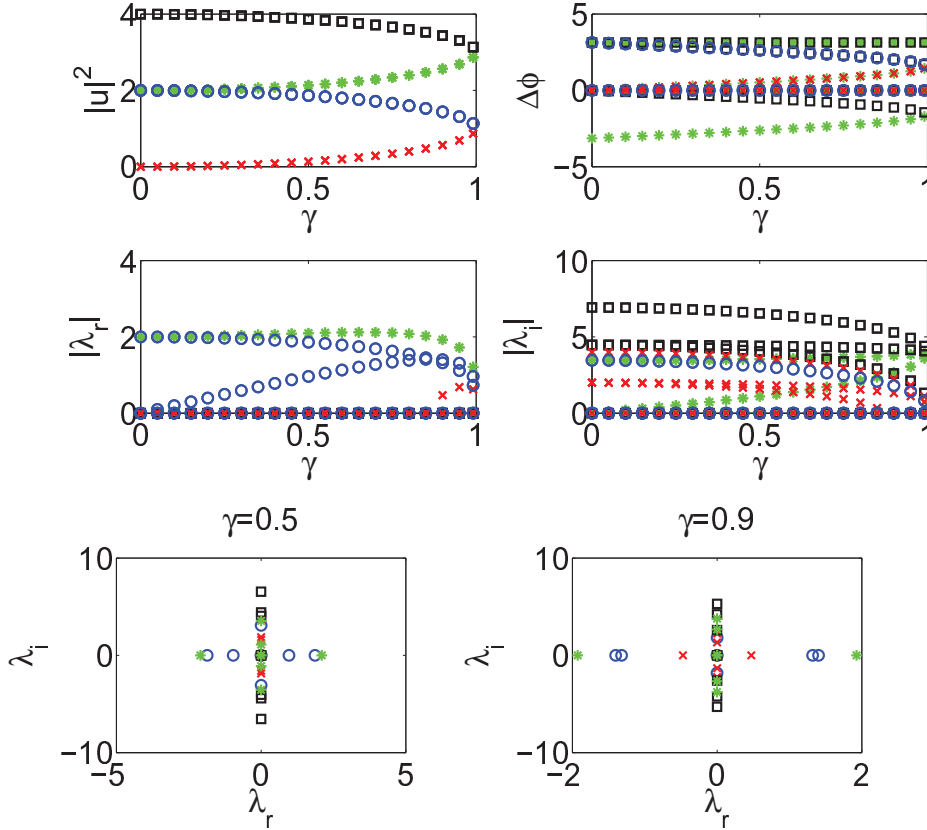
**Figure 4.8.** (Color online) The characteristics of the mode of the $++--$ type, supported by plaquette (c) in Fig. 4.1, and given in analytical form by Eqs. (4.22)-(4.25), for $E = 2$ and $k = 1$. The blue circles correspond to the completely unstable branch with the upper sign in Eq. (4.22), while the red crosses pertain to branch with the lower sign, which is stable at $\gamma < 0.86$. The black-square and green-star branches correspond to the upper and lower sign in Eq. (4.24), respectively. The former one is always stable, while the latter one is always unstable. All four branches terminate at the critical point $|\gamma| = |k|$ of the linear $\mathcal{PT}$-symmetric system.

## I.4 The plaquette of the $+-0+-$ type

Lastly, motivated by the existence of known "cross"-shaped discrete-vortex modes in 2D conservative lattices, in addition to the fundamental discrete solitons [36, 37], we have also examined the five-site configuration, in which the central site does not carry any gain or loss, while the other four feature a $\mathcal{PT}$-balanced distribution of the gain and loss, as shown in panel (d) of Fig. 4.1. Seeking for stationary states with propagation constant, $G$ [instead of $E$ in Eq. (4.1), as in this case we reserve label $E$ for one of the sites of the 5-site

73

(a) blue circles branch



(b) red crosses branch



(c) black squares branch



(d) green stars branch
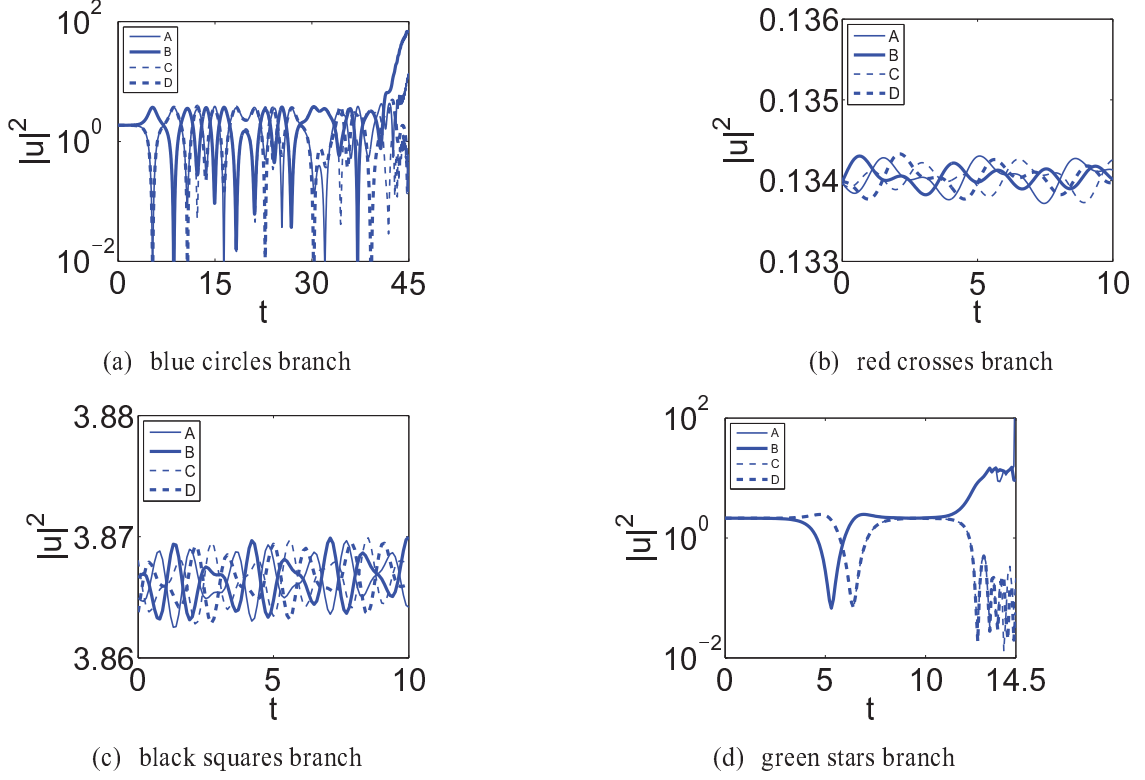
**Figure 4.9.** (Color online) The perturbed evolution of the four branches of the analytical solutions given by Eqs. (4.22)-(4.25), which correspond to Fig. 4.8 with $\gamma = 0.5$.

plaquette in Fig. 4.1(d)], we get:

$$
\begin{aligned}
Ga &= kc + |a|^2 a + i\gamma a, \\
Gb &= kc + |b|^2 b - i\gamma b, \\
Gc &= k(a + b + d + e) + |c|^2 c, \\
Gd &= kc + |d|^2 d + i\gamma d, \\
Ge &= kc + |e|^2 e - i\gamma e.
\end{aligned}
\tag{4.26}
$$

Similarly as before, we use the Madelung decomposition $a = Ae^{i\phi_a}, b = Be^{i\phi_b}, c = Ce^{i\phi_c}, d = De^{i\phi_d}, e = Ed^{i\phi_e}$, cf. Eq. (4.4), and focus on the simplest symmetric solutions with $A = B = D = E$. Without the loss of generality, we set $\phi_c = 0$, reducing the equations to

$$C^2(G - C^2) = 4A^2(G - A^2),$$

$$(kC)^2 = (\gamma A)^2 + (GA - A^3)^2,$$

$$\sin \phi_a = \frac{\gamma A}{kC},$$

$$\phi_a = -\phi_b = \phi_d = -\phi_e. \tag{4.27}$$

We report here numerical results for parameters $G = 15$, $k = 1$ (smaller $G$ yields similar results but with fewer solution branches). We have identified five different solutions in this case, see Figs. 4.10 and 4.11 for the representation of the continuation of the different branches, and for typical examples of their stability (the latter is shown for $\gamma = 0.1, 0.5$ and $0.95$). There are two branches (green stars and black squares) that only exist at $\gamma < 0.13$, colliding and terminating at that point. One of them has three real eigenvalue pairs and one imaginary pair, while the other branch has two real and two imaginary pairs. Two real pairs and one imaginary pair of green stars collide with two real pairs and one imaginary pair of black squares, respectively, while the final pairs of the two branches (one imaginary for the green stars and one real for the black squares) collide at the origin of the spectral plane. These collisions take place at $\gamma = 0.13$, accounting for the saddle-center bifurcation at the point where those two branches terminate. On the other hand, there exist two more branches (red crosses and magenta diamonds in Fig. 4.10), which collide at $|\gamma| = |k|$. One of these branches (the less unstable one, represented by magenta diamonds) bears only an instability induced by an eigenvalue quartet, while the highly unstable branch depicted by the red crosses has four real pairs (two of which collide on the real axis and become complex at $\gamma > 0.92$). Last but not least, the blue circles branch does not terminate at $\gamma = \pm k$, but continues to larger values of the gain-loss parameter, $|\gamma| > |k|$. It is also unstable (as the one represented by the magenta diamonds) due to a complex quartet of eigenvalues.

The dynamics of the solutions belonging to these branches is shown in Fig. 4.12. For the branches depicted by black squares and green stars (recall that they disappear through the collision and the first saddle-center bifurcation at $\gamma = 0.13$), the perturbed evolution is fairly simple: the amplitudes grow at the gain-carrying sites and decay at the lossy ones, while the central passive site (C) stays almost at zero amplitude. For the other branches, the amplitudes also grow at the two gain-carrying sites and decay at the lossy elements, while the passive site may be drawn to either the growth or decay.
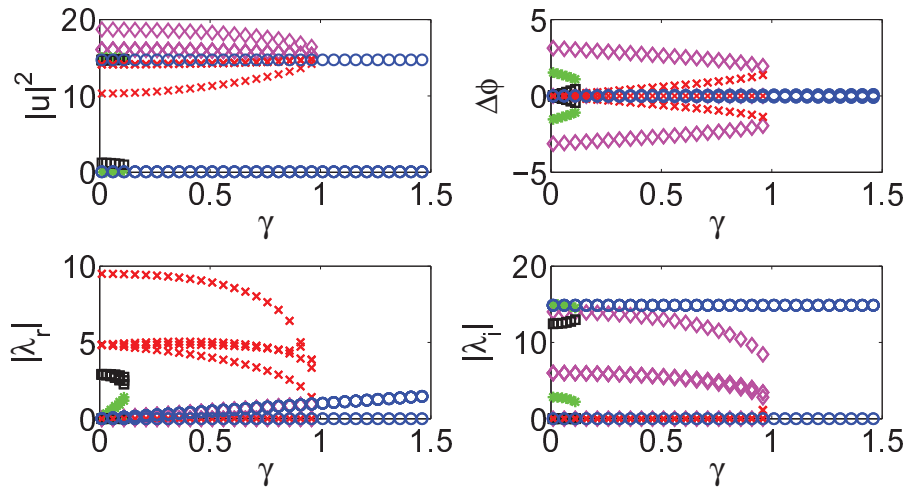


**Figure 4.10.** (Color online) The characteristics of the different branches of solutions in the case of the five-site plaquette (d) in Fig. 4.1 are shown for $G = 15$ and $k = 1$. The branches represented by the chains of black squares and green stars terminate at $\gamma = 0.13$. The branches depicted by red crosses and magenta diamonds terminate at $\gamma = 1$ [i.e., at the exceptional point $|\gamma| = |k|$], while the branch formed by blue circles continues past that point.
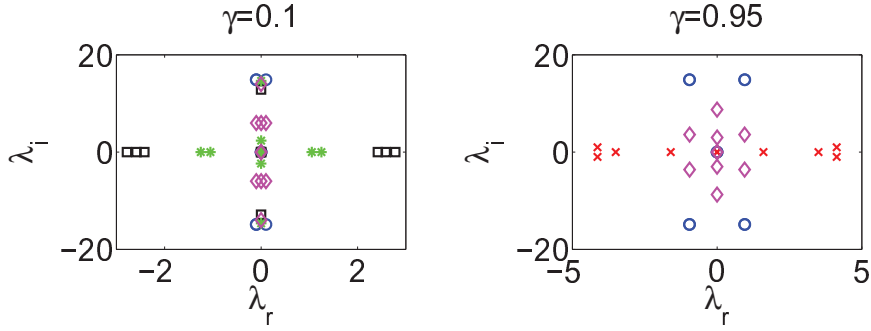
**Figure 4.11.** (Color online) Case examples of the spectral planes of the linear-stability eigenvalues for the different solution branches shown in the previous figure, for $G = 15$, $k = 1$, and $\gamma = 0.1$ and $0.95$ (from left to right).



(a) blue circles branch

(b) red crosses branch

(c) black squares branch

(d) green stars branch

(e) magenta diamonds branch
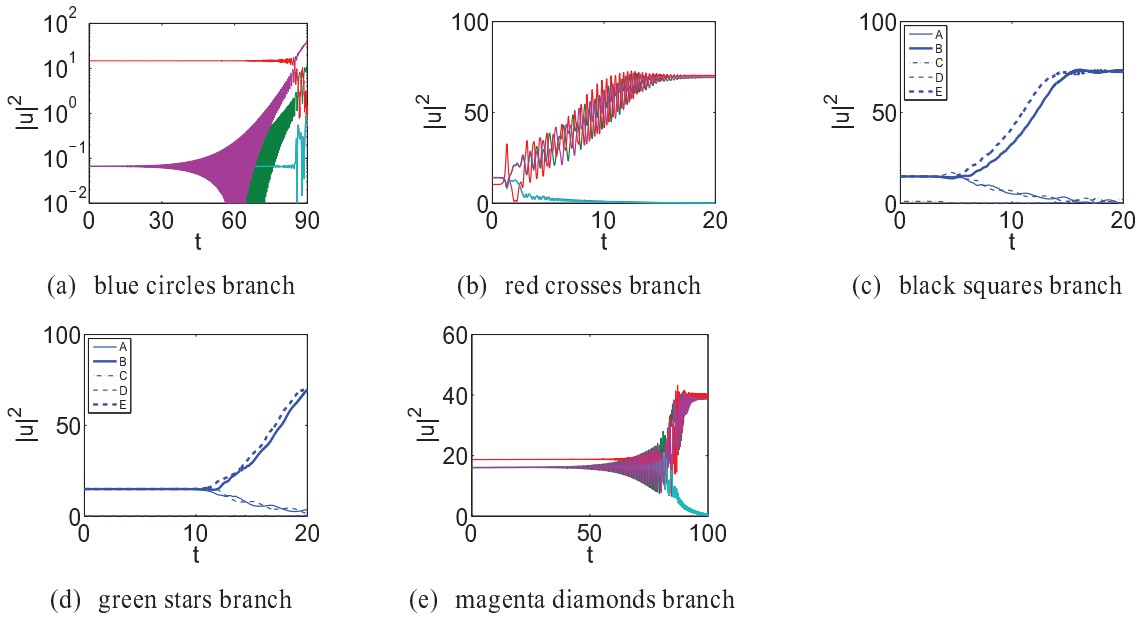
**Figure 4.12.** (Color online) The perturbed evolution for solutions belonging to different branches from Figs. 4.10 and Fig. 4.11, at $\gamma = 0.1$. In panel (a), the amplitudes at the different sites of plaquette (d) from Fig. 4.1 (A,B,C,D,E) are depicted as follows. A: the line around $10^{-1}$; B: the right one of the two triangle-like (oscillating) curves; C: the line around $10^1$; D: overlapped by A; E: the left one of the two triangle like curves. In panel (b), the amplitudes at sites A and D overlap with each other and correspond to the bottom curve which tends to 0, while the amplitudes at sites B, C, E eventually grow to a large value. Panels (c) and (d) represent the dynamical effect of the gain at sites B and E, and loss at sites A and D, while the curve for the amplitude at site C remains very close to zero. (e) A and D overlap with each other and correspond to the bottom curve, which tends to 0; B, C, E eventually grow to values $\simeq 40$. B and D overlap with each other and C starts a little higher than those two.

77

# CHAPTER 5

# $\mathcal{PT}$-SYMMETRIC COUPLER WITH BIREFRINGENT ARMS

The previously proposed settings were chiefly focused on effectively scalar models. However the "vector" type of problems is natural for experimental settings where the exploited fibers obey birefringence, since the two orthogonal polarizations are to be taken into account [41]. As a direct extension of the previous sections, in this chapter we consider a $\mathcal{PT}$-symmetric coupler whose arms are birefringent waveguides. Assuming that the first waveguide is active and the second one is absorbing, we address the problem of a $\mathcal{PT}$-preserving (in the linear limit) configuration. While being an interesting model from a physical point of view, this setting also offers a different (in comparison to what was studied before) mathematical situation where the nonlinear modes bifurcate from doubly degenerate eigenvalues of the linear problem. This requires the generalization of earlier developed approaches (e.g. like the one reported in [31]) for the bifurcation of the nonlinear modes from the linear spectrum. In addition, it presents a rich playground for dynamical systems analysis, due to the emergence of a variety of saddle-center bifurcations (nonlinear analogs of the linear $\mathcal{PT}$-phase transition), as well as symmetry-breaking (pitchfork) ones. It is these nonlinear states, their emergence, stability, dynamics and the asymptotics of the system that we will focus on hereafter.

We specify the problem by imposing that the principal optical axes of the two Kerr-type waveguides are $\pi/4$-rotated with respect to each other, as it is schematically represented in Fig. 5.1. In each arm, labeled by $j$, there are two orthogonal field components of the electric fields which we write down in the form [41] ($j = 1, 2$):

$$\mathbf{E}_j(\mathbf{r}, z, t) = \left[ u_j(z) A_j(\mathbf{r} - \mathbf{r}_j) e^{-i\beta_j z} \mathbf{e}_j + u_{j+2}(z) A_{j+2}(\mathbf{r} - \mathbf{r}_j) e^{-i\beta_{j+2} z} \mathbf{e}_{j+2} \right] \sqrt{\frac{2}{\chi}} e^{i\omega t} + c.c \quad (5.1)$$

Here $u_j$ are the field envelopes depending on the propagation distance $z$, i.e. we consider the stationary – in time – problem, assuming that the carrier wavelength $\lambda_0$ is in the region of the normal group velocity dispersion, thus ruling out a possibility of modulational instability; $\mathbf{r} = (x, y)$ is a transverse radius vector, and $\mathbf{r}_{1,2}$ are the positions of the centers of the cores of the coupler. The real parameters $\beta_j$ are the propagation constants of each of the field components, and $\mathbf{e}_j$ are the polarization vectors, which are mutually orthogonal in each arm of the coupler, i.e. $\mathbf{e}_1 \cdot \mathbf{e}_3 = \mathbf{e}_2 \cdot \mathbf{e}_4 = 0$. The real functions $A_j(\mathbf{r} - \mathbf{r}_j)$ and $A_{j+2}(\mathbf{r} - \mathbf{r}_j)$ describe the transverse distributions of the fields in each waveguide and the normalization coefficient $\sqrt{2/\chi}$, where $\chi$ is the Kerr coefficient, is introduced for convenience. For $j = 1$ and $j = 2$ the functions $A_j(\mathbf{r})$ are centered in different points $\mathbf{r}_j$. Also, for the sake of simplicity, we consider $A_j(\mathbf{r}) = A_{j+2}(\mathbf{r}) = A(\mathbf{r})$ (for $j = 1, 2$), such that the integral

$$(\mathbf{e}_j \cdot \mathbf{e}_{j+1}) \frac{\int A(\mathbf{r} - \mathbf{r}_j) A(\mathbf{r} - \mathbf{r}_{j+1}) d^2\mathbf{r}}{\int A^2(\mathbf{r}) d^2\mathbf{r}}$$

(the integration is performed over the transverse plane) describes the linear coupling between the respective modes. Since in the configuration shown in Fig. 5.1 $\mathbf{e}_1 \cdot \mathbf{e}_2 = \mathbf{e}_1 \cdot \mathbf{e}_4 = \mathbf{e}_3 \cdot \mathbf{e}_4 = -\mathbf{e}_3 \cdot \mathbf{e}_2 = 1/\sqrt{2}$ we use the single linear coupling coefficient $k$ (see also [42]). Then following the analysis described in detail in [41] we end up with the system of equa-
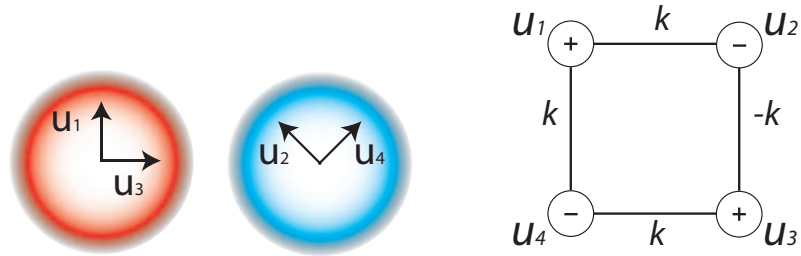


**Figure 5.1.** (Color online) (a) Schematic presentation of a $\mathcal{PT}$-symmetric coupler based on birefringent fibers. (b) Equivalent graph (plaquette) representation illustrating the $\mathcal{PT}$-symmetry. Here $-$ and $+$ stand for active and lossy waveguides, respectively.

tions:

$$i\frac{du_1}{dz} = -k(u_2 + u_4) + i\gamma u_1 - \left(|u_1|^2 + \frac{2}{3}|u_3|^2\right)u_1 - \frac{1}{3}u_3^2 u_1^* e^{i\Delta_1 z} \tag{5.2a}$$

$$i\frac{du_2}{dz} = -k(u_1 - u_3) - i\gamma u_2 - \left(|u_2|^2 + \frac{2}{3}|u_4|^2\right)u_2 - \frac{1}{3}u_4^2 u_2^* e^{i\Delta_2 z} \tag{5.2b}$$

$$i\frac{du_3}{dz} = -k(u_4 - u_2) + i\gamma u_3 - \left(\frac{2}{3}|u_1|^2 + |u_3|^2\right)u_3 - \frac{1}{3}u_1^2 u_3^* e^{-i\Delta_1 z} \tag{5.2c}$$

$$i\frac{du_4}{dz} = -k(u_1 + u_3) - i\gamma u_4 - \left(\frac{2}{3}|u_2|^2 + |u_4|^2\right)u_4 - \frac{1}{3}u_2^2 u_4^* e^{-i\Delta_2 z} \tag{5.2d}$$

Here $\gamma > 0$ describes gain in the first waveguide and dissipation in the second waveguide, $\Delta_j = \frac{4\pi c}{\lambda_0}\left(\beta_j' - \beta_{j+2}'\right)$ with $\beta_j' = \frac{d\beta_j(\omega_0)}{d\omega_0}$, $\omega_0$ being the carrier wave frequency, is a properly normalized mismatch between the propagation constants of the orthogonal polarizations $u_{j+2}$ and $u_j$. The asterisk stands for complex conjugation.

We will be interested in the stationary solutions, in particular in their linear stability properties and ensuing nonlinear dynamics which can be found in the two prototypical limiting cases of (i) zero mismatches $|\beta_j - \beta_{j+2}| = 0$ and (ii) large mismatches $|\beta_j' - \beta_{j+2}'| \gg k\lambda_0/c$ when the respective nonlinear terms can be neglected. Using the standing wave ansatz $u_j(z) = w_j e^{ibz}$, where $w_j$ are $z-$independent, into (5.2), we obtain the system of algebraic equations:

$$bw_1 = k(w_2 + w_4) - i\gamma w_1 + \left(|w_1|^2 + \frac{2}{3}|w_3|^2\right)w_1 + \frac{\alpha}{3}w_3^2 w_1^*, \tag{5.3a}$$

$$bw_2 = k(w_1 - w_3) + i\gamma w_2 + \left(|w_2|^2 + \frac{2}{3}|w_4|^2\right)w_2 + \frac{\alpha}{3}w_4^2 w_2^*, \tag{5.3b}$$

$$bw_3 = k(w_4 - w_2) - i\gamma w_3 + \left(\frac{2}{3}|w_1|^2 + |w_3|^2\right)w_3 + \frac{\alpha}{3}w_1^2 w_3^*, \tag{5.3c}$$

$$bw_4 = k(w_1 + w_3) + i\gamma w_4 + \left(\frac{2}{3}|w_2|^2 + |w_4|^2\right)w_4 + \frac{\alpha}{3}w_2^2 w_4^*. \tag{5.3d}$$

Below the spectral parameter $b$ will be also referred to as the propagation constant.

# I   Properties of the linear problem

First we address the underlying linear problem [which corresponds to the situation when all cubic terms in (5.3) are negligible]. It can be rewritten in the matrix form $\tilde{b}\tilde{\mathbf{w}} = \mathcal{H}\tilde{\mathbf{w}}$ where

$$\tilde{\mathbf{w}} = \begin{pmatrix} \tilde{w}_1 \\ \tilde{w}_2 \\ \tilde{w}_3 \\ \tilde{w}_4 \end{pmatrix} \quad \text{and } \mathcal{H} = \begin{pmatrix} -i\gamma & k & 0 & k \\ k & i\gamma & -k & 0 \\ 0 & -k & -i\gamma & k \\ k & 0 & k & i\gamma \end{pmatrix}$$

(hereafter we use tilde in order to distinguish eigenvalues and eigenvectors of the linear problem).

The operator $\mathcal{H}$ is $\mathcal{PT}$ symmetric, which means that $\mathcal{HPT} = \mathcal{PTH}$, where $\mathcal{P}$ is a spatial reversal linear operator

$$\mathcal{P} = \begin{pmatrix} 0 & 0 & 0 & 1 \\ 0 & 0 & 1 & 0 \\ 0 & 1 & 0 & 0 \\ 1 & 0 & 0 & 0 \end{pmatrix} \tag{5.4}$$

and $\mathcal{T}$ performs element-wise complex conjugation: $\mathcal{T}\mathbf{w} = \mathbf{w}^*$. The spectrum of operator $\mathcal{H}$ consists of *two double eigenvalues*

$$\tilde{b}_\pm = \pm\sqrt{2k^2 - \gamma^2}, \tag{5.5}$$

which are real for $\gamma < \gamma_{PT}^{(1)}$ where $\gamma_{cr}^{(1)} = \sqrt{2}k$ will be referred to as a primary critical point: the spontaneous $\mathcal{PT}$ symmetry breaking occurs at $\gamma_{PT}^{(1)}$ above which the eigenvalues are all imaginary. In order to visualize the $\mathcal{PT}$ symmetry of the linear system, following [31] one can represent it with a graph shown in the right panel of Fig. 5.1, reminiscent of four linearly

coupled waveguides [31] (notice however the sign difference in the coupling constants) or plaquettes [43].

## II   Exact solutions

Let us consider nonlinear modes of arbitrary amplitudes $\alpha \neq 0$. Relying on results of the previous subsection we firstly search for nonlinear modes which have equal intensities in all four waveguides. Making the substitution $w_2 = -iw_1^*$ and imposing the condition $w_4 = w_1^*$, $w_3 = w_2^*$, which is necessary for a nonlinear mode to be an eigenstate of $\mathcal{PT}$ thus leading to the circularly polarized light in each of the coupler arms, system (5.3) yields the single (complex) algebraic equation

$$bw_1 = k(1-i)w_1^* + \frac{5-\alpha}{3}|w_1|^2 w_1 - i\gamma w_1. \tag{5.6}$$

Representing $w_1 = \rho e^{i\phi}$, we obtain a bi-quadratic equation for $\rho$ yielding two families of the modes bifurcating from the eigenvalues $\tilde{b}_\pm$, given by (5.5), of the linear spectrum:

$$\rho_\pm^2 = \frac{3(b - \tilde{b}_\pm)}{5 - \alpha}, \quad e^{2i\phi_\pm} = \frac{\tilde{b}_\pm(1-i) - \gamma(1+i)}{2k}. \tag{5.7}$$

Respectively, the nonlinear modes have the following form:

$$\mathbf{w} = \begin{pmatrix} \rho_\pm e^{i\phi_\pm} \\ -i\rho_\pm e^{-i\phi_\pm} \\ i\rho_\pm e^{i\phi_\pm} \\ \rho_\pm e^{-i\phi_\pm} \end{pmatrix} \tag{5.8}$$

Using Eqs. (5.7) one can easily obtain continuous families of nonlinear modes that can be identified as a function of the propagation constant $b$, for given $k$ and $\gamma$.

For $\alpha = 0$ and $\gamma < \gamma_{cr}^{(2)}$, there exist families of elliptically polarized modes having different absolute values of the polarization vectors. However, all such modes turned out

to be unstable (see Figs. 5.2–5.3 and discussion below). In the case of zero propagation constant mismatch, i.e. when $\alpha = 1$, one also can find families which have different amplitudes of the polarization vectors. The explicit expressions for the families bifurcating from $\tilde{b}_{\pm}$ read

$$w_1 = w_4^* = \rho_{\pm} e^{i\phi}, w_2 = w_3^* = (-1 \pm \sqrt{2})\rho_{\pm} e^{-i\phi},$$
$$\rho_{\pm}^2 = \frac{b - \tilde{b}_{\pm}}{4 \mp 2\sqrt{2}}, \quad \phi = \mp\frac{1}{2}\arcsin\frac{\gamma}{\sqrt{2}k}. \tag{5.9}$$

Remarkably, these modes, which also describe propagation of elliptically polarized light, are stable in a certain range of the parameters.

## III  Families of nonlinear modes

The results of our analysis of the families of nonlinear modes are summarized in Fig. 5.2. The upper panels show that for $0 < \gamma < k$ each eigenvalue of the linearized problem gives rise to two distinct (circularly and elliptically polarized) families of nonlinear modes. Let us consider the total energy flow through the coupler, which is defined by

$$U = \sum_{j=1}^{4} |w_j|^2. \tag{5.10}$$

In the case of $\alpha = 0$ the slopes of the dependencies $U(b)$ are close for the families of both types, and the elliptically polarized families are always unstable while circularly polarized families have both stable and unstable solutions. For $\alpha = 1$ one can find stable solutions both for the families with circular and for those with elliptical polarization.

For $k < \gamma < \sqrt{2}k$, the case $\alpha = 0$ does not allow for elliptically polarized families [see Fig. 5.2 C], a feature which is in accordance with the perturbation approach developed above. In this case one can only find circularly polarized modes, which are unstable. On the other hand, for $\alpha = 1$, stable and unstable modes of both types can be found [see Fig. 5.2 D].

83
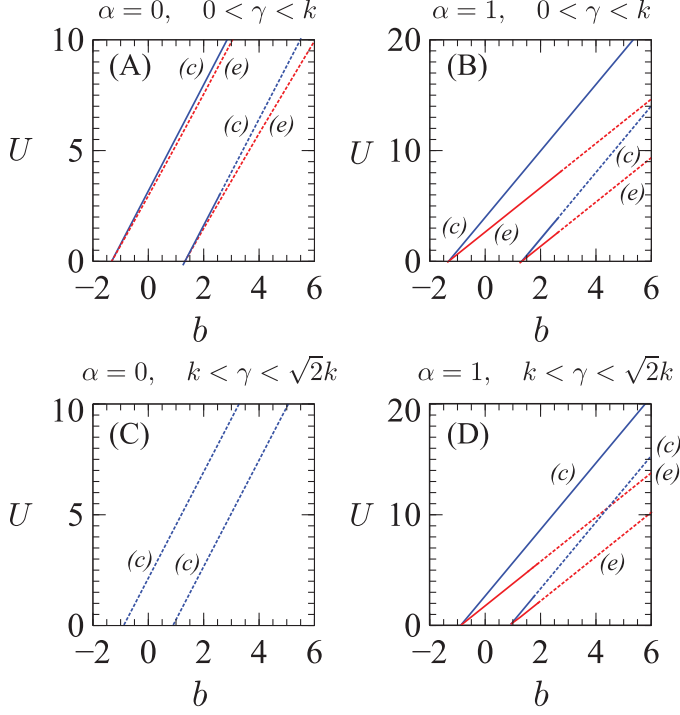
**Figure 5.2.** (Color online) Prototypical examples of families of nonlinear modes in the plane $(b, U)$ for $k = 1$ and gain-loss parameters $\gamma$: $\gamma = 0.5$ (the upper panels), $\gamma = 1.1$ (the lower panels). Left and right columns correspond to $\alpha = 0$ and $\alpha = 1$. Stable and unstable modes are shown by solid and dashed lines, respectively. The families with the circular and elliptical polarization (if any) are marked with labels "*(c)*" and "*(e)*", respectively (in the color online version families with the circular and elliptical polarization are also shown by blue and red lines, respectively). Notice that the families corresponding to the modes having exact solutions (5.7) and (5.9) are represented by the straight lines.

Summarizing at this point, we have identified 4 sets of solutions, two circularly polarized with equal amplitude at the nodes, and two elliptically polarized with unequal such amplitudes. These all degenerate into the two distinct eigenvalues $\tilde{b}_\pm$, given by (5.5), of the linear problem. The circularly polarized solutions are more robust, while the elliptically polarized ones are always unstable for $\alpha = 0$ and stable only for small enough amplitudes for $\alpha = 1$. Among the circularly polarized ones, for $0 < \gamma < \sqrt{2}k$ the more fundamental state (stemming from the negative eigenvalue at the linear limit) is always the stable ground state of the system in continuations over the parameter $b$, while the excited state is only stable for small enough amplitudes.

# IV   Continuation over $\gamma$

An alternative and perhaps even more telling way to illustrate the above features stems from fixing some value of $b$, starting from the Hamiltonian limit of $\gamma = 0$ and subsequently identifying branches of the nonlinear modes by means of changing $\gamma$, as shown in Fig. 5.3. It is important to note that this alternative viewpoint affords us the ability to visualize bifurcations that cannot be discerned over variations in $b$.

The relevant results for parametric continuations over $\gamma$ are given in Figs. 5.3-5.4; typical examples of the corresponding linearization spectra for different values of $\gamma$ can be found in Fig. 5.5. Here, it can be seen that a lower amplitude and a higher amplitude symmetric (i.e., equal amplitude) branch exist, for fixed $b$, from the Hamiltonian limit of $\gamma = 0$ and all the way up to the linear $\mathcal{PT}$-phase transition point $\gamma_{PT}^{(1)} = \sqrt{2}k$. At that point, the two symmetric branches collide and disappear in a saddle-center bifurcation which can be thought of as a nonlinear analog of the linear $\mathcal{PT}$-phase transition [44]. An additional very interesting feature arises precisely at the point $\gamma_{PT}^{(2)}$, where it can be seen that both branches of equal amplitude between the sites become dynamically unstable for $\alpha = 0$. In fact, it is seen that for the larger amplitude branch (associated with the blue circles), one pair of unstable eigenvalues arises, while for the smaller amplitude (red diamond) branch, two such pairs accompany the symmetry breaking bifurcation occurring at this critical point. A closer inspection reveals that the symmetric branch (blue circles) is destabilized through a subcritical pitchfork bifurcation with its "corresponding" asymmetric state (i.e., the one degenerate with it in the linear limit). In the case of the lower amplitude (excited) state for the same $b$, the situation appears to be more complex. In particular, there exists once again a subcritical pitchfork with the corresponding asymmetric branch, yet this would justify one pair of unstable eigenvalues and we observe two. This is because at the *same* point, there also exists a supercritical pitchfork, which gives rise to the so-called ghost states, denoted by magenta plus symbols. These states are analogous to the ones to analyzed in [27, 28, 22], but remarkably are not stationary states of the original problem, yet they are pertinent to its

dynamical (instability) evolution and for this reason they will be examined in further detail separately in the dynamics section below.

In the case of $\alpha = 1$, only one pair of unstable eigenvalues emerges for the lower amplitude branch at the secondary critical point of $\gamma_{PT}^{(2)}$ (while the larger amplitude branch remains stable throughout the continuation in $\gamma$). Hence, in this case, once again a saddle-center bifurcation will mark the nonlinear $\mathcal{PT}$-phase transition, yet the number of unstable eigendirections of each symmetric branch (fundamental and excited) is decreased by one (0 and 1 real pairs instead of 1 and 2, respectively, for $\alpha = 0$). In this case, in fact, both asymmetric branches persist up to the linear $\mathcal{PT}$-phase transition (rather than terminate in a subcritical pitchfork as above), and collide and disappear with each other. Interestingly all 3 branches (the lower amplitude, excited symmetric one and the two asymmetric ones) become unstable at the secondary critical point $\gamma_{cr}^{(2)} = k$, which again points to the existence of corresponding ghost states. For the lower amplitude symmetric branch, the bifurcating ghost states are again identified by the magenta plus symbols in Fig. 5.4.

## V   Dynamics of the polarization

To examine the potentially symmetry breaking (and more generally instability driven) nature of the dynamical evolution past the critical points identified above, we have also performed direct numerical simulations which are illustrated in Fig. 5.6; see also Fig. 5.7. Here, it can be seen that although the relevant parameters are below the critical point for the linear $\mathcal{PT}$-phase transition $\gamma_{PT}^{(1)} = \sqrt{2}k$, nevertheless, symmetry breaking phenomena are observed due to the dynamical instability of the relevant states (the ones denoted by dashed lines in Fig. 5.2). This dynamics may, in principle, be associated with the so-called ghost states of complex propagation constant that have recently been proposed as relevant for the dynamical evolution in [22]. To substantiate this claim, we note that it is observed in the left panel of Fig. 5.6 that the relative phase of the two gain sites that lock into an equal growing amplitude, is $\pi/2$, as is those of the decaying amplitude lossy sites. In light
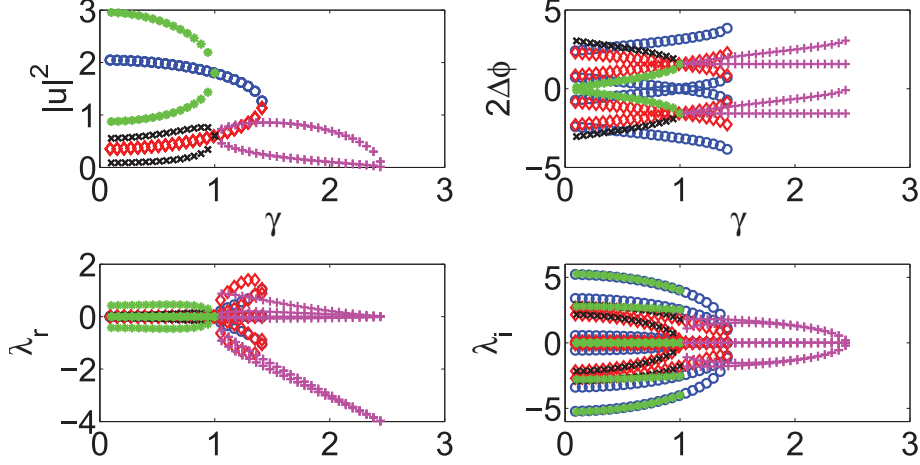
**Figure 5.3.** (Color on-line) The four panels denote the solution amplitude (top left), phase differences between adjacent nodes (top right), real and imaginary parts (second row) of eigenvalues for $\alpha = 0$, $b = 2$, and $k = 1$. The blue circles branch corresponds to the "+" sign in Eq. (5.7), while the red diamonds branch corresponds to the "-" sign (the symmetric/circularly polarized branches). The green stars and black crosses are those solutions with distinct absolute values of the polarization vectors (the asymmetric or elliptically polarized branches). In the top left panels, they collide and disappear in two subcritical pitchfork bifurcations with the blue circles and red diamond branches, respectively. The magenta pluses branch in the panels represents the ghost state solutions, which bifurcate from the red diamonds at $\gamma = \gamma_{cr}^{(2)} = 1$ and terminate at $\gamma = 2.44$.
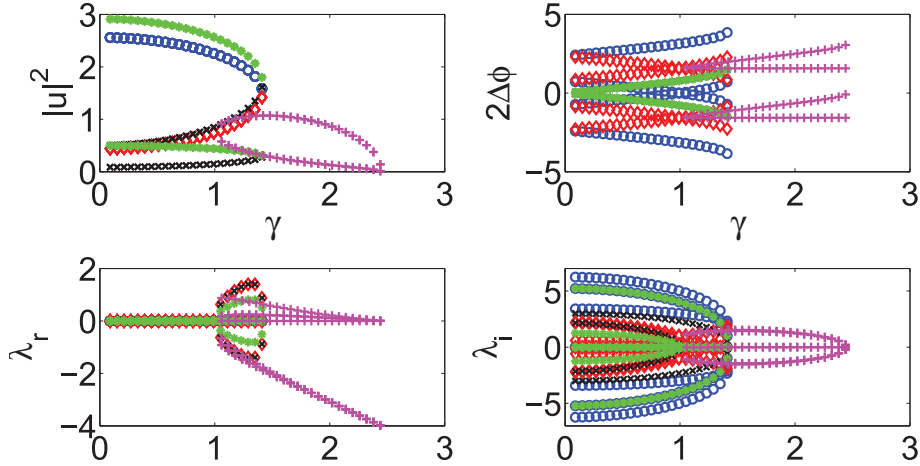


**Figure 5.4.** The four panels show the same diagnostics as in the previous figure but now for $\alpha = 1$, $b = 2$, and $k = 1$.

of this, we seek ghost states with precisely this phase difference and are able to explicitly identify them via the ansatz $w_3 = iw_1$, $w_4 = iw_2$, setting $w_j = c_j e^{i\phi_j}$ for $j = 1, 2$. For
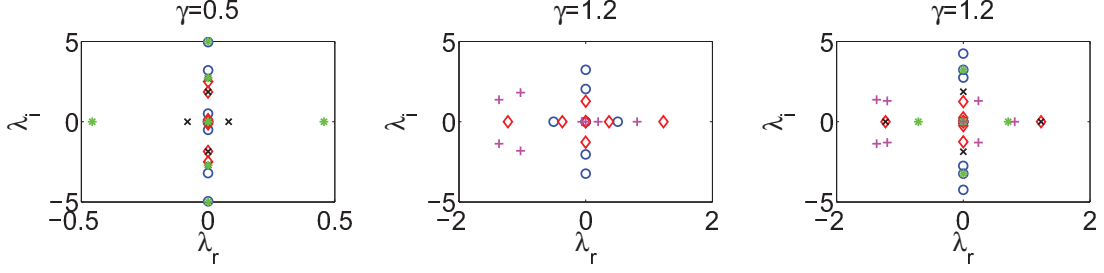
**Figure 5.5.** Stability plots. The top two panels are for $\alpha = 0$, and the bottom one is when $\alpha = 1$. In the case $\alpha = 0$, at $\gamma = \gamma_{cr}^{(2)} = 1$, one pair of blue circles and two pairs of red diamonds collide at 0 so that one pair of real eigenvalues arises in blue circles branch whereas two pairs of real eigenvalues arise in the red diamonds branch. The asymmetric branches only exist (and are unstable) for the smaller value of $\gamma = 0.5$, for $\alpha = 0$. For the same parameters ($b = 2$, $k = 1$), in the case of $\alpha = 1$, the excited symmetric and both asymmetric branches are unstable for $\gamma = 1.2$.

these branches, the propagation constant is complex. This highlights the potential growth or decay of such states. Importantly also, note that these states are "ghosts" because they may be solving the stationary problem of Eqs. (5.3), but the U(1) invariance of the original model does *not* permit them to be a solution of the dynamical Eqs. (5.2).

The algebraic conditions that this family of solutions satisfies are

$$\sin \phi_b = \frac{(c_2^2 - c_1^2)\gamma}{(c_1^2 + c_2^2)B} \tag{5.11}$$

$$\cos \phi_b = \frac{(5 - \alpha)(c_1^2 + c_2^2)}{3B} \tag{5.12}$$

$$\sin(\phi_2 - \phi_1)$$
$$= \frac{(3\gamma - B(\sin \phi_b + \cos \phi_b) + (5 - \alpha)c_2^2)c_2}{6kc_1} \tag{5.13}$$
$$= \frac{(3\gamma + B(\sin \phi_b - \cos \phi_b) + (5 - \alpha)c_1^2)c_1}{6kc_2} \tag{5.14}$$

$$\cos(\phi_2 - \phi_1)$$
$$= \frac{(3\gamma - B(\sin \phi_b - \cos \phi_b) - (5 - \alpha)c_2^2)c_2}{6kc_1} \tag{5.15}$$
$$= \frac{(3\gamma + B(\sin \phi_b + \cos \phi_b) - (5 - \alpha)c_1^2)c_1}{6kc_2}. \tag{5.16}$$

88

Notice that the imaginary part of the propagation constant $B\sin(\phi_b)$ is proportional to the difference $c_1^2 - c_2^2$. Hence, prior to the symmetry breaking, the relevant solutions bear a real propagation constant. Past the bifurcation point one (unstable) branch has $c_2^2 > c_1^2$, while the stable branch has $c_1^2 > c_2^2$. The relevant ghost state branches and their bifurcation from the equal amplitude ones are explored in Fig. 5.3-5.4. Given that these are only ghost solutions of the original dynamical problem, the interpretation of their linearization spectrum (shown for completeness in Fig. 5.5) is still an open problem.

These ghost states appear, in fact, to be the ones directly observed in the unstable evolution dynamics. To illustrate this, we observed the particular behavior of the unstable modes and how it depends on the form of the initial perturbation. A typical example in which the gain sites lead to growth and the lossy sites to decay is shown in the left panel of Fig. 5.6. On the other hand, in the right panel of Fig. 5.6 a different scenario of evolution is illustrated. Instead of the gain nodes growing and the lossy ones decaying, a breathing oscillation settles between the two pairs. These two scenarios, illustrated in Fig. 5.6, are the prototypical instability evolution ones that we have obtained in this system. Fig. 5.7 shows the evolutionary plot of the ghost states, together with its predicted rate of growth given by $-2b\sin\phi_b$ in red dashed lines.
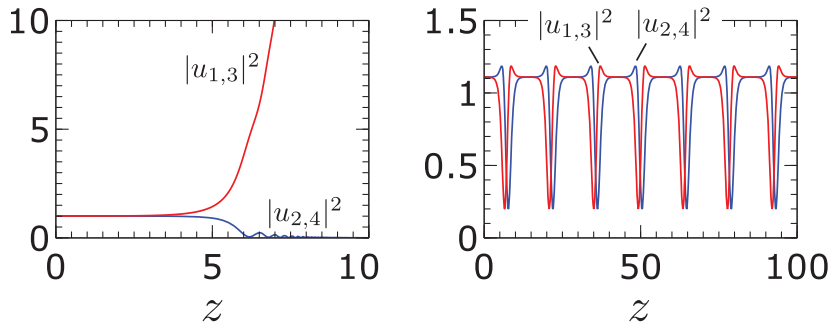
**Figure 5.6.** (Color online) Dynamics of an unstable circularly polarized mode at $b = 3$, $\gamma = 0.5$ and for $\alpha = 0$ for two different small initial perturbations. The result of the evolution of the left panel involves growth at the gain sites ($u_{1,3}$, red curves in the color online version) and decay at the lossy sites ($u_{2,4}$, blue curves in the color online version). Notice that intensities among the two gain sites and among the two lossy sites are approximately equal ($|u_1|^2 \approx |u_3|^2$ and $|u_2|^2 \approx |u_4|^2$) and are not distinguishable in the scale of the plots. In the right panel only the initial stage of the found persistent periodic dynamics is shown; the simulations were performed up to $z = 2000$.
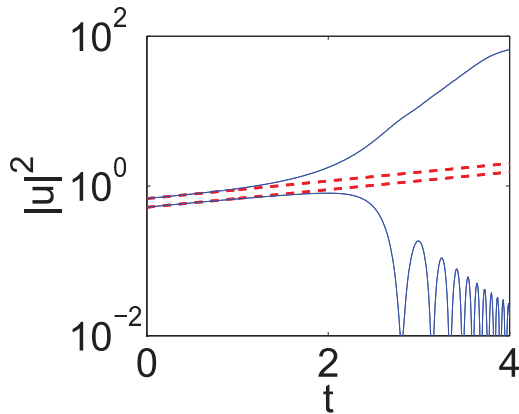


**Figure 5.7.** The dynamical semi-log plot of the ghost state (magenta pluses branch in Fig. 5.3) with $\alpha = 0$, $b = 2$, and $k = 1$ for $\gamma = 1.02$. The dashed lines are the predicted dynamics of the ghost states on the basis of their growth rates.

90

# CHAPTER 6

# CONCLUSIONS AND FUTURE CHALLENGES

In this thesis, we considered the existence, stability, and dynamics of $\mathcal{PT}$-symmetric one-dimensional linear and nonlinear oligomers as well as two dimensional plaquettes.

Chapter 2 started our considerations by a complete characterization of the dimer case, where the two obtained branches of solutions terminate at the critical point of the linear case. However, we illustrated that the trimer and quadrimer feature a number of fundamental differences in comparison with this dimer behavior. In particular, the trimer features branches which exist past the linear critical point (although unstable). On the other hand, the quadrimer has even richer features: in particular, it possesses completely asymmetric solutions. The bifurcation structure is also richer in the latter problem, featuring symmetry-breaking pitchfork bifurcations. Another notable feature is that some solutions do not exist for arbitrary combinations of coupling, gain-loss parameter, and propagation constant; instead, these parameters appear to be inter connected (at least in the case of a single gain-loss parameter considered herein). Finally, even the linear problem presents interesting variations in this case, featuring the breaking of the real nature of the eigenvalues through two colliding pairs that lead to a quartet occurring for smaller gain-loss parameter values than in the trimer case.

Chapter 3 generalized one-dimensional oligomers in Chapter 2 and examined different types of solutions of such configurations with linear and nonlinear gain or loss profiles. Solutions beyond the linear $\mathcal{PT}$-symmetry critical point as well as solutions with asymmetric linearization eigenvalues are found in both the nonlinear dimer and trimer. The latter feature is absent in linear PT-symmetric trimers, while both of them are absent in linear

PT-symmetric dimers. Furthermore, nonlinear gain/loss terms enable the existence of both symmetric and asymmetric solution profiles (and of bifurcations between them), while only symmetric solutions are present in the linear $\mathcal{PT}$-symmetric dimers and trimers.

Chapter 4 considered two-dimensional plaquettes, which may be subsequently used as fundamental building blocks for the construction of $\mathcal{PT}$-symmetric two-dimensional lattices. In this context, we have introduced four basic types of plaquettes, three of which in the form of four-site squares. The final one was in the form of the five-site cross, motivated by earlier works on cross-shaped (alias rhombic or site-centered) vortex solitons in the discrete nonlinear Schrödinger equation. Our analysis was restricted to modes which could be found in the analytical form, while their stability against small perturbations was analyzed by means of numerical methods. Even within the framework of this restriction, many effects have been found, starting from the existence of solution branches that terminate at the critical points of the respective linear $\mathcal{PT}$-symmetric systems — e.g., in the settings corresponding to plaquettes (a) and (c) in Fig. 4.1. The bifurcation responsible for the termination of the pair of branches may take a complex degenerate form [such as the one in the case of setting (a)]. Other branches were found too, that continue to exist, due to the nonlinearity, past the critical points of the underlying linear systems. In addition, we have identified cases [like the gain-loss alternating pattern (b) or the cross plaquette of type (d)] when the $\mathcal{PT}$ symmetry is broken immediately after the introduction of the gain-loss pattern. The spectral stability of the different configurations was examined. Most frequently, the stationary modes are unstable, although stable branches were found too [e.g., in settings (a) and (c)]. We have also studied the perturbed dynamics of the modes. The evolution of unstable ones typically leads to the growth of the amplitudes at the gain-carrying sites and decay at the lossy ones. It was interesting to observe that the passive sites, without gain or loss, might be tipped towards growth or decay, depending on the particular solution (and possibly on specific initial conditions).

In Chapter 5 , we have proposed a novel, physically realistic variant of a $\mathcal{PT}$ symmetric dimer where the effect of birefringence has been taken into consideration. The existence of polarization of the electric field within the coupler yields two complex dynamical equations for each of the fibers, providing a physical realization of a plaquette model with *both linear and nonlinear* coupling between the elements. The stationary states of the model were identified and both linear and nonlinear $\mathcal{PT}$-phase transitions were obtained. The degenerate nature of the linear limit complicated the problem in comparison to other ones studied earlier in this context. Furthermore, the emergence of symmetry breaking phenomena and associated (subcritical or supercritical) pitchfork bifurcations, as well as their dynamical implications in leading to indefinite growth and decay (of the corresponding waveguide amplitudes) were elucidated. A connection was given to ghost states that appeared to dominate the symmetry-breaking dynamics.

The next relevant step of the analysis may be to search for more sophisticated stationary modes (that plausibly cannot be found in an analytical form), produced by the *symmetry breaking* of the simplest modes considered in this work, cf. Ref. [23]. The difference of such modes from the $\mathcal{PT}$-symmetric ones considered in the present work is the fact that modes with the unbroken symmetry form a continuous family of solutions, with energy $E$ depending on the solution's amplitude, see Eq. (4.1). This feature, which is generic to conservative nonlinear systems, is shared by $\mathcal{PT}$-symmetric ones, due to the "automatic" balance between the separated gain and loss. On the other hand, the breaking of the symmetry gives rise to the typical behavior of systems with competing, but not explicitly balanced, gain and loss, which generate a single or several *attractors*, i.e., *isolated* solutions with a single or several values of the energy, rather than a continuous family. A paradigmatic example of the difference between continuous families of solutions in conservative models and isolated attractors in their (weakly) dissipative counterparts is the transition from the continuous family of solitons in the usual Nonlinear Schrödinger Equation (NLSE) to a pair of isolated soliton solutions, one of which is an attractor (and the other is an unsta-

93

ble solution playing the role of the separatrix between attraction basins, the stable soliton and the stable zero solution) in the complex Ginzburg-Landau equation, produced by the addition of the cubic-quintic combination of small dissipation and gain terms to the NLSE [45].

Moreover, the present work may pave the way to further considerations of two-dimensional $\mathcal{PT}$-symmetric lattice systems, and even three-dimensional ones. In this context, the natural generalization is to construct periodic two-dimensional lattices of the building blocks presented here, and to identify counterparts of the modes reported here in the infinite lattices, along with new modes which may exist in that case. On the other hand, in the three-dimensional realm, the first step that needs to be completed would consist of the examination of a $\mathcal{PT}$-symmetric cube composed of eight sites, and the nonlinear modes that it can support. This, in turn, may be a preamble towards constructing full three-dimensional $\mathcal{PT}$-symmetric lattices. These topics are under present consideration and will be reported elsewhere.

# BIBLIOGRAPHY

[1] C.M. Bender and S. Boettcher, Phys. Rev. Lett. **80**, 5243 (1998); C.M. Bender, S. Boettcher and P.N. Meisinger, J. Math. Phys. **40**, 2201 (1999); C.M. Bender, Rep. Prog. Phys. **70**, 947 (2007).

[2] Z.H. Musslimani, K.G. Makris, R. El-Ganainy and D.N. Christodoulides, Phys. Rev. Lett. **100**, 030402 (2008); K.G. Makris, R. El-Ganainy, D.N. Christodoulides and Z.H. Musslimani, Phys. Rev. A **81**, 063807 (2010).

[3] V. Achilleos, P.G. Kevrekidis, D.J. Frantzeskakis, R. Carretero-González, arXiv:1202.1310.

[4] A. Guo, G. J. Salamo, D. Duchesne, R. Morandotti, M. Volatier-Ravat, V. Aimez, G. A. Siviloglou and D. N. Christodoulides, Phys. Rev. Lett. **103**, 093902 (2009).

[5] C.E. Rüter, K.G. Makris, R. El-Ganainy, D.N. Christodoulides, M. Segev, D. Kip, Nature Phys. **6**, 192 (2010).

[6] J. Schindler, A. Li, M.C. Zheng, F.M. Ellis and T. Kottos, Phys. Rev. A **84**, 040101 (2011).

[7] H. Ramezani, T. Kottos, R. El-Ganainy and D.N. Christodoulides, Phys. Rev. A **82**, 043803 (2010).

[8] A.A. Sukhorukov, Z. Xu and Yu.S. Kivshar, Phys. Rev. A **82**, 043818 (2010).

[9] M.C. Zheng, D.N. Christodoulides, R. Fleischmann and T. Kottos, Phys. Rev. A **82**, 010103(R) (2010).

[10] E.M. Graefe, H.J. Korsch and A.E. Niederle, Phys. Rev. Lett. **101**, 150408 (2008).

[11] E.M. Graefe, H.J. Korsch and A.E. Niederle, Phys. Rev. A **82**, 013629 (2010).

[12] Z. Lin, H. Ramezani, T. Eichelkraut, T. Kottos, H. Cao and D.N. Christodoulides, Phys. Rev. Lett. **106**, 213901 (2011).

[13] K. Li and P. G. Kevrekidis Phys. Rev. E **83**, 066608 (2011)

[14] S.V. Dmitriev, S.V. Suchkov, A.A. Sukhorukov, and Yu.S. Kivshar, Phys. Rev. A **84**, 013833 (2011)

[15] S. V. Suchkov, B. A. Malomed, S. V. Dmitriev and Yu. S. Kivshar, Phys. Rev. E **84**, 046609 (2011).

[16] R. Driben and B. A. Malomed, Opt. Lett. **36**, 4323 (2011).

[17] R. Driben and B. A. Malomed, Europhys. Lett. **96**, 51001 (2011).

[18] F. Kh. Abdullaev, V.V. Konotop, M. Ögren and M. P. Sørensen, Opt. Lett. **36**, 4566 (2011).

[19] N.V. Alexeeva, I.V. Barashenkov, A.A. Sukhorukov, and Yu.S. Kivshar, Phys. Rev. A **85**, 063837 (2012).

[20] A.A. Sukhorukov, S.V. Dmitriev and Yu.S. Kivshar, Opt. Lett. **37**, 2148 (2012).

[21] E.-M. Graefe, arXiv:1206.4806.

[22] A. S. Rodrigues, K. Li, V. Achilleos, P. G. Kevrekidis, D. J. Frantzeskakis, C. M. Bender, Rom. Rep. Phys. **65**, 5 (2013).

[23] A.E. Miroshnichenko, B.A. Malomed, and Yu.S. Kivshar Phys. Rev. A **84**, 012123 (2011).

[24] F.Kh. Abdullaev, Y.V. Kartashov, V.V. Konotop and D.A. Zezyulin, Phys. Rev. A **83**, 041805 (2011)

[25] D. A. Zezyulin, Y. V. Kartashov, V. V. Konotop, Europhys. Lett. **96**, 64003 (2011).

[26] M. Hiller, T. Kottos, and A. Ossipov, Phys. Rev. A, **73**, 063625 (2006).

[27] H. Cartarius and G. Wunner, Phys. Rev. A, **86**, 013612 (2012); H. Cartarius, D. Haag, D. Dast, and G. Wunner, J. Phys. A: Math. Theor., **45**, 444008 (2012).

[28] E.-M. Graefe, J. Phys. A **45**, 444015 (2012).

[29] T. Kapitula, P. G. Kevrekidis and Z. Chen, SIAM J. Appl. Dyn. Sys. **5**, 598 (2006).

[30] V. Achilleos, P. G. Kevrekidis, D. J. Frantzeskakis, R. Carretero-González, arXiv:1208.2445.

[31] D. A. Zezyulin and V. V. Konotop, Phys. Rev. Lett. **108** 213906 (2012).

[32] F. C. Moreira, F. Kh. Abdullaev, V. V. Konotop, and A. V. Yulin, Phys. Rev. A **86**, 053815 (2012).

[33] F. C. Moreira, V. V. Konotop, and B. A. Malomed, Phys. Rev. A **87**, 013832 (2013).

[34] P. G. Kevrekidis, D. E. Pelinovsky, and D. Y. Tyugin, arXiv:1303.3298, SIAM J. Appl. Dyn. Sys. (in press, 2013); also: P. G. Kevrekidis, D. E. Pelinovsky, and D. Y. Tyugin, arXiv:1307.2973.

[35] M. Johansson, J. Phys. A: Math. Gen. **37**, 2201 (2004); R.H. Goodman, J. Phys. A: Math. Theor. **44**, 425101 (2011).

[36] P. G. Kevrekidis *The discrete nonlinear Schrödinger equation: Mathematical Analysis, Numerical Computations and Physical Perspectives*, Springer-Verlag (Heidelberg, 2009).

[37] B. A. Malomed and P. G. Kevrekidis Phys. Rev. E **64**, 026601 (2001).

[38] D. E. Pelinovsky, P. G. Kevrekidis, D. J. Frantzeskakis, Phys. D **212**, 1 (2005).

[39] J. W. Fleischer, G. Bartal, O. Cohen, O. Manela, M. Segev, J. Hudock, and D. N. Christodoulides Phys. Rev. Lett. **92**, 123904 (2004).

[40] D. N. Neshev, T. J. Alexander, E. A. Ostrovskaya, Yu. S. Kivshar, H. Martin, I. Makasyuk, and Z. Chen, Phys. Rev. Lett. **92**, 123903 (2004).

[41] C. R. Menyuk IEEE J. Quant. Eelectron., **23**, 174-176 (1987)

[42] A. W. Snyder and Y. Chen, Opt. Lett. **14**, 517 (1989); Y. Chen, A. W. Snyder, and D. N. Payne, IEEE J. Quant. Electro. **28**, 239 (1992); M. Romagnoli S. Trillo, S. Wabnitz, Opt. and Quant. Electron. **24**, S1237 (1992).

[43] K. Li, P.G. Kevrekidis, B. A. Malomed and U. Guenther, J. Phys. A: Math. Theor. **45** 444021 (2012).

[44] V. Achilleos, P.G. Kevrekidis, D.J. Frantzeskakis, and R. Carretero-González Phys. Rev. A **86**, 013808 (2012).

[45] B. A. Malomed, Physica D **29**, 155 (1987)